MONITORING UNREST FROM AMBIENT SEISMIC NOISE RECORDINGS: RESULTS FROM MOUNT RUAPEHU, NEW ZEALAND FOR 2022

A thesis presented in partial fulfillment of the
requirements for the degree of

Master of Science
in
Earth Science

by

MUSTAFA ALMASSRI

Massey University, Palmerston North, New Zealand.

April 2024

Almassri, **Mustafa** (**Master of Science**, **Earth Science**)

MONITORING UNREST FROM AMBIENT SEISMIC NOISE RECORDINGS: RESULTS FROM MOUNT RUAPEHU, NEW ZEALAND FOR 2022

Thesis supervised by **Stuart Mead**
Co-supervised by **Oliver lamb**
Georg Zellmer

ABSTRACT

Ruapehu is an active andesitic composite volcano that had two significant eruptions on 4 October 2006 and on 25 September 2007 since the last major eruption in 1995–1996. These were mostly phreatic explosions that happened with minimal precursors. A significant unrest period occurred between March and June at Ruapehu volcano in 2022, with heating of the crater lake and tremor levels consistent with moderate to high levels of volcanic unrest.

In this study, velocity changes during the 2022 unrest were explored using seismic interferometry. Analysis of one year of ambient noise data using moving window cross-spectral analysis (MWCS) found a nearly 0.5% drop in the East-North edifice's seismic velocity, while no reduction in velocity was noted in the West-North. This decrease began three weeks before the unrest signals of Crater Lake temperature and tremor were observed. This drop is a reversible process, and several factors, including fractures opening, fluid fluxes like water, gas, or magma, magmatic anomalies, magma intruding into the subsurface without reaching the surface, and environmental factors (such as rainfalls or changes in atmospheric pressure), could cause a low-velocity zone. There is, however, no evidence of the precise reason for the 2022 unrest.

ACKNOWLEDGEMENTS

Firstly, I would like to express my gratitude to Georg Zellmer for his unwavering support from the moment I set out on this scholarship journey until I arrived in New Zealand. Georg has always provided insightful advice and guidance at every step of the way. Thank you for the opportunity to be part of this research project. I would like also to express my heartfelt gratitude to Stuart Mead. Over the past few months, your guidance has been invaluable, both with the thesis and any general questions I have had. His expertise and thoughtful comments have been essential to the accomplishment of this thesis. I appreciate his patience, constructive criticism, and support. I would also like to thank Oliver Lamb for the discussions we had during this thesis, as well as for your invaluable feedback, and helpful suggestions. Thank you to Alexander Yates for helping me with the SNR computation and for our discussion regarding his work with the MSNoise.

Thank you to the Ministry of Business, Innovation and Employment (MBIE) for supporting me financially through the Smart Idea Scholarship. With this support, I was able to finish my thesis without experiencing undue financial strain.

To my parents, you have given me more support than I could have ever imagined during my academic career. Especially to my mother for always being there for me as a friend. Thank you for always pushing me to be my best. You are the reason I have so many opportunities in life!

Finally, as I reflect on reaching this milestone, I feel obligated to dedicate it to two integral aspects of my thesis journey that have a profound impact on me.

First and foremost, I wish to honour the memory of my beloved little brother, "*Akram*", whose passing has had a significant impact on my life while writing this thesis. Even though he is no longer physically with us, his spirit and innocent smile still motivate me every day. I trust that he now resides in a place of peace and serenity and am thankful for the time we had together.

Second, I would like to express my sincere gratitude to *Gaza*, my hometown, which has simultaneously been a source of resiliency, love, and hope as well as a birthplace of pain. It is a city that personifies the dichotomy of peace and war, where ties of solidarity endures and love persists despite the chaos.

TABLE OF CONTENTS

CHAPTER

APPENDIX

LIST OF TABLES

TABLE

LIST OF FIGURES

FIGURE

CHAPTER 1

INTRODUCTION

New Zealand is made up of three different tectonic processes, including two opposing subducting systems that are divided by a strike-slip fault [Figure 1.1]. These faults produce strong earthquake activity as a result. As the Pacific plate subducted beneath New Zealand's North Island toward the west, intense volcanism resulted forming the Taupō Volcanic Zone (TVZ) [Rowlands et al., 2005]. Two of the TVZ's most visually striking volcanic features are the Tongariro and Ruapehu volcanoes, which are both situated in the southern part of the TVZ [Leonard et al., 2021]. Ruapehu volcano is a significant area of research due to the variety of eruption sizes, hazardous processes produced, and the potential effects they may have on nearby tourists and the North Island of New Zealand [Leonard et al., 2021].

The iconic stratovolcanoes Ruapehu (150 km^3 cone, 150 km^3 ring-plain) and Tongariro (90 km^3 cone, 60 km^3 ring-plain) formed at $\sim$ 230 and $\sim$ 350 ka, respectively, in the southern Taupō Volcanic Zone and Taupō Rift [Leonard et al., 2021]. Most historical eruptions of Mt. Ruapehu have come through Crater Lake, and a very common artifact of eruptions of Ruapehu is the production of lahars [Manville and Cronin, 2007, Mordret et al., 2010]. Additionally, these eruptions produce ballistics that may injure climbers near the Crater Lake. Mt. Ruapehu is also home to two sizable ski areas, which increases the risk from eruptions during winter periods. Ruapehu is vulnerable to damaging lahars because of the 10^7 m^3 of hot, acidic water in Crater Lake and the surrounding summit glaciers and ice fields. The thousands of skiers in the ski area are the ones most at risk that cross a northern lahar route [Leonard et al., 2021]. This risk makes it critical for us to monitor and understand the volcanic processes at Ruapehu.

For this reason, the structure, history, unrest events, and evaluation of Ruapehu have been the subject of scientific research, but there are still many unanswered questions that need to be investigated. This thesis explores volcanic unrest during the year 2022 at Ruapehu and presents the results of the cross-correlation function from the ambient noise technique to assess whether the ambient noise velocity variations technique is feasible for monitoring Ruapehu Volcano.

Seismic interferometry analysis techniques have shown that large earthquakes or volcanic activities are connected with temporary variations in seismic velocity. These interferometric techniques are now widely used to monitor temporal changes in structure [Hirose et al., 2017]. Seismic interferometry estimates seismic velocity changes using cross-correlation functions of ambient seismic noise, allowing us to track seismic velocity changes continuously [Hirose et al., 2017, Curtis et al., 2006, Brenguier et al., 2008b]. Cross-correlating seismic wavefields collected at several seismic stations can then make it possible to identify subtle changes in the subsurface that may be attributed to a number of geophysical processes.

1.1 STUDY AIMS AND OBJECTIVES

Predicting the timing and location of volcanic eruptions is a primary goal of volcanology, which seeks to get a thorough understanding of the magmatic processes and products of volcanoes worldwide [Sparks, 2003]. However, a lot of information remains unknown, making it difficult for us to forecast when and how a volcano will erupt [Wilson, 2017]. One way to think of volcanic activity is as the consequence of magma rising into contact with the Earth's surface. The identification of rising magma or the disruption of a pre-existing shallow chamber is an essential factor in predicting the timing of an eruption. Deformation of the crust is predicted to be caused by increases in subsurface pressures prior to volcanic eruptions [Sparks, 2003, Savage et al., 2015]. To better understand volcanic processes, a wide range of disciplines have focussed on monitoring precursory activity at volcanoes [Sparks, 2003].

Recently seismologists started to utilize seismic ambient noise which has created an exciting new path for the monitoring of small crustal changes. The use of ambient noise is significant because it can yield continuous seismic velocity data that can identify small variations in the crust's elastic properties. This makes it possible to collect data when there are no seismic events, such as during the pressurization or movement of magma [Brenguier et al., 2008a]. The study of seismic velocity variations has become a reliable and robust method for monitoring volcanic activity. These variations are sensitive to the subsurface changes and provide important information regarding magma flow, pressure fluctuations, and structural changes within volcanic systems. As a result, the method has gained significance for monitoring volcanoes, and the number of research studies using it is expanding quickly [Mordret et al., 2010, Ratdomopurbo and Poupinet, 1995, Minato et al., 2012, Lecocq et al., 2014, Clarke et al., 2011, Poupinet et al., 1984, Aki and Ferrazzini, 2000].

An interesting case study for ambient noise-based monitoring is Mount Ruapehu in New Zealand. Not only have there been several well-recorded eruptions in recent years, including the one that occurred in 2006, but also significant periods of heightened volcanic activity detected through increased seismicity and changes in crater lake dynamics. The significant unrest period that occurred in 2022 at Ruapehu volcano presents a unique opportunity to investigate changes in seismic velocity during volcanic unrest. This period of heightened seismic activity, rising Crater Lake temperature, and increasing gas emissions, including sulfur dioxide, without causing an eruption, provides scientists with an opportunity to further investigation the causes of the increased seismic activity and the dynamic processes occurring beneath the surface of the volcano. Seismic velocity fluctuations during this unrest may provide knowledge of how seismic velocities vary over time, and can yield important insights into fluid dynamics and magma transport within the volcanic system. Furthermore, studying variations in seismic velocity during volcanic activity can help build better early warning and monitoring systems for volcanic hazards, which will eventually increase our capacity to reduce risks and safeguard communities infrastructure and populations.

This thesis aims to investigate seismic velocity changes during volcanic unrest and to understand how velocity change could help us monitor volcanoes such as Ruapehu. The key objectives of this study to meet this aim are delineated below:

- Identify the seismic velocity and velocity variations at Ruapehu volcano during 2022.
- Investigate the correlation between the seismic velocity variations and the unrest.
- Identify changes in seismic velocity during the unrest in 2022.
- Consider the use of ambient noise for the detection and monitoring of volcanic unrest and activity.

1.2 THESIS STRUCTURE

To meet these aims and objectives, this thesis comprises five chapters in the following structure:

- **CHAPTER 01 - INTRODUCTION**

  The motivation for this study as well as its goals are presented in this chapter. It also briefly overviews the background, covering the region's geology, tectonic setting, and recent unrest in the TVZ and at Ruapehu.

- **CHAPTER 02 - BACKGROUND THEORY**

  In this chapter, we present background information on the theory of seismic noise including the characteristics of ambient seismic noise, cross-correlation methods and methods for extracting seismic velocity variations. Additionally, it summarises previous studies that used similar methods to monitor volcanoes.

- **CHAPTER 03 - METHODOLOGY AND DATA**

  The procedures for handling cross-correlations for station pairs are described in this chapter. Included here are the explanations of the procedures used to compute the Green Function and extract seismic velocity, and parameter testing.

- **CHAPTER 04 - RESULTS**

  After processing the cross-component station pair ambient noise up to velocity variations, this chapter presents the seismic velocity variations for 2022 at Ruapehu volcano.

- **CHAPTER 05 - DISCUSSIONS**

  This chapter discusses the velocity variations identified in reference to other signals of unrest (Crater Lake temperature and volcanic tremor) and the potential for ambient noise in monitoring of volcanic unrest.

- **CHAPTER 06 - CONCLUSION**

  A summary of this thesis' primary objectives and how we achieved them are presented in the last chapter. The chapter ends with suggestions for further research as well as the limitations of our research.

- **APPENDICES**

  There are two sections to the appendices. All of the final processing parameters that MSNoise uses to process data from ambient noise to velocity changes are listed in this Appendix [see Appendix A.1]. The station final filter utilized in this finding is included in Appendix A.2.

1.3 GEOLOGICAL AND TECTONIC SETTINGS OF NEW ZEALAND

New Zealand was thought of as part of Gondwanaland which was attached to Australia and Antarctica before the Late Cretaceous seafloor spreading. Only 5 - 10 % of the continent Zealandia lies above sea level, which forms the New Zealand region [Campbell et al., 2012, Mortimer, 2004]. The tectonics of New Zealand are primarily governed by the convergence of the Australian and Pacific Plates at rates of 39–48 mm/yr [Anderson et al., 1993, Norris et al., 1990, Wallace et al., 2012, Norris and Cooper, 1997, Hamling et al., 2015]. New Zealand comprises three types of tectonic processes with the northern and southern regions of two opposing subducting systems, separated by a strike-slip fault [Figure 1.1]. This section will provide a brief overview of the geological evolution and tectonic setting of New Zealand.

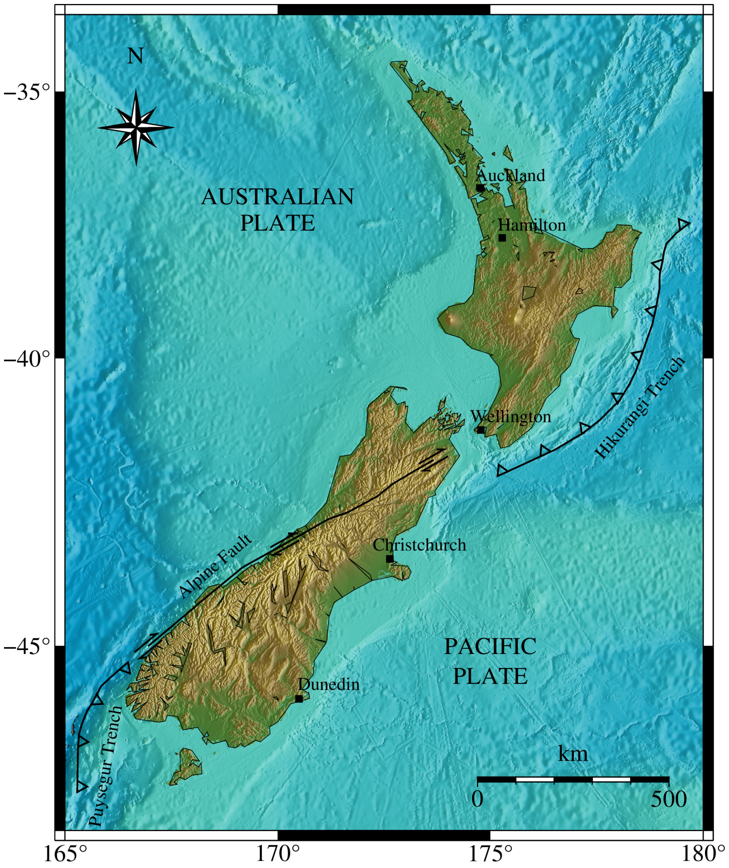

Figure 1.1: Map of New Zealand's geology. The map shows three of the main tectonic faults the Alpine Fault, the Hikurangi subduction zone, and the Puysegur Trench.

1.3.1 NORTH ISLAND OF NEW ZEALAND

The North Island of New Zealand is located in the boundary zone between the obliquely convergent (40° - 70°) Pacific and Australian Plates, with rates of 38–49 mm/yr [Hamling et al., 2015, Reyners et al., 2006]. The relative rotation of the Australia-Pacific plate slows down in rate and develops a greater parallel component southward along the New Zealand Zone. The oblique relative plate motion produces a margin-parallel [Mouslopoulou et al., 2007] and margin-normal [Walcott, 1998] component of motion, accommodating strike-slip faulting and rotation of the forearc, respectively. The national seismograph network of New Zealand has produced compilations of seismicity that have provided insight into the basic form of the subducted plate [Anderson and Webb, 1994]. The plate interface in Hawkes Bay on the East Coast is around 15 km deep and dips at a 10° angle to the northwest. Therefore, the coastal area is above the plate interface's seismogenic zone, which has the potential to produce powerful subduction thrust earthquakes [Hyndman et al., 1997]. According to both seismological and GPS data, the interseismic coupling at the seismogenic zone appears to be increasing southward [Reyners, 1998]. As a result, much of the forearc rotates clockwise at a rate between 1.6 and 3.8° Myr^{-1} as multiple, distinct tectonic blocks [Reyners et al., 2006]. Due to the forearc's rotation the northern part of the TVZ has seen an extension of backarc continental crust [Figure 1.1].

1.3.2 TAUPŌ VOLCANIC ZONE (TVZ)

The Taupō Volcanic Zone (TVZ), which is situated in the central North Island, is where most of New Zealand's volcanic activity takes place [Figure 1.2]. Taupō Volcanic Zone is a zone of active extension connected to the oblique subduction of the Pacific Plate beneath the Australian Plate, with a 300 km long (200 km onshore) and up to 60-km-wide extensional basin [Mouslopoulou et al., 2007, Wilson et al., 1995, Hamling et al., 2015], as defined by vent positions and caldera structural boundaries, and formed as a result of back-arc rifting. The TVZ is rifting at rates between 7 and 18 mm/yr [Wilson et al., 1995, Hamling et al., 2015]. Estimated from fault slip data, the late quaternary extension rates, depict that the rate of slip increases from 1.9 mm/yr at the surface to 3.6 - 10.2 mm/yr at seismogenic depths of 6 to 10 km. Five volcanic centres are found in the zone: Tongariro, Taupo, Maroa, Okataina, and Rotorua [Cole, 1979]. The Taupō Volcanic Zone, which was formed by crustal extension above the subduction zone, is separated into an old and young TVZ [see Figure 1.2]. The young TVZ is an actively rifting arc, widening at 7 mm/year to 15 mm/year and productive rhyolitic volcanism [Wilson and Rowland, 2016, Rowland and Sibson, 2004, Bibby et al., 1995].

TVZ is characterized by extraordinarily high heat flow and magma eruption rates, which result in geothermal waters with high temperatures. The majority of the volcanism in the TVZ is andesitic in the northern and southern regions, although rhyolitic volcanism predominates in the area in between [Bannister, 1992, Hurst et al., 2002, Hyndman et al., 1997]. This volcanism is seen in the central TVZ as many calderas have caused rhyolite eruptions [Figure 1.2]. TVZ is considered one of the most active rhyolitic systems on our planet, magma has been erupting from the central rhyolite-dominated part of the TVZ at an average rate of 0.3 $m^3 s^{-1}$ for the last 0.3 Myr [Bannister et al., 2004, Reyners et al., 2007, 2006]. Volcanic activity in the TVZ is characterized by rhyolitic eruptions that formed calderas and produced numerous ignimbrite flows that predominated the surface geology. The rhyolites exhibit no significant compositional changes through time, although the area of magma chamber zonation may have varied with the incoming rifting and crustal expansion in the recent 0.9 Ma [Wilson et al., 1995]. The TVZ is also characterized by an extremely high heat flow, with more than 20 high-temperature geothermal systems alongside these volcanic activities that discharge more than 4000 ± 500 MW of heat, an average heat flow of about 700 mW m^{-2} for the region [Bannister et al., 2004, Hurst et al., 2002, Reyners et al., 2007, Hyndman et al., 1997].

Numerous shallow earthquakes characterize the seismicity of the central part of the North

Island [Bryan et al., 1999, Anderson and Webb, 1994, Hurst et al., 2002]. The site of the most intense seismic activity occurs in the TVZ, which is delineated by the envelope of active volcanism during the last two million years [Bryan et al., 1999, Hurst et al., 2002]. There are steep gravity gradients of the eastern margin of the TVZ, from Mt Ruapehu to the Bay of Plenty, which is interpreted as the greywacke basement downfaulting to the northwest. The northwest margin lacks a distinct gravity gradient, but the southwestern margin is distinguished by a similarly strong gradient [Bryan et al., 1999, Hurst et al., 2002]. Until recently, it has been difficult to reliably pinpoint earthquakes due to the lack of many permanent seismometers in the region and the low-velocity surface layer that is both highly attenuating and varies in thickness [Bannister, 1992]. It is challenging to identify good focal mechanisms from the permanent seismic stations due to the shallowness of the seismicity. In the central TVZ, the only focal mechanisms available previously were composite ones that were obtained from earthquake swarms [Hurst et al., 2002]. These were mostly strike-slip mechanisms rather than normal mechanisms.

On the North Island of New Zealand, the shallow seismicity is dominated by the Hikurangi subduction zone and the rift region above it. The thickness of TVZ volcanic deposits is controversial because a subvolcanic basement has not been identified, although current data point to bulk quantities of 15 – 20,000 km^3, and has produced at least 10,000 km^3 of magma [Alloway et al., 2005]. The Whakamaru eruptions, which largely buried the evidence for earlier activity inside the zone, serve as a dividing line between the "old TVZ" from 2.0 Ma to 0.34 Ma and the "young TVZ" from 0.34 Ma onward in the history of the TVZ [Wilson et al., 1995, Hurst et al., 2016]. The young central TVZ is the most active and productive silicic volcanic, erupting rhyolite at a rate of around 0.28 $m^3 s^{-1}$, and data shows that this has been the case for at least the last 0.34 Myr [Wilson et al., 1995, Reyners et al., 2006]. According to seismic research, there are not enough detailed velocity estimates in the deep crust under the TVZ to distinguish between the various kinds of rocks, but they suggest that the base of the rocks has $v_p \simeq 6.1$ km s^{-1} [Reyners et al., 2006, Wilson et al., 1995]. Moreover, at this depth, there is an anomalous mantle with a different velocity v_p = 7.4 - 7.5 km s^{-1} [Rowlands et al., 2005, Hurst et al., 2016, Stern et al., 2010]. Despite fitting with theories of crustal thinning due to rifting or spreading in the TVZ, this oversimplified crustal model cannot adequately explain the complexity of the region. Seismicity in the upper crust is linked to low v_P/v_S (<1.70) within the TVZ [Reyners et al., 2007]. In northern Japan, similar low v_P/v_S ratios have been seen beneath active volcanoes; this can be explained by the presence of water [Nakajima et al., 2001]. In the lower crust of the TVZ, v_P/v_S increases rapidly, and the temperature sensitivity of attenuation Q_P is low (<300) [Reyners et al., 2007]. The low velocity v_P feature, which is centered close to 18 km deep, has been interpreted by Reyners et al. (2006) as an area of texturally equilibrated partial melt [Reyners et al., 2006, Hurst et al., 2016]. This interpretation is consistent with the low Q_P observed in this region.

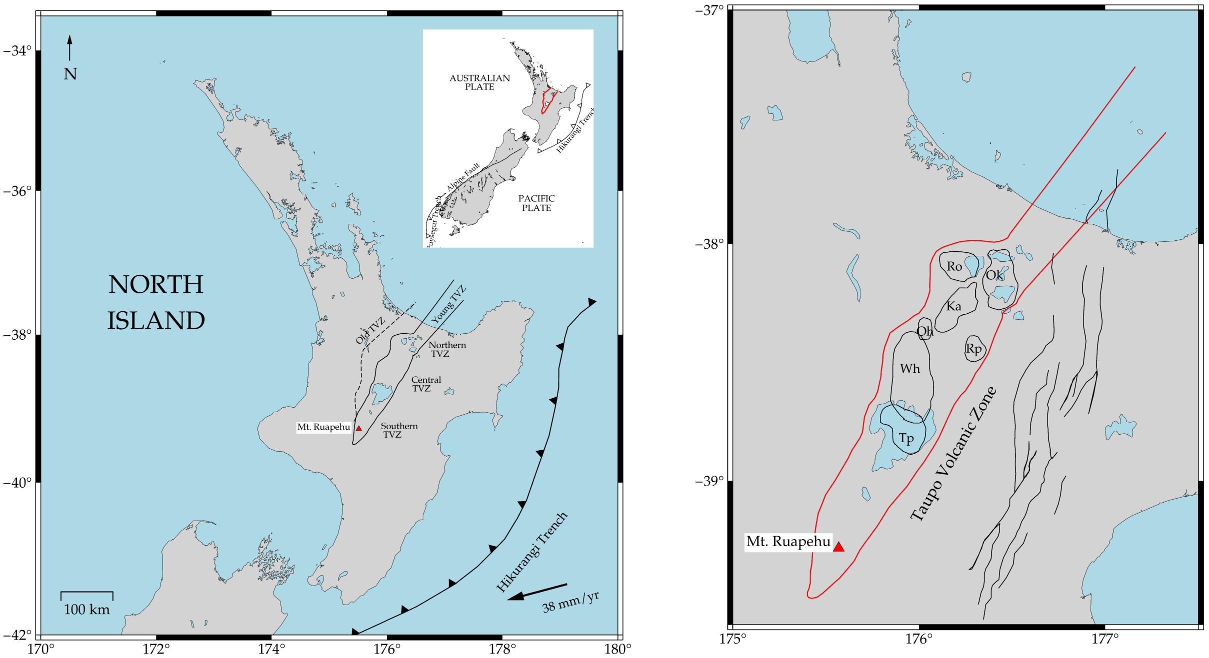

Figure 1.2: Various aspects of the geological features of New Zealand: a map showing the major faults across the country, an outline of the North Island showing the various regions of the Taupo Volcanic Zone (TVZ), both young and old, and a figure showing Mt Ruapehu and the calderas (black circles) within the TVZ.

According to both InSAR and vertical GPS data, the central TVZ is experiencing widespread subsidence at rates of up to 20 mm per year [Hamling et al., 2015]. Hamling et al. [2015] expects that the central TVZ would experience a yearly volume change of 0.011 - 0.016 km^3 as a result of the cooling and subsequent contraction of magma within the shallow crust. InSAR data shows a complex pattern of uplift or subsidence around the volcanic centre, these alterations could be brought on by the migration of the magma, intrusion into the hydro-thermal system, or contraction of molten rock underneath the volcanic zone causing it to cool down. Finding the underlying process can offer crucial insights into the magmatic plumbing system and the potential hazards associated with periods of unrest.

1.3.3 RUAPEHU VOLCANO

Mount Ruapehu is an active andesite-dacite stratovolcano with a volume of around 110 km^3 located at the southern terminus of the Taupo Volcanic Zone, Central North Island, New Zealand [Hackett, 1985, Leonard et al., 2008]. Ruapehu is characterized by high volcanism, crustal extension, and high heat flow [Hackett, 1985, Houghton et al., 1987, Hurst and McGinty, 1999]. Ruapehu's major peaks encircle a summit plateau that is $\sim$ 1 km^2 in extent and located at an elevation of over 2600 m. A severely acidic (pH $\leq$ 1) Crater lake [Ingham et al., 2009, Hurst et al., 2018] is located at the southern end this plateau at an elevation of 2540 meters, and is the surface manifestation of the volcanic—hydrothermal system. Based on stratigraphic research and geologic mapping, four distinct eras of cone construction have been identified, each spanning 104-105 years [Hackett, 1985]. Mount Ruapehu has not erupted since 2007 [Houghton et al., 1987]. The chronology of eruption events at Mount Ruapehu are 1969, 1971, 1975, 1977, 1978, 1979, 1980 and 1981-1982, 1985 and 1987 [Gamble et al., 1999, Sherburn et al., 1999]; these eruptions have caused damage or destruction to ski-field facilities, road and rail bridges, and parts of a large hydroelectric power project [Houghton et al., 1987]. Around 35 eruptions of Ruapehu have been documented since 1830, with the most recent one occurring in September 2007 [Hurst et al., 2018]. A significant amount of material around 0.1 km^3 has erupted during the two largest known historical eruptions, which occurred in 1945 and 1995–1996. Other historical eruptions, such as 2007, were much smaller [Kilgour et al., 2010, Gamble et al., 1999]. This indicates that the volcano has the capacity for both small and large eruptions. The greatest hazards at Ruapehu are the collapse of its fragile southeast wall or the renewed phreatomagmatic activity in Crater Lake [Houghton et al., 1987]. The times between eruptions can be as short as one to three years, however, and Ruapehu erupts on average roughly every 10 to 50 years [Leonard et al., 2008]. For phreatomagmatic eruptions, three categories of hazard zones may be identified: outside zones of service interruption due to fall deposits, inner zones of high danger from ballistic blocks and surges, and zones of risk from lahars [Houghton et al., 1987]. Ruapehu Volcano poses a risk from volcanic eruptions that produce ashfalls, pyroclastic flows, lava flows, sector collapses, and lahars [Houghton et al., 1987, Hodgson et al., 2007]. The most common and dangerous hazard at Ruapehu are lahars, due to the $9 \times 10^6\ m^3$ Crater Lake that covers the active venting zone at the southern border of the summit plateau [Hodgson et al., 2007]. Through recorded history, 151 people have lost their lives and infrastructure was damaged as a result of the lahars created by Crater Lake eruptions [Houghton et al., 1987, Hodgson et al., 2007].

The main characteristics of Ruapehu cone-building phase were mainly the changes in petrology and geochemistry brought about by discrete crystal fractionation, shallow magma mixing, and partial melting and assimilation processes [Kereszturi et al., 2021, Zellmer et al., 2021, Hodgson et al., 2007]. The mineral phases found in juvenile Ruapehu are Plagioclase, orthopyroxene, and clinopyroxene (A), while rare olivine undergoing peritectic reaction is mostly absent [Zellmer et al., 2021]. For Ruapehu Group, Hackett [1985] has suggested four new formation names, each of which denotes a cone-building phase over a time scale of $10^4 - 10^5$ years. The forms are Te Herenga, Wahianoa, Mangawhero, and Whakapapa, in order of age. Currently, the mountain's Te Herenga Formation, which comprises the oldest Ruapehu cone, is only weakly visible [Graham and Hackett, 1987]. Lavas from the Wahianoa Formation are primarily exposed in Ruapehu's south-east quadrant. Although the Wahianoa Formation's age is unknown, it is unquestionably older than the Mangawhero Formation, which it unconformably overlies [Graham and Hackett, 1987]. Five distinct vent locations produced the Whakapapa Formation's young (less than 15 ka) lava flows and pyroclastics, which all unconformably overlie deposits from earlier layers [Graham and Hackett, 1987]. According to Johnston et al. [2000], the historical explosions that occurred at Ruapehu featured small to moderate magnitude with a VEI > 3.

The first recorded seismic activity at Ruapehu occurred during the 1945 eruptions; however these data were never published [Sherburn et al., 1999]. In general, volcanic tremor is known as a quasi-continuous seismic signal generated by an active volcano, in contrast to earthquakes, which are often discrete events. Volcanic tremors and some volcanic earthquakes are alike to some degree, with tremors becoming less continuous and more like energy impulses. In the frequency domain, this translates to a shift from a spectrum characterized by narrow peaks to a broader spectrum that resembles the spectrum of a typical earthquake [Hurst and Sherburn, 1993]. Research on volcanic tremors has been focused on analyzing the 2 Hz tremor, which is Ruapehu's most frequent tremor [Hurst, 1992]. Even for a lag time longer than twenty seconds, the autocorrelation function of this signal exhibits a high degree of coherence and a strong peak in its spectrum. While the 2 Hz tremor and the 2 Hz volcanic earthquakes most likely come from the same source, the tremor is not caused by small volcanic earthquakes occurring repeatedly [Hurst, 1992]. Hurst and Sherburn (1993) demonstrated that the 2 Hz tremor is mostly propagated as Rayleigh waves and also proposed that it originates in a single-phase vapor zone below the vent under Crater Lake [Hurst and Sherburn, 1993, Sherburn et al., 1999]. Volcanic tremor at 3 Hz was frequent between 1985 and 1988 [Sherburn et al., 1999]. It was assumed that it had something to do with the source of extra heat input into the lake during heating periods [Sherburn et al., 1999]. The temperature records near the lake's surface indicated that it can change significantly in a matter of hours. It appears that some of these changes are due to disturbances in the lake's convective heat transport [Hurst, 1980]. Due to the frequency of these brief temperature changes, there is no clear and simple correlation between the temperatures in Crater Lake and Ruapehu's volcanic activity. However, as a result of releasing heat from Ruapehu into the lake, the lake's temperature serves as an indicator of Ruapehu's heat production and activity level. Only slight chemical variations are visible in water samples taken from various lake surface locations and depths: in 1966, samples taken from 25 meters down to 200 meters showed 3% variations in chloride concentrations while in 1970, samples taken at 0, 40, and 78 meters contained 11.45, 11.46, and 11.44 g/kg of chloride, respectively [Sherburn et al., 1999]. According to these results, the waters of Crater Lake are generally homogeneous and well-mixed.

1.3.4 UNREST AT NEW ZEALAND VOLCANOES

Volcanoes typically exhibit indicators of instability (unrest episodes) prior to eruption, which often consist of increased ground deformation [Passarelli and Brodsky, 2012, Hamling, 2021, Hamling et al., 2015], volcanic tremors [Hurst and McGinty, 1999], Seismic swarms, and geothermal system changes [Mannen et al., 2021]. Nevertheless, monitoring many volcanoes via ground deformation observations alone might be difficult because of their distant locations and hazardous environments [Hamling et al., 2015]. In New Zealand, volcanic behaviour is classified into background activity and unrest. Depending on how unrest is defined, the threshold takes into account the point at which background activity turns into unrest. There are two ways to characterize volcanic unrest [Potter et al., 2015a, 2014]. The first method places the activity level relative to the typical activity level of a particular volcano while the second method places the activity level relative to all volcanoes' activities. Volcanoes that have background activity, such as at Ruapehu with a continuously warm crater lake, active geothermal system, and high gas flux use the Volcanic Alert Level (VAL) system [Potter et al., 2014] which is based on 6 levels, which has a range of 0 (meaning "no unrest") to 5 (meaning "major volcanic eruption") and designed to characterize the current status of each active volcano [Table 1.1].

Status	**Alert Level**	**Volcanic Activity**	**Hazards**
Eruption	5	Major volcanic eruption	Eruption hazards on and beyond volcano
Eruption	4	Moderate volcanic eruption	Eruption hazards on and near volcano
Eruption	3	Minor volcanic eruption	Eruption hazards near vent
Unrest	2	Moderate to heightened volcanic unrest	Volcanic unrest hazards, potential for eruption hazards
Unrest	1	Minor volcanic unrest	Volcanic unrest hazards
No Activity	0	No unrest	Volcanic environment hazards

Table 1.1: Volcanic Alert Levels description

1.3.5 RECENT UNREST AT RUAPEHU - 2022 UNREST

Early in 2022, The Volcanic Alert Level was at Level 1 and the Aviation Colour Code was at Green since there was not much volcanic activity. On March 13 2022, a new heating cycle of Ruapehu Crater Lake began and was accompanied by an increase in seismic activity. Since the tremor levels had changed from weak to moderate [see Figure 1.4], the Volcanic Alert Level was raised to Level 2 and the Aviation Colour Code turned to Yellow on March 21. Eruptions are often more likely to occur when a volcano is at Volcanic Alert Level 2 than when it is at Volcanic Alert Level 1. This period between March and June at Ruapehu volcano in 2022 is considered consistent with moderate to high levels of volcanic unrest.

Ruapehu Crater Lake increased in temperature, reaching $\sim 40.77^{\circ}C$ on May 8th. The temperature then decreased to $\sim 21^{\circ}C$ on June 14th, followed by an increase to $\sim 25^{\circ}C$ during the next two weeks [see Figure 5.1]. During this unrest period, the lake colour shifted from the more typical grey hue seen in the previous few months to a blue-green, according to an observation conducted on November 22. The lake was full, however, there were sulfur slicks visible on the surface. No upwellings were noticed.

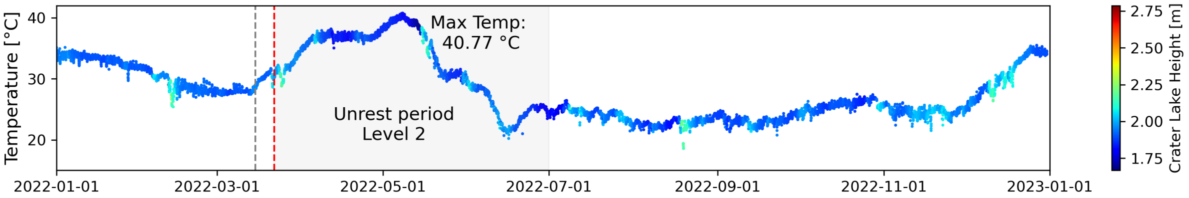

Figure 1.3: The figure displays the Crater's Lake temperature and level at Ruapehu volcano for 2022. The gray-colored box indicates the duration of the unrest period. The red and gray lines represent the start of the unrest and the period of heightened lake temperature, respectively.

The level of tremors or types of volcanic earthquakes [see Figure 1.4] also increased during this period, and intensified on March 20. The recorded tremors varied, with strong tremors interspersed by short periods of weaker activity. A rise in gas emissions, including sulfur dioxide, was also observed during the unrest in 2022. The gas measured on April 28th, at 390 tonnes per day, showed the sixth-highest SO_2 flow since 2003.

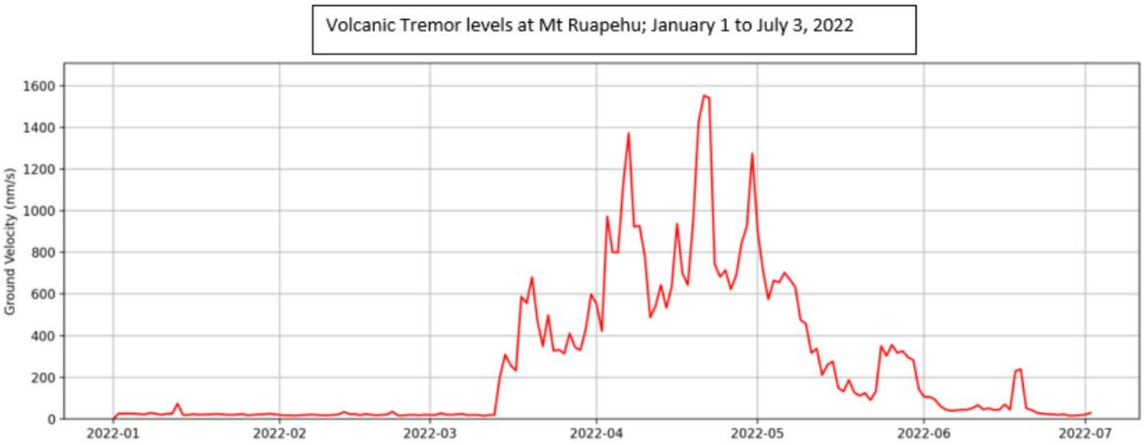

Figure 1.4: The level of volcanic tremor at Mt. Ruapehu, 2022 from GNS volcanic activity bulletin RUA-2022/18 (https://www.geonet.org.nz/vabs/6ek5OkTf13CM9BqY538frb)

Early in July, when seismic activity and the heat cycle returned to their usual mean values, the Alert level dropped to Level 1. The monitoring data does not reveal which mechanism is causing the unrest during this period. If velocity changes are shown to be a reliable monitoring technique at Mt. Ruapehu, it will be able to predict the next eruption before it occurs by monitoring and understanding what causes the unrest episode there.

CHAPTER 2

BACKGROUND THEORY

The objective of this chapter is to discuss the background theories that underpin this thesis. Green's function and its recovery are covered in Section 2.1. The topic of ambient noise wavefield is discussed, including what it is, and how recent developments have made it possible for us to use it as a tool for subsurface monitoring [Section 6.1.2]. Section 2.4 discusses the application to ambient noise and how this tool can be used to determine changes in seismic velocity.

2.1 GREEN'S FUNCTION RECOVERY

Seismic interferometry is a method based on the cross-correlation of two seismic waves from two different stations recorded and was presented as a means of obtaining information on the physical characteristics between these receivers called Green's function [Wapenaar et al., 2010]. Applications of Green's theorem in seismic processing are reviewed by Ramírez and Weglein [2009]. Aki [1957] was the first to demonstrate that seismic noise could be utilized to extract information about the propagation media, which led to early breakthroughs in seismic interferometry. Later, Claerbout [1968] showed that the autocorrelation of signals at the surface might be used to estimate the impulse response of a medium. It has been found that Green's function is recoverable over a wide variety of length scales, from a few kilometers [Sabra et al., 2005] between seismic stations to thousands of kilometers [Bensen et al., 2008, Yang et al., 2007]. As a result, the technique is now widely used for seismic tomography [Yang et al., 2007]. Accurate recovery of the Green's Function usually requires sufficiently long recordings of the ambient noise signal and the noise must travel randomly in a complex scattering way on Earth. For tomography-based work, which usually employs noise recordings on the order of years, this is not an issue. On the other hand, smaller noise recordings are needed to repeatedly compute cross-correlation functions utilizing noise records at different periods, which is necessary for monitoring temporal velocity changes. It has been shown that small changes in velocity may be monitored without a complete reconstructing of the Green's Function. Rather, the most crucial need for lowering errors in measurements is the stability of noise sources [Hadziioannou et al., 2009].

The concept of seismic interferometry is applied to create new seismic responses of virtual sources by cross-correlating seismic measurements at different receiver locations [Wapenaar et al., 2010]. The energy that travels between the two stations is added constructively if the cross-correlation is stacked together; otherwise, the energy that comes indirectly is added destructively. Particularly for ambient noise, the cross-correlation result is roughly the Green function between the two stations, which is dominated by surface waves. An illustration to explain the principles of seismic interferometry is provided in Figure 2.1. This method involves cross-correlation as discussed in [Chapter 3.4]. We begin our discussion of seismic interferometry by taking a close look at a synthetic example of direct-wave interferometry. Figure 2.1a shows a direct path wave that travels between A and B from a random source. We assume that the medium is lossless and that the propagation velocity, c, is constant. Along the propagation path, there are two receivers: A and B. Figure 2.1b shows the synthetic response observed by receivers A and B, and the cross-correlation of these two receivers. A synthetic response was created to simulate the ambient noise that is recorded by a receiver as shown in Figure 2.1b. The response is denoted as G($x_{A,B}$,x_s,t), where G stands for the Green's function. The Green's function consists of an impulse at $t_A = (x_A - x_s)/c$; therefore, $G(x_A, x_s, t) = \delta(t - t_A)$, where $\delta(t)$ is the Dirac delta function. Similarly, the response at x_B is given by $G(x_B, x_s, t) = \delta(t - t_B)$, with $t_B = (x_B - x_s)/c$. The cross-correlation of responses at two receivers, in this example at x_A and x_B, is an important step in seismic interferometry. Looking at Figure 2.1b, the raypaths associated with $G(x_A, x_s, t)$ and $G(x_B, x_s, t)$ have the path from x_S to x_A in common. In the cross-correlation process, the travel time along this common path cancels, leaving the travel time along the remaining path, which is $\Delta t = t_B - t_A = (x_B - x_A)/c$, from x_A to x_B. The receiver at x_B would recode the same impulse response as the receiver at x_A but would be shifted by the same amount of time t_s, which would be cancelled in the cross-correlation. The cross-correlation of the impulse responses at x_A and x_B are defined as:

$$G(x_A, x_s, t) * G(x_B, x_s, t) = \int G(x_A, x_s, t + t')G(x_B, x_s, t')dt' \tag{2.1}$$

Substituting the delta functions into the right-hand side gives:

$$\delta(t + t' - t_B)\delta(t' - t_A)dt' = \delta(t - (t_B - t_A)) = \delta(t - (x_a - x_B)/c) \tag{2.2}$$

This is the Green's function $G(x_B, x_A, t)$, propagating from x_A to x_B. This expresses the principle that the response at one of two receivers, x_B, may be obtained from the cross-correlation of observations at those two receivers (x_A and x_B) as if a source were present at the other receiver, x_A. It also demonstrates why seismic interferometry is often called Green's function retrieval. The Green's function representation is as follows:

$$G(x_B, x_A, t) = G(x_B, x_s, t) * G(x_A, x_s, -t) \tag{2.3}$$

The source isn't always an impulse. Suppose a wavelet is used as the source function rather than an impulse. In that case, the Green's function between two receivers may be obtained by the cross-correlation of their responses, convolved with the auto-correlation of the source function [Wapenaar et al., 2010].

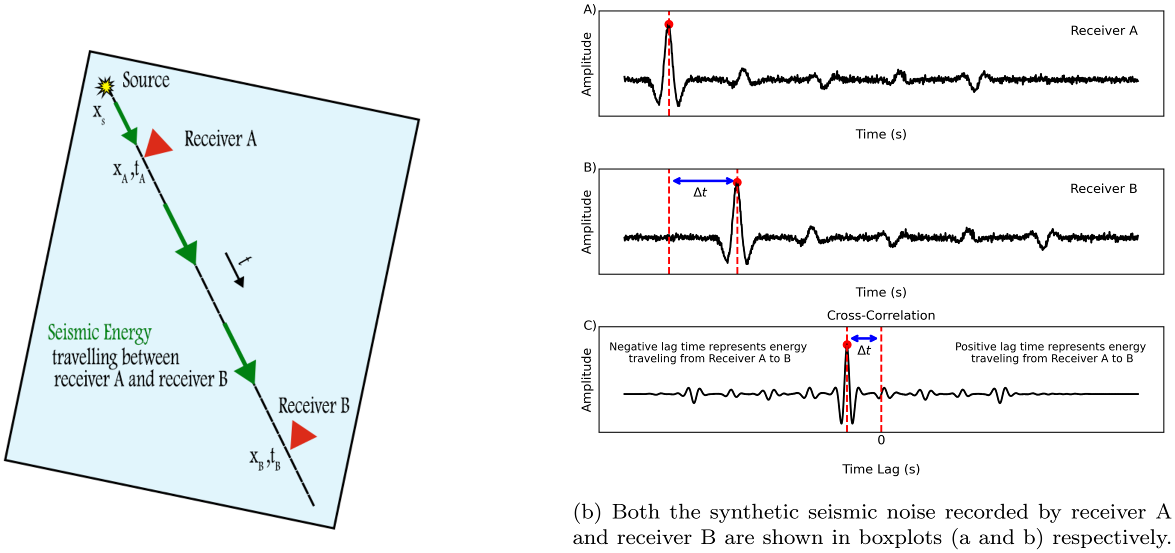

(a) Seismic energy travels on a direct path between receivers A and B.

(b) Both the synthetic seismic noise recorded by receiver A and receiver B are shown in boxplots (a and b) respectively. (c) The transit time (time delay) of the coherent energy between two stations is calculated by cross-correlating the two time series (A and B).

Figure 2.1: This figure illustrates the cross-correlation concept using synthetic data.

2.2 AMBIENT NOISE INTERFEROMETRY

The conventional view of noise (seismic, acoustic, etc.) is that it is a random, unwanted signal that appears above the desired signals. Several earlier investigations offered a new understanding of this noise, revealing its use in applications [Claerbout, 1968]. There are many different sources of noise, including anthropogenic sources from industrial machines and automobiles as well as natural sources such as air pressure changes and tides from wind and ocean movements. Gutenberg [1958] compiled a list of sources categorized by frequency and demonstrated that noise at high frequencies above 1 Hz is often generated by anthropogenic (human activity) sources, whereas noise at lower frequencies, less than 1 Hz, originates naturally from sources such as ocean waves. Cross-correlation of recorded ambient waves to recover Green's function is referred to as a passive technique as no active source (such as man-made explosions, earthquakes, or volcanic eruptions) is required [Clarke et al., 2011, Wapenaar et al., 2010]. One of the most important factors in using ambient noise for extracting the Green function and revealing the characteristics of the crust and upper mantle structures is the ability to process ambient seismic signals, extracting signals of interest while suppressing signals of disinterest like earthquake signals, instrument irregularities, and non-stationary noise sources close to the stations [Anggono et al., 2012, Shapiro et al., 2005]. The ambient noise interferometry method has been shown to be reliable for retrieving Green's function between two receivers in the absence of an active source [Nooghabi, 2018, Clarke et al., 2011]. The importance of applying the Cross-Correlation approach to diffuse waveforms like ambient noise and scattered coda waves has been demonstrated in several studies [Wapenaar et al., 2010, Ramírez and Weglein, 2009, Aki, 1957]. With the help of this approach, we may estimate the Green function between two stations while being given information about the subsurface features.

2.2.1 AMBIENT NOISE

In seismology, two types of signals have been considered to create random wavefields. Seismic coda wavefields are the first type that results from the effect of repeated scattering of seismic waves by small-scale inhomogeneities in the lithosphere. Ambient seismic noise is the second type of signal. The advantage of ambient noise over seismic coda is that ambient noise is continuously recorded in space and time, and is not dependent on the occurrence of earthquakes [Yang and Ritzwoller, 2008, Clarke et al., 2011]. The study of seismic ambient noise dates back to the early days of seismology, primarily due to the requirement to improve the level of detection of deterministic arrivals. From early studies such as Gutenberg [1958], It was recognized that the origin of the ongoing disturbance of the earth's surface varies depending on the frequency range [Hechels, 2017]. The cause of high frequency noise (>1 Hz) is typically human activities (e.g., traffic, machinery). The energy of these signals varies significantly over time and is associated with daily and weekly periodicities in human activity. In contrast, the relationship between amplitude and meteorological conditions allowed identify the natural source of ambient noise over extended periods. The frequency defining the human activity domain depends on local conditions [Bonnefoy-Claudet et al., 2006]. Microseisms often refer to the background noise in the range of 0.3 Hz to 0.05 Hz. Two strong peaks of the short-period seismic noise are typically observed in the primary (10–20 s) and secondary (5–10 s) microseism bands [Yang and Ritzwoller, 2008]. Microseisms have large amplitudes that make it challenging to detect the weak arrivals caused by earthquakes. The noise in the microseism spectral band is mostly dominated by surface waves, primarily Rayleigh waves [Toksöz and Lacoss, 1968]. Despite this, there is evidence of the presence of body waves dominating the noise between 0.4 and 0.8 Hz [Vinnik, 1973]. Early on, it was discovered that there is a coincidence between periods of strong microseisms and high surges that reach the coastline [Gutenberg, 1958].

Long periods (> 50 s) of ambient noise, often called hum, have the spectral structure of Earth's free oscillations [Tanimoto et al., 1998, Xie et al., 2016]. It is assumed that the interaction between the solid Earth and the infragravity waves of the ocean causes this excitation [Xie et al., 2016, Hasselmann, 1963]. This mechanism has been confirmed by the link between large wave height regions and the apparent locations of hum sources [Bromirski and Gerstoft, 2009]. The generation of background ambient noise at long periods occurs both in deep oceans and coastal areas.

Ambient noise is known as the seismic energy signal that travels through the Earth but is not produced by active sources. Along its travel path, this noise records the velocity structures of the ground and other subsurface features, and it is possible to estimate the velocity of the structure between two sensors at any time from the ambient noise extracted from the waveform data. Therefore, information on the velocity structure may be obtained without an active seismic source. Seismic noise has emerged as a very promising field of study in recent times, owing to its ability to overcome the constraints imposed by dependence on the occurrence of seismic events. These constraints are overcome through seismic Green's functions that are obtained by computing the cross-correlation (cc) of records of a random seismic wavefield acquired at various locations within a region of interest [Clarke et al., 2011]. The ambient noise recorded by station pairs is cross-correlated to obtain an impulse response that provides information on the subsurface velocity structure. However, cross-correlations can greatly lower the likelihood of obtaining a reliable impulse response between the two sensors if the ambient noise is not generated by randomly distributed homogeneous sources. Section 3.4 discusses the cross-correlation technique.

2.2.2 MEASURING SEISMIC VELOCITY VARIATION BASED ON AMBIENT NOISE

It has been demonstrated both theoretically and experimentally that utilizing ambient noise to monitor seismic wave velocity changes is a useful technique for examining variations in the stress state of the crust [Wang and Yao, 2020]. As a result, we can track how the seismic wave velocity varies over time. We can study the stress state of the crust at depth and continuously over time by measuring variations in seismic velocity [Wang and Yao, 2020, Nur, 1971]. This can provide information on dynamic processes occurring in the crust, such as those caused by earthquakes, volcanoes, and other activities. The ambient noise-based monitoring technique may also be used to monitor the changes in subsurface velocity caused by environmental changes. The seismic velocity travelling along the Earth's surface is very sensitive to small perturbations in the elastic properties of the crust, it is possible take advantage of the sensitivity to estimate the seismic structure [Aki, 1957].

The basic concept behind employing seismic noise to track changes in seismic velocities is to compare "current" cross-correlation functions (CCFs) that depict the situation at a given time period with "reference" cross-correlation functions (CCFs), that represent the average background state of the medium [Clarke et al., 2011]. Coda wave interferometry is the conventional technique for measuring seismic wave velocity using ambient noise. This method, which was first presented by Poupinet et al. [1984], involves analyzing the subtle phase shifts in waveforms that occur between earthquake doublets along seismograms. This idea was developed further by Snieder et al. [2002], who suggested a similar technique for measuring time changes by using different lag time moving windows. To estimate the seismic velocity variation, let us consider a reference medium where the seismic wave propagation path is $d = vt$, where d is the path's length, v is the seismic wave's velocity, and t is the propagation time.

Assuming that the path remains unchanged and a homogenous velocity variation in space δv, then:

$$d = vt = (\delta v + v)(\delta t + t) \tag{2.4}$$

This results to first order

$$\frac{\delta t}{t} = -\frac{\delta v}{v} \tag{2.5}$$

where $\delta v/v$ denotes the relative velocity change and δt is the propagation time variation brought on by the velocity variation. Therefore, one may estimate the relative velocity variation by measuring the relative travel time shift between the reference "CCF" and the current "CCF". This is the basis for very accurate measurements of the velocity change with coda waves. Moving-window cross-spectral analysis, or MWCS, is a linear regression technique that was introduced by Snieder et al. [2002], Poupinet et al. [1984] to measure δt in moving windows along seismograms and evaluate $\delta v/v$. Section 2.3 discusses moving-window cross-spectral analysis (MWCS).

To monitor small changes in velocity, the stretching approach optimizes a stretching parameter ϵ. Using this procedure, the seismic trace is deformed by setting the time variable (t) to a new value ($t' = t(1 - \epsilon)$). Using varying stretching factors (ϵ), the technique includes interpolating the coda at different times ($t(1 - \epsilon)$). The actual relative velocity change ($\epsilon_0 = \delta v/v$) can be estimated by maximizing the cross-correlation coefficient between the traces collected before and after the velocity shift. The stretching approach is especially useful for data with low signal-to-noise ratios when true global velocity variations are present [Hadziioannou et al., 2009].

Studies showing the use of ambient noise for monitoring of environmental processes are increasing, as it has been shown that a variety of natural events can cause measurable changes in seismic velocity. These include short and long-term volcano activity related to deformation [Brenguier et al., 2008a, Obermann et al., 2013a, Rivet et al., 2014, Mordret et al., 2010], large earthquakes [Minato et al., 2012, Madley et al., 2021], and some activities linked to environmental factors (e.g. rainfall or atmospheric pressure changes) [Sens-Schönfelder and Wegler, 2006, Silver et al., 2007, Hillers et al., 2015]. In volcanic regions, significant changes in the seismic velocity may be inferred as a result of local volcanic processes occurring prior to eruptive activity [Mordret et al., 2010]. These velocity variations typically have a magnitude of 0.1% or less [Sens-Schönfelder and Wegler, 2011].

2.3 MOVING WINDOW CROSS SPECTRUM (MWCS) ANALYSIS

The MWCS approach was the first presented by Poupinet et al. [1984] for retrieving relative velocity changes between earthquake doublets. Brenguier et al. [2008a,b] used this method to apply it to seismic noise data [Gouédard et al., 2008]. An important method in monitoring the variation in the subsurface properties of the Earth using seismic noise data is Moving Window Cross Spectrum (MWCS) analysis, which provides a special lens through which to study the temporal changes in the relative dephasing between seismic signals. This analysis is performed on time series that are generated for every possible pair of seismic stations by cross-correlating the noise sequences that were collected at those stations [Lecocq et al., 2014, Clarke et al., 2011]. Creating many current cross-correlations and at least one reference [see Section 3.5]. A certain number of single cc's must be stacked since the continuous noise records are divided into short sequences (e.g. one for each day or hour).

The method consists of two phases for any pair of reference and current stack functions. The first stage is seismic data time series split into overlapping windows using the moving window approach [Clarke et al., 2011]. Then, calculating the time-delay between these sequences of overlapping windows. The windows' overlap minimizes artifacts at window boundaries and ensures continuity. The seismic waves may be whitened before doing cross spectrum analysis [see Section 3.3]. Evaluating the relative velocity variation linked to the current function in relation to the reference is the second stage. For simplicity, it is assumed in this second stage that the examined media's seismic wave propagation velocity is disturbed uniformly [$\delta v/v = \delta t/t =$ Const.].

It is important to note that the first stage is executed in the spectral domain. In the phase of the cross spectrum analysis, the Fourier transform of two seismic signals is computed, and the complex conjugate of one signal is then multiplied by the other. The coherence between signals is calculated by measuring the normalized cross-spectral power of the two signals. A high degree of coherence suggests a correlation between the two signals. Every calculated delay time has a corresponding cross-correlation lag time, which serves as the central point of the window [Clarke et al., 2011]. Consequently, the second phase entails estimating the relative time delay $\delta t/t$ across the entirety of the signals. The time delay between the two signals is represented by a slope of regression line [Lecocq et al., 2014] [see Figure 2.2]. Measuring the lag times at every window provides information insight into how the delays between signals change over time. The relative homogeneous velocity perturbation of the current cross-correlating stack with respect to the reference cross-correlating stack is, to a first approximation, indicated by the slope of their linear regression [Clarke et al., 2011] [see Figure 2.2, see Section 3.6].

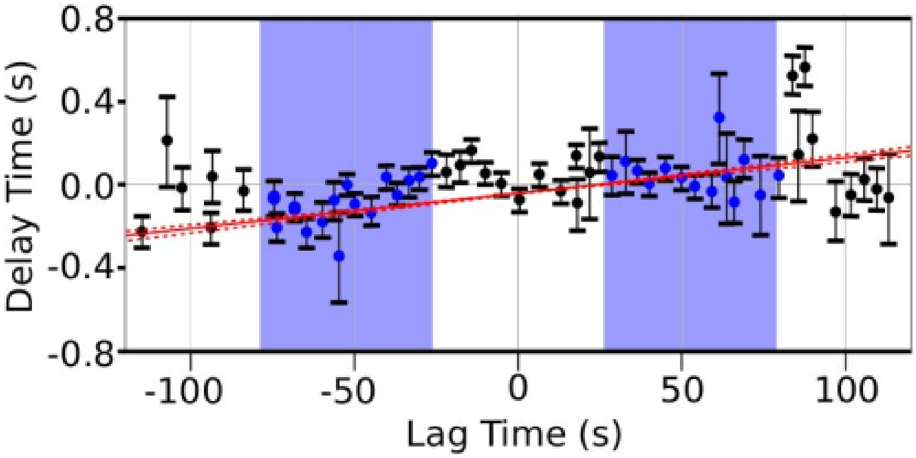

Figure 2.2: An example of a moving-window cross-spectral analysis fitted to delay values taken from [Kortink, 2020], showing the slope (red line) and its uncertainty (dashed red lines). The lowest and maximum lag periods at positive and negative delays are indicated by shaded blue boxes.

2.4 MONITORING VOLCANOES WITH AMBIENT NOISE

Studying the temporal variations of crustal structure associated with seismic and volcanic activity is becoming an increasingly popular field of Earth science research. This study contributes not only to fundamental geological understanding but also to the development of improved models for seismic hazard assessment and volcanic monitoring [Poupinet et al., 1984, Mordret et al., 2010]. Nowadays, many techniques have been used to identify changes in the crust around volcanoes; such as surface deformation [Cayol et al., 2000, Lu et al., 2000], anisotropy [Savage et al., 2015, Gerst and Savage, 2004], investigation of volcanic and long-period earthquakes [Aki and Ferrazzini, 2000, Chouet et al., 1994], and velocity changes studies [Mordret et al., 2010, Bennington et al., 2015, Wang and Yao, 2020]. The sensitivity to changes at depth and the continuity of the dataset are the main advantages of employing ambient noise over some of the other approaches mentioned. The physical mechanism of temporal changes in volcanic systems will be covered in Section 2.4.1, and some findings from related research are presented in Section 2.4.2.

2.4.1 PHYSICAL MECHANISM

The characteristics of volcanic eruptions indicate that they are not like other tectonic events. Three types of seismic signals are often used to describe volcanic earthquakes that are not directly associated with eruptions: Type A events, seismic characteristics of high-frequency (>10 Hz) are similar to those of tectonic earthquakes. Signals from type B events have a low-frequency content, often between 0 and 5 Hz. Type C events, harmonic tremors are defined as persistent low-frequency (0 to 10 Hz) ground vibrations that endure for a few minutes to many hours [Ferrick et al., 1982, Aki et al., 1977]. The origin of low-frequency volcanic earthquakes is controversial. Some theories of the origin of the tremors are free oscillations of a magma chamber, oscillations of gas in a volcanic vent [Steinberg and Steinberg, 1975], oscillation of volcanic layers from flowing magma, and random opening of tensile fractures from excess fluid pressure [Aki et al., 1977, Aki and Koyanagi, 1981]. These hypotheses all suggest that source effects are what produce tremors.

Many studies have been conducted on the effects of stress on seismic velocities in dry rock at pressures and temperatures that mimic shallow crustal conditions [Wang and Yao, 2020, Nur, 1971, Lockner et al., 1977]. However, our understanding of the processes underlying attenuation is lacking. At relatively low temperatures and pressures, cracks are assumed to be the source of the dissipation that produces seismic attenuation in rock [Lockner et al., 1977]. Microcrack distribution is commonly hypothesised as the source of seismic velocity changes in volcanic zones [Nur, 1971]. These changes result from the material interacting with its surroundings and variations in the stress field at depth as it ascends [Ratdomopurbo and Poupinet, 1995]. Laboratory experiments have demonstrated that seismic velocities increase when microcracks close and become stiffer as a result of pressure rise [Nur, 1971]. According to sample observations made by Nur and Simmons [1969], Lockner et al. [1977], velocity increases parallel to the applied stress axis as uniaxial stress increases, and this increase is significantly larger than the increase in directions normal to the axis. The magnitude of this increase is dependent upon the angle formed by the stress and the direction in which the compressional wave propagates [Nur and Simmons, 1969]. Such a larger pressure and a new deformation may result in the creation of new cracks surrounding rock, such damage would lower the seismic velocity [Nur and Simmons, 1969, Lockner et al., 1977].

2.4.2 PREVIOUS STUDIES

A possible monitoring technique for volcanoes is the measurement of seismic velocity by passive interferometry utilizing seismic noise. This method is sensitive to magma pressurization and the redistribution of melt within a subsurface plumbing system [Donaldson et al., 2017]. Monitoring changes in seismic velocity at the volcanic zones has been the focus of several studies [Clarke et al., 2011, Mordret et al., 2010, Meier et al., 2010, Daskalakis et al., 2016]. Improved monitoring utilizing volcano velocity change monitoring could improve hazard resilience if we had a thorough understanding of what is happening in the volcanic zones, what causes the velocity changes before eruptions, and if these changes in velocity are indicative of an eruption. Here, a summary of the primary causes of changes in seismic velocity, which include earthquake coseismic and postseismic procedures, pressure buildup, magma migration within the volcanic area, environmental perturbations and activities occurring within natural and man-made reservoirs is presented. A selection of representative noise-based monitoring studies with various forcing sources in this part was represented.

A number of recent studies have demonstrated the decrease of velocity correlated with fault system activity, earthquakes, and transient creep [Aki and Ferrazzini, 2000, Chouet et al., 1994, Brenguier et al., 2008a]. A partial postseismic recovery after a quick coseismic velocity drop was observed following several large earthquakes in Japan [Hobiger et al., 2016]. The 2003 San Simeon and the 2004 Parkfield earthquakes enhanced non-volcanic tremor activity along the San Andreas Fault and decreased seismic velocities [Brenguier et al., 2008a]. These two earthquakes in the San Andreas fault zone were linked to a velocity drop ($\sim 0.08\%$) that was observed by Brenguier et al. [2008a]. This drop was interpreted as the result of deep coseismic stress change and postseismic stress relaxation within the fault zone, as well as coseismic damage in the shallow layers [Brenguier et al., 2008a, Wang and Yao, 2020]. Research on the M_w 9.0 Tohoku-Oki earthquake that occurred offshore of Japan in 2011 revealed a $\sim 1.5\%$ drop in seismic velocity in the area nearest to the mainshock [Minato et al., 2012]. After the earthquakes, a gradual healing process was displayed. In addition, a decrease was observed following Japan's M_w 6.6 mid-Niigata earthquake [Sens-Schönfelder and Wegler, 2006]. The change in velocity is not only related to the response of the sallow layers but also associated with the earthquake.

Another crucial application is monitoring changes on a relatively small scale in volcanic zones. Brenguier et al. [2008b] first observed alterations caused by ambient noise at the Piton de la Fournaise volcano, La Réunion Island. Analyzing 18-month data, they observed a clear indication that short-term velocity decreases in the interior of the Piton de la Fournaise volcano of about $0.05 - 0.1\%$ occur a few weeks to a few days prior to the major eruption on April 2, 2007. Seismic velocity decreases before the eruptions indicate pre-eruptive inflation of the volcanic edifice, most likely as a result of elevated magma pressure [Brenguier et al., 2016, Wang et al., 2019]. In addition, the deformation observations from InSAR and GPS showed that a simultaneous seismic velocity drop occurred before the eruption with a widespread flank movement when magma was injected to feed an initial eruption [Clarke et al., 2013, Brenguier et al., 2008a]. This proved that ambient noise could be used as a predicting tool for eruptions and, made Piton de la Fournaise volcano a focal point for ambient noise-based volcano monitoring, and this raised the question of whether the behaviours of all volcanoes are the same.

The number of volcanoes where seismic velocity changes have been studied with ambient noise is still increasing. Examples include the Kilauea volcano in Hawaii [Donaldson et al., 2017], Ruapehu volcano [Mordret et al., 2010] and White Island (Whakaari) Volcano [Yates et al., 2019] in New Zealand , Okmok volcano in Alaska [Bennington et al., 2015], and Miyakejima volcano in Japan [Anggono et al., 2012]. Mt Ruapehu exhibited a significant 0.8% seismic velocity reduction in the edifice two days prior to the phreatic eruption in 2006 [Mordret et al., 2010]. Mordret et al. [2010] interpreted the drop in velocity attributed to a pressure buildup in a magma pocket beneath Ruapehu's east flank as a result of new magma flowing into a small reservoir. This increasing pressure caused open cracks, which in turn caused a localized decrease in seismic velocity. In contrast, no significant change in the velocity related to the 2007 eruption was observed [Mordret et al., 2010]. This might be attributed to the different pressurization time scales for the two events (October 2006 and September 2007 eruption) as well as the low temporal resolution. In 2000, the Japanese volcano Miyakejima displayed intriguing volcanic activity [Anggono et al., 2012]. The study revealed both increases and decreases in seismic velocity. There was a 3.3% increase in seismic velocity at the volcanic edifice on the flanks while the areas around the collapsed caldera saw a 2.3% drop. For a better comprehension of the velocity increase and decrease, Anggono et al. [2012] examined several potential mechanisms of the velocity changes, including stress changes, caldera formation, and topographic changes. The results indicated that the compression brought on by the deflation sources connected to magma activity in 2000 might account for the observed increases in seismic velocity. However, the drop could also be attributed to topographic changes brought about by a caldera. Similar to the volcano Miyakejima, the

Hawaiian Kilauea volcano has recorded both increases and decreases in velocity [Donaldson et al., 2017, Anggono et al., 2012]. This can be interpreted as indicating distinct deformation patterns with regions experiencing deflation-inflation events based on the source's relative position.

In addition to seismic velocity variations caused by tectonic and volcanic activity, environmental perturbations originating from many sources can have an important impact on seismic wave velocity. Rainwater infiltration causes (delayed) increases in pore pressure in the crust when rainfall rises [Hillers et al., 2015]. In the end, this results in a decrease in the shear modulus, which also lowers the seismic wave velocity [Wang and Yao, 2020]. Seismic velocity declines associated with groundwater and rainfall, which can reach $\sim 0.2\%$ to 0.1%, have been widely discussed as evidence of the significance of hydraulic impacts on seismic wave velocity [Sens-Schönfelder and Wegler, 2006, Meier et al., 2010, Tsai, 2011, Hotovec-Ellis et al., 2014]. Using data from Merapi volcano, passive image interferometry revealed velocity changes of 0.1% at a temporal resolution of one day. Based on precipitation, Mt. Merapi's velocity changes exhibit a major seasonal effect. Sens-Schönfelder and Wegler [2006] demonstrate that hydrological circumstances may alter seismic velocities by more than 10% in a depth range [Sens-Schönfelder and Wegler, 2006]. Moreover, the shallow layer seismic wave velocity is affected annually by variations in air pressure, thermoelastic stress [Lecocq et al., 2017], sea surface height, precipitation, and snowfall [Donaldson et al., 2017]. Research was conducted in Germany to study the groundwater effect on velocity changes [Lecocq et al., 2017]. In their study, thirty years of continuous data were used, and observed velocity changes of approximately 0.01% of the surface waves. The velocity changes can be interpreted as impacts of temperature diffusion and water storage changes.

CHAPTER 3

METHODOLOGY

This chapter will cover the instrumentation and data acquisition [Section 3.1], processing techniques [Section 3.2], data pre-processing [Section 3.3], cross-correlation [Section 3.4], moving and reference stacks [Section 3.5], velocity calculations [Section 3.6], and parameter justification in this investigation [Section 3.7]. A portion of this study is focused on the processes and explanations for the parameters used in the computation of seismic velocity variations were discussed.

3.1 INSTRUMENTATION AND DATA ACQUISITION

Raw seismic data is obtained through the International Federation of Digital Seismograph Networks (FDSN), downloaded in MSSED format using the Python package Obspy [Krischer et al., 2015]. The dataset used in this thesis comprises eight broadband stations and six short-period sensors located around Ruapehu volcano. Data was obtained from GeoNet between January and December of 2022 for the vertical components with a sampling frequency of 100 Hz. The different station pairs [Figure 3.1] chosen for this study had interstation separation distances ranging from 2 km to 26 km, figure 3.1 also shows the cross-correlation raypath coverage between all station pairs. These stations were chosen by their location to Ruapehu. Due to the small number of broadband instruments across Ruapehu and to acquire good coverage of the study area we also have used data from short-period instruments surrounding Ruapehu. The availability of data for the seismic stations in this study is displayed in Figure 3.2 across the studied time period. The gaps in the figure show the station was not recording during that period. One important step in the MSNoise process is to make sure the data is continuous and gap-free. Once any gaps are identified, the data must be processed to make it as continuous as possible. To do this, the daily traces are split into equal length segments. After that, the segments are merged into continuous day-long segments.

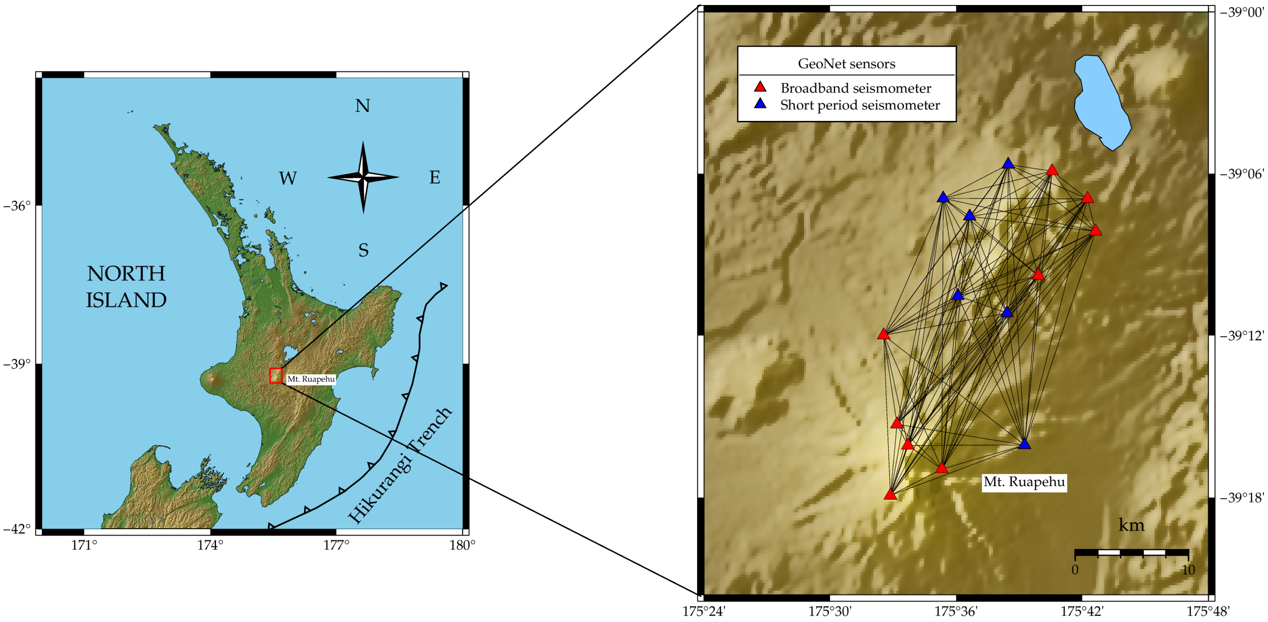

Figure 3.1: Map showing station locations and cross-correlation raypath coverage between station pairs.

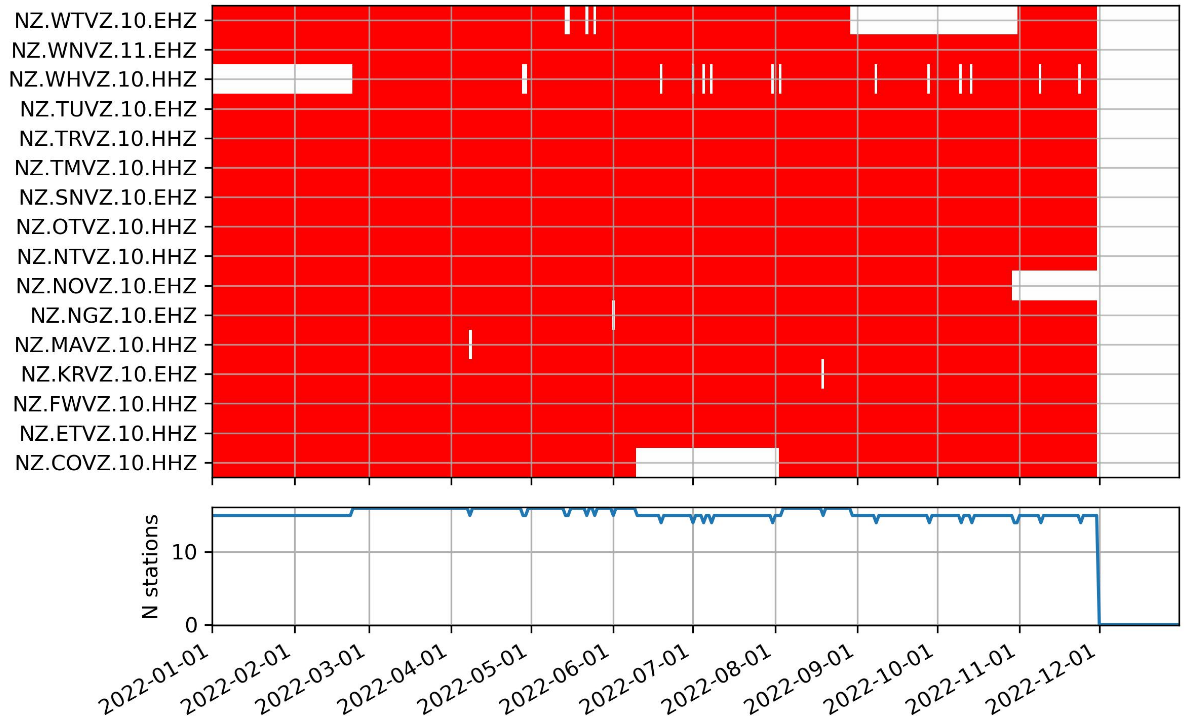

Figure 3.2: Station data availability. Stations are listed on the left with duration at the bottom. Data availability, as recorded in the database, is indicated in red. Days with no data remain blank. The number of operating stations is displayed in the lower chart.

3.2 DATA PROCESSING

In this study, I used the software MSNoise which handled a large portion of the data processing for this study, mostly using the techniques described by Bensen et al. [2007]. MSNoise is an open-source and free Python package developed by Lecocq et al. [2014] to process and recover velocity changes. As shown in Figure 3.3, computing temporal velocity changes using an ambient noise processing procedure is divided into four phases. These procedures are: [**Phase 1**] pre-processing raw data, a single-station data preparation step that involves removing the instrumentation response, the mean, the trend, and cutting the data to the chosen time frame. The data is then normalized in the time and frequency domains to prevent earthquake signals. In [**phase 2**] cross-correlation functions (CCFs) of the ambient seismic noise for each pair of seismic stations are computed. In [**phase 3**] these cross-correlations are stacked in the temporal domain. Lastly, [**phase 4**] involves computing travel-time delays of various arrivals between these individual cross-correlated functions and a defined reference cross-correlated function. Afterward, a simple model of uniform relative velocity change [$\delta v/v = -\delta t/t = constant$] [Ratdomopurbo and Poupinet, 1995] is used to estimate seismic velocity changes in the study region. Different options and parameters are available for each of the aforementioned procedures, which require selection and tuning for the study area; these options and parameters will be covered in the following sections.

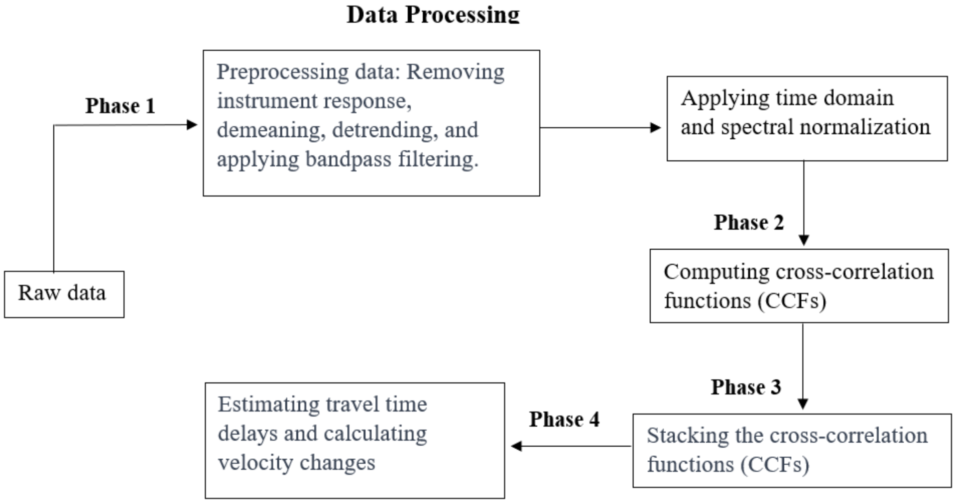

Figure 3.3: The data processing workflow. Phase 1 demonstrates the preprocessing required for single-station data before cross-correlation. Phase 2 involves computing the cross-correlation method and Phase 3 involves stacking the CCFs. Lastly, Phase 4 deals with computing velocity variations.

3.3 PHASE 1: PRE-PROCESSING

Pre-processing the raw data includes several important steps that are required to be completed before cross-correlation. The purpose of the preprocessing step is to enhance ambient noise signals by setting up control parameters to maximize the surface wave energy for estimated Green's functions, and to attenuate transient signals such as earthquakes. The initial step is to prepare the waveform data for each single individual station. The raw data are organized into continuous seismic day-long traces. The data files provide daily traces for every station. Initially, these daily traces are merged in order to address any potential gaps caused by artifacts in the seismic station. The combined data is then split into day-long chunks to ensure continuous segments for each day. These day-long chunks are checked to identify gaps; in order to preserve data continuity, chunks with gaps less than 80% of the day's duration are rejected. Afterward, the accepted day-long chunks are subjected to several preprocessing steps. First, the data is demeaned by removing the mean value to center the waveform around zero. Next, detrending removes any linear trend present in the data to eliminate long-term variations. A 20-second taper is then applied to each day-long waveform to ensure smooth transitions at the segment boundaries [see Appendix A.1]. Following these initial preprocessing steps, this waveform is then subjected to a band-pass filter to remove frequency content over 12 Hz and below 0.01 Hz [see Appendix A.1]. This filtering step focuses the analysis on seismic signals within the desired frequency band. The next critical step involves removing the instrument response and data is downsampled from its original sampling rate of 100 Hz to 25 Hz using a Lanczos resampling method [see Appendix A.1]. Normalization is then applied to the data in both the time-domain and frequency domain in order to standardize the spectral and amplitude characteristics throughout various datasets.

In this study, I chose to investigate the vertical component of the cross-correlation function. There are several parameters that have a significantly non-linear impact on instrument response and normalization. The parameters used for the pre-processing steps were tested and chosen carefully since they greatly rely on the waveform and the desired investigation.

- **INSTRUMENT RESPONSE**

  Correcting instrument response is essential to processing seismic data to ensure the ground motion, earthquakes, and other seismic events captured by seismological sensors are accurately represented. That being said, these instruments by nature incorporate a response function that needs to be corrected, before the raw data can be interpreted accurately. The first phase of data processing is to prepare the waveform data from each station individually. The purpose of this phase is to retrieve the accurate broadband frequency by removing instrument response. In general, the average broadband instrument's response range is between 0.01 and 100 Hz, and for a short-period instrument, it is between 1 and 100 Hz. However, the instrument response frequency varies for a single station [e.g. Figure 3.5 and 3.4]. The response function for most broadband instruments has a flat amplitude in the periods of interest. Consequently, the instrument response only serves as a scaling factor and does not perturb the cross-correlation waveform for broadband stations [Gorbatov et al., 2012]. However, we employed broadband and short-period seismometers in this study. As a result, instrument response was removed during preprocessing to optimize our signal for some stations.

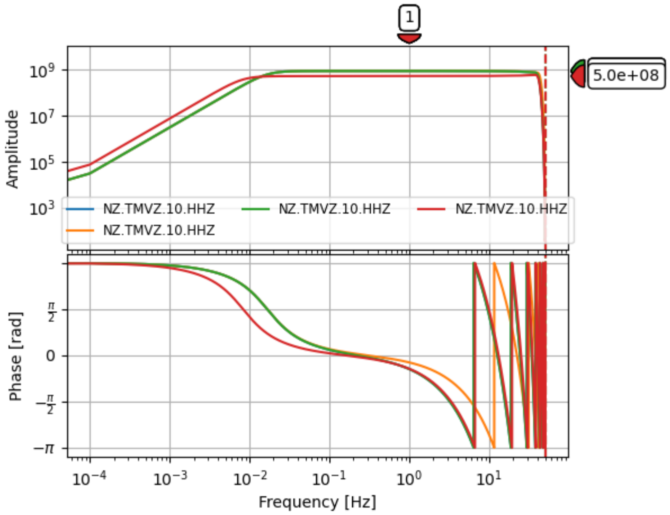

Figure 3.4: Plots showing the amplitude and phase response for a GeoNet broad-band station (TMVZ)

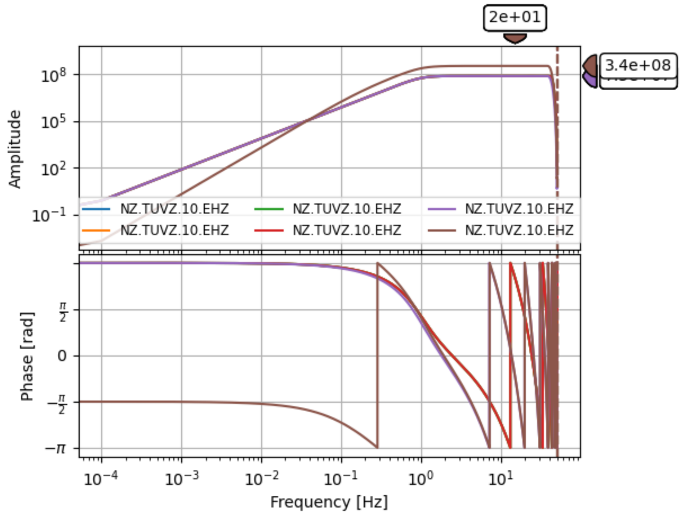

Figure 3.5: Plots showing the amplitude and phase response for a GeoNet short-period station (TUVZ)

A filter was applied before the instrument response was removed. This involved determining the four corner frequencies (f1, f2, f3, f4) of a band-pass filter, which allows frequencies between f2 and f3 while attenuating frequencies outside this range. The pre-filter applied in this study is (0.005, 0.006, 30.0, 35.0) Hz as indicated in Table A.1. This prefiltering step is essential to focus on the seismic signal of interest and ensure accurate removal of the instrument response. Because short-period instruments have a high corner frequency, their cross-correlations are not as stable or dependable for study on ambient noise as broadband correlations.

- **TEMPORAL NORMALIZATION**

  The most important step when working with single-station data preparation is time-domain (or temporal) normalization. Temporal normalization is a technique used to remove or reduce non-uniform signals, high amplitude signals produced near the receiver (e.g., earthquakes, explosions), or non-stationary noise produced in the neighbourhood of the station due to daily human activities. Bensen et al. [2007] outlines the five types of time domain normalization techniques:

  - *Clipped waveform normalization* uses a clipping threshold set as a factor of the RMS amplitude of the signal for that particular day.
  - *Automated event detection and removal* involves setting the waveform's next 30 minutes to zero if its amplitude rises over a certain threshold. The arbitrary nature of this threshold makes it challenging to choose because amplitudes vary throughout stations.
  - *Absolute-mean normalization* is a method that calculates the running average of the waveform's absolute value across a fixed-length time frame and weights the waveform at the window's centre by the inverse of this average.
  - *Water-level normalization* involves down-weighting any amplitude that exceeds a certain multiple of the daily RMS amplitude.

MSNoise can utilize RMS (clipped waveform) clipping and one-bit normalization as shown in Figure 3.6. The method I employed in this study, one-bit normalization is widely utilized in both passive and active seismic studies. It replaces all positive amplitudes with a +1 and all negative amplitudes with a −1, retaining just the sign of the raw signal, which was chosen as it increases the signal-to-noise ratio (SNR).

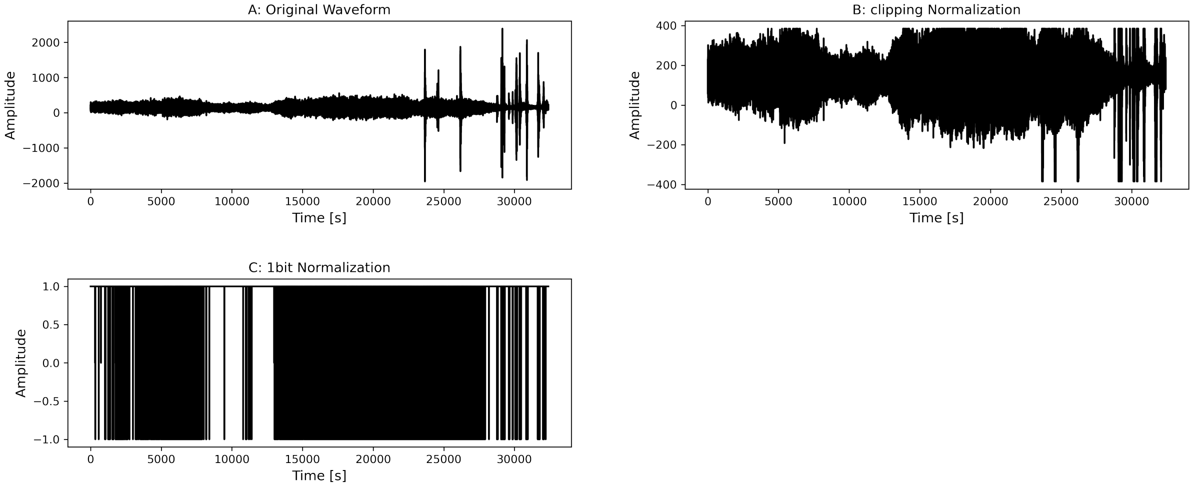

Figure 3.6: Waveforms showing examples of the two time-domain normalization techniques have been tested. (a) Raw data with about ∼ 8 h of windowed data recorded at TUVZ station. (b) Clipped waveform, in which the signal's RMS amplitude for the specified day equals the clipping threshold. (c) A one-bit normalized waveform, in which the signal is set to ± 1 depending on the original waveform's sign.

- **SPECTRAL NORMALIZATION OR WHITENING**

The ambient noise spectrum is not flat [see Figure 3.7A], it is therefore necessary to broaden the bandwidth of the estimated Green's function and to reduce the impact of band-limited spatially localized sources such as the 26s microseism [Bensen et al., 2007]. Frequency domain normalization through spectral whitening acts to balance the amplitude of the data at different frequencies [Pham and Tkalčić, 2017] - shown in Figure 3.7, as not all instruments record frequencies at the same level. One-bit normalization is used to clip the traces in MSNoise, and the signal's amplitude is then whitened in the frequency domain. The goal is to represent broadband Green's function estimations more accurately in the stacked cross-correlation functions (CCFs) that are ultimately generated. In this study, the phase weighted stacking method (PWS) [Schimmel and Paulssen, 1997] was used. Given several N individual one-sided cross-correlograms $s_n(t)$, their analytical signals are defined as

$$S_n(t) = s_n(t) + iH_n(t) = A_n e^{i\phi_n(t)} \tag{3.1}$$

Where $H_n(t)$ is the Hilbert transform of the original trace $s_n(t)$, and A_n, $phi_n(t)$ are the amplitude and phase components, respectively.

The analytical phase average amplitude, which is a measure of the coherence among all signals in the stack, is used to weight their linear stack

$$g(t) = \frac{1}{N}\sum_{n=1}^{N} s_n(t) \left| \frac{1}{N}\sum_{n=1}^{N} e^{i\phi_n(t)} \right|^{\eta} \tag{3.2}$$

Where $\eta \geq 0$ is the PWS order and $g(t)$ is the phase-weighted stack. The order of η controls the contribution of the overall coherency measure in the final stack. If $\eta = 0$, PWS becomes a linear stack while η is large, the coherency measure dominates the stack and makes it severely distorted. We used linear stacking ($\eta = 0$) which gives the best results [see Table A.1].

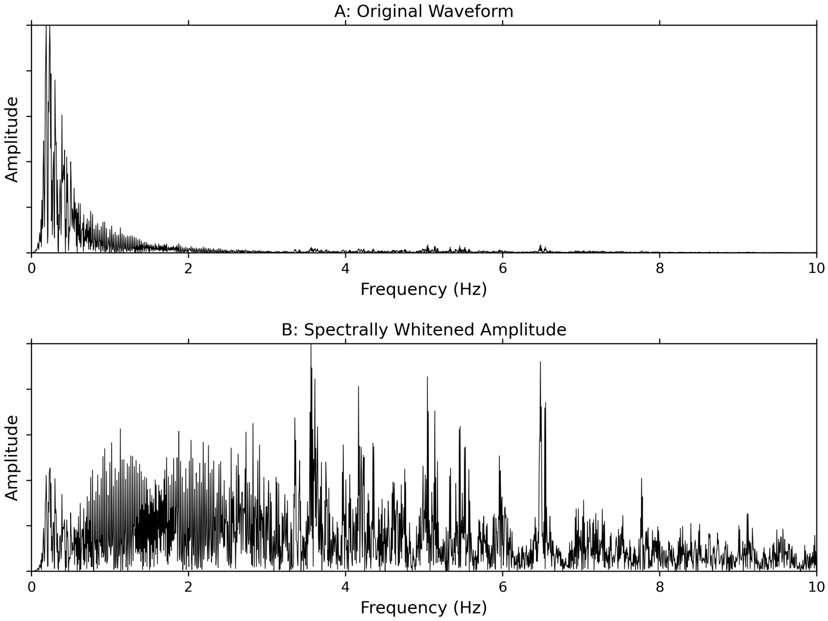

Figure 3.7: (A) Raw data recorded at TUVZ station and (B) spectrally whitened amplitude spectra for 1 sample per second vertical component data at station TUVZ for March 10, 2022. A 20–100 s bandpass filter is primarily responsible for the taper seen at both ends of the spectrum.

3.4 PHASE 2: COMPUTING CROSS-CORRELATION FUNCTION (CCF)

After processing the individual stations, the next stage is to compute the cross-correlations, which produce daily cross-correlations. Cross-correlations were initially calculated between every possible pair of stations, although there is a possibility that certain interstation distances are either short or too long to obtain accurate data. With N being the total number of stations, this results in a total of M potential station pairings.

$$M = N(N-1)/2 \tag{3.3}$$

Fully diffuse wave fields are made up of waves with random amplitudes in all directions [Snieder, 2004]. The cross-correlation of a pair of these wave fields indicates a complete

Green's function between the pair of receivers [Snieder, 2004]. This indicates that by calculating the cross-correlations between the two receivers, information on all potential paths—such as all possible reflections, scatterings, and propagation modes—can be retrieved from them [Gouédard et al., 2008].

Cross-correlation is computed by comparing the similarity of the data from two distant seismic stations — where the trace in one station is shifted relative to the other in time. The cross-correlation that results is saved with both the positive and negative lag parts, which are sometimes referred to as causal and acausal signals, respectively. These parts represent waves that move in opposing directions between the two station pairs and are identical if the noise sources are evenly distributed in the azimuth. The signals observed in the cross-correlation function will only come from sources close to the line joining two stations [Snieder, 2004]. Sources on opposing sides of the line will, in the cross-correlation function, contribute to the signal at positive lag (causal) and negative lag (acausal), respectively.

The cross-correlation is computed in the frequency domain using the two-time series, x(t) and y(t), which are transformed into Fourier transforms X(f) and Y(f). The correlation operation is defined as

$$C(f) = X^*(f) \times Y(f) \tag{3.4}$$

where $X^*(f)$ represents the complex conjugate of $X(f)$. The cross-correlation function $c(t)$ is the inverse Fourier transform of $C(f)$.

Then, a stacking process was conducted to improve the coherence of the Green's function and to increase the signal-to-noise ratio (SNR). MSNoise offers two distinct stacking methods: phase-weighted stack (PWS) and linear mean stacking. The PWS is a nonlinear stacking technique that is computed to enhance coherent signals between instantaneous phases of all windows [Paulssen et al., 1993]. On the other hand, a linear stack results if the PWS order is zero. A simple mean CCF of all windows is saved as the daily CCF if the stacking technique is linear. On the other hand, if the stack method is PWS then all PWS is calculated and stored as a daily CCF [Lecocq et al., 2014].

3.5 PHASE 3: MOVING AND REFERENCE STACKS

The main purpose of stacking is to enhance coherence, improve the signal-to-noise ratio, cancel out information that comes in perpendicular to the stations, and amplify the information that comes basically from directions near 0 or 180 degrees. Generally speaking, stacking across longer time series increases the SNR ratio [Bensen et al., 2007].

In the dv/v equation, the reference stack serves as the denominator. Not only will a moving stack that is too small generate noise, but an insufficiently small reference stack will not give a suitable 'average' velocity. However, very large stacks will also combine changes across short time intervals, which will reduce the signal of the velocity change. The goal is then to select a stack size that is both large enough to yield accurate velocity measurements and small enough to yield useful temporal information. The reference stack and moving stack (current function) are defined as the number of summed cross-correlations (cc's); which are N_{ref} and N_{mov}, respectively. In this study, cc's are calculated daily.

The moving stack CC_{mov} involves summing the daily cross-correlations of specific period of time together, such as 2, 5, and 10 days, while the reference stack CC_{ref} may be created by summing the cross-correlations of a station pair over a reference study period. The only requirement is that the reference stack should be longer than the moving-window stack, $N_{ref} \gg N_{mov}$ to guarantee the reference stack is reflective of a background value, while the moving stack contains information on the actual state of the crust [Clarke et al., 2011]. More days stacked together generally result in better coherency; but, small velocity changes, particularly those that happen over a short period, might become more challenging to recover from as day stack sizes increase. There is an immediate decrease in resolution when a too long moving-window stack is taken [Lecocq et al., 2014].

The reference function (REF) can be specified by an absolute or relative data span. For instance, a relative range could be the last 200 days, while the period from 1 January to 31 December 2022 could be considered an absolute range [Lecocq et al., 2014]. It is good practice to test many moving-window stacks, for example, 2, 5, 10, and 30 days. In this study, various moving stack choices are tested and the reference stack is set as the entire duration (1 January to 31 December 2022).

3.6 PHASE 4: VELOCITY VARIATIONS CALCULATIONS

There are two techniques for estimating time delays in MSNoise: moving-window cross spectrum (MWCS) and stretching method. MSNoise relies on moving-window cross spectrum technique, which operates in the frequency domain to estimate time delay. The technology was first introduced by Poupinet et al. [1984] for the recovery of relative velocity variations between earthquake doublets, the MWCS methodology was developed for noise analysis by Clarke et al. [2011]. The current CC_{mov} is compared with the reference CC_{ref}, and both time series are sliced in several overlapping windows. A cosine taper of 1% is applied to both ends of each slice for adjustment before it is Fourier transformed to the frequency domain [Lecocq et al., 2014, Poupinet et al., 1984]. The cross spectrum $X(\nu)$ is defined as:

$$X(\nu) = F_{ref}(\nu) \times F^{*}_{mov}(\nu) \tag{3.5}$$

The cross coherence between energy densities in the frequency domain:

$$C(\nu) = \frac{|\overline{X(\nu)}|}{\sqrt{|\overline{F_{ref}(\nu)}|^2 |\overline{F_{mov}(\nu)}|^2}} \tag{3.6}$$

where the overline indicates the smoothing of energy spectra F_{ref}, F_{mov}, and the spectrum of X. The time delay between the two cross correlations is found in the unwrapped phase, $\phi(\nu)$, of the cross spectrum and is linearly proportional to frequency:

$$\phi_j = m\nu_j, \tag{3.7}$$

$$m = 2\pi\delta t. \tag{3.8}$$

where δt is the time delay and the phase ϕ_j is expressed in radians. Within the frequency range of interest, the time shift for every window separating two signals is the slope m of a weighted linear regression of the sample data [Lecocq et al., 2014].

The delay time can be estimated by comparing the lag time between the reference stack CC_{ref} and the moving window stack CC_{mov}. Relative velocity variations then can be estimated from the linear slope of the time delay against lag time [Lecocq et al., 2014]. It is important to choose the minimum and maximum lag times for the time shift calculations that are used to estimate relative velocity variations and the slope of the delay times. The maximum lag time is defined by setting a width, in seconds, for the window containing delay times. It is noteworthy that the reliability of the results is increased by cross-correlating over a large range of station pairs, which also increases the stability of the measured velocity changes.

3.7 PARAMETER VALIDATION

The cross-correlation functions of the ambient noise approach are greatly influenced by several parameter choices. To increase the reliability of ambient noise measurements, a variety of processing parameters have been investigated. The main objective of this section is to investigate and justify the many processing choices that are offered to guarantee the highest quality of measured velocity changes.

- **SIGNAL-TO-NOISE RATIO COMPUTATION**

  The signal-to-noise ratio (SNR) measures how strong a signal is compared to background noise present in the same data. Measuring the signal-to-noise ratio (SNR) of a stacked set of cross-correlation functions (cc) is important to determine which stacks can yield reliable delay-time measurements and which cannot [Clarke et al., 2011]. Prior to calculating the lag-time dependent SNR, several parameters were tested using a method first introduced by Larose et al. [2007] and later by Yates [2018].

  The SNR of a cross-correlation function can be obtained by:

  $$SNR(N,t) = \frac{s(N,t)}{\sigma(N,t)} \tag{3.9}$$

  where N is the number of stacked individual days, $s(N,t)$ is the signal level and $\sigma(N,t)$ is the noise level. One may estimate the noise level $\sigma(N,t)$ by calculating the variation between each constituent cross-correlation function (CCF) at every lag time (t);

$$\sigma(N,t) = \sqrt{\frac{< cc(t)^2 > - < cc(t) >^2}{N-1}} \tag{3.10}$$

Before computing the SNR, The signal level $s(N,t)$ and the noise level $\sigma(N,t)$ are both smoothed using a 30-second sliding Hanning window. The signal level $s(N,t)$, in the stacked cross-correlation, is calculated by taking the Hilbert envelope:

$$s(N,t) = |< cc(t) > + iH(< cc(t) >)| \tag{3.11}$$

where $< . >$ denotes the average of N single-day cross-correlation functions $(cc(t))$ and $H(.)$ the Hilbert transform.

- **RELATIONSHIP BETWEEN SNR AND COHERENCE**

Signal quality control is largely dependent on coherence and SNR to compute the velocity changes. Coherence is a measure of how similar the current and reference stacks are to one another within the moving-window stack. Both Coherence and SNR depend on time lags, and plotting coherence against SNR can aid in determining the appropriate coherence threshold to produce high-quality data for a particular station pair by excluding any results that fall below a defined threshold [Yates, 2018], and showing the level of coherence at which the SNR will drop. When MWCS computations are performed, MSNoise produces coherence values, which quantify how similar the current stack is to the reference stack within the moving window. The entire year (2022) of data from all stations was used to evaluate eight filters with different frequency ranges [see Figure 3.8]. As can be seen, every filter has a distinct SNR from the others; selecting the filter that has the greatest SNR produces more trustworthy results. Among the other filters in use, filters 6 and 8, at 0.03–0.35 Hz and 0.05–0.4 Hz respectively, show the highest SNR.

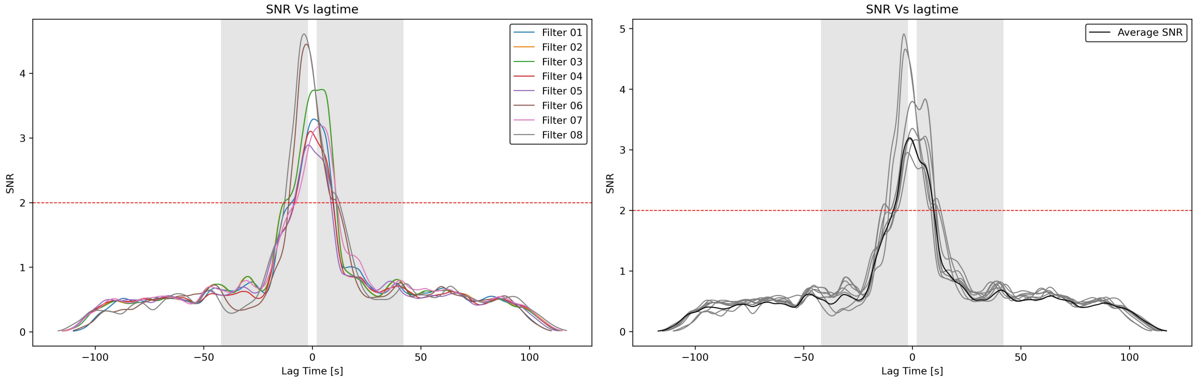

(a) SNR for all filters. In contrast to the other filters, filters eight and six have a high SNR.

(b) the SNR average in black while all filters adopted here are depicted in grey colour.

Figure 3.8: The effect of changes in the filters used [see Table 3.1] for 45-day stacked cross-correlation functions on SNR during a 12-month period at the COVZ-FWVZ station. The gray box shows where direct energy arrivals and exhibits a high SNR for it.

In this study, the maximum interstation distance is 26 km. Assuming surface waves travel at velocities between 2 and 4 km/s, the travel time range is approximately between 6.5 seconds and 13 seconds. The lag time is discussed in Section 3.7. Figure 3.8 serves as an example to show that the direct arrivals come from around 6.5 s and 13 s and exhibit a high SNR above 2 inside the gray-shaded box.

Coherency values with a 45-day stack size were calculated for the NZ.COVZ.10-NZ.FWVZ.10 pair. Figure 3.9 illustrates this in relation to lag time. When the direct arrivals show up in the waveforms, the coherency values are maximum against lagtime. A filter should exhibit strong coherence values during the whole lagtime period ±120 seconds, not only when the direct arrivals come, in order to be selected as a good filter among the ones displayed in the figure. Filters 8 and 6, which are 0.05 - 0.4 Hz and 0.03 - 0.35 Hz respectively, are the best results since they exhibit a high correlation value throughout the period, as can be seen here.

It is important to note that filters 8 and 6 performed the best according to the figures [see Figures 3.9, 3.8], which are based on the two tests mentioned above. The greatest SNR and coherence are shown by both filters (filters 8 and 6). More broadly, strong coherence values during the direct arrivals and a high signal-to-noise ratio (SNR) are indicative of the high consistency of the CCF produced during the tremor, which gives us accurate results.

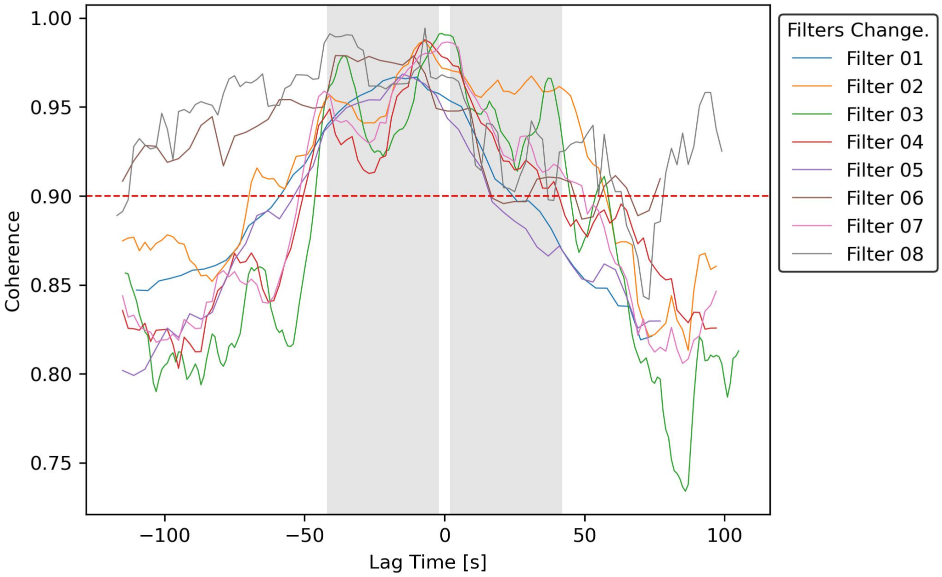

Figure 3.9: Coherence of filters tested for the one-year 2022 dataset for NZ.COVZ.10-NZ.FWVZ.10 using a stack size of 35 days. These are the filters that are displayed in Table 3.1. The filter eight and six has the highest coherency.

- **TEMPORAL STACKING - MOVING WINDOW STACKSIZE**

Stacking cross-correlation functions is mostly used to increase temporal stability by improving the signal-to-noise ratio. Coherent energy is expected to combine constructively, while incoherent energy is expected to combine destructively. Figure 3.10 illustrates 1-day and 30-day stacks over a 12-month period. It should be noted that an N-day stack in MSNoise denotes the cross-correlation function for a specific day stacked with the $N-1$ preceding days. Using 30-day stacks clearly improves temporal stability [Figure 3.10b], whereas 1-day stacks make it difficult to notice coherent arrivals at longer lag periods [Figure 3.10a]. However, the capacity to identify velocity variations and the temporal resolution of the data are diminished with more stacking. Selecting a stack size that is both large enough to yield accurate velocity measurements and small enough to yield useful temporal information is the next step. Cross-correlation functions that are separately compared with the reference stack are referred to as current stacks. The reference stack, which is a cross-correlation reflecting the background state, is made up of a large number of stacked days so that $N_{ref} \gg N_{mov}$. The basis of measurement for velocity changes is the difference between the current stacks and the reference stack. As a result, choosing a current stack that incorporates all accessible data deserves careful thought.

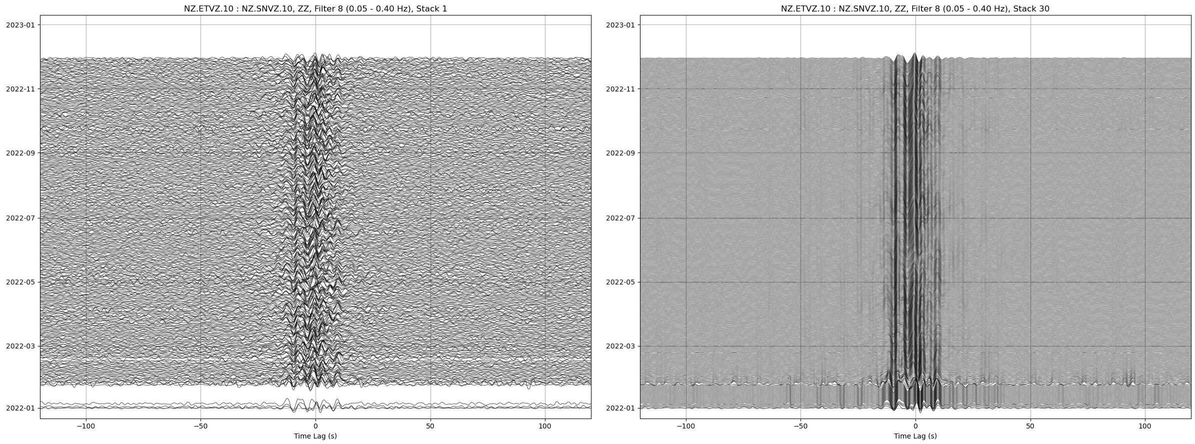

(a) 1-day stacks

(b) 30-day stacks

Figure 3.10: Comparison of 30-day stacked and 1-day stacked cross-correlation functions over a 12-month period using a filter (0.05 -0.40) Hz at the ETVZ-SNVZ station.

Figure 3.11 illustrates how coherence is affected by the number of days in the moving stack. It is important to note that, as shown, the coherence is impacted by the filter that is applied as well. When the filter was adjusted from 0.05–0.4 Hz to 0.1–0.9 Hz, the correlation coefficient values very slightly dropped [see Figures 3.11a and 3.11b for comparison]. Coherency improves as more days are stacked together; but, as the stack sizes rise, it may become harder to identify small velocity changes.

As a result, selecting the ideal moving stack window that offers precise data and strong coherence requires further consideration [see Chapter 4].

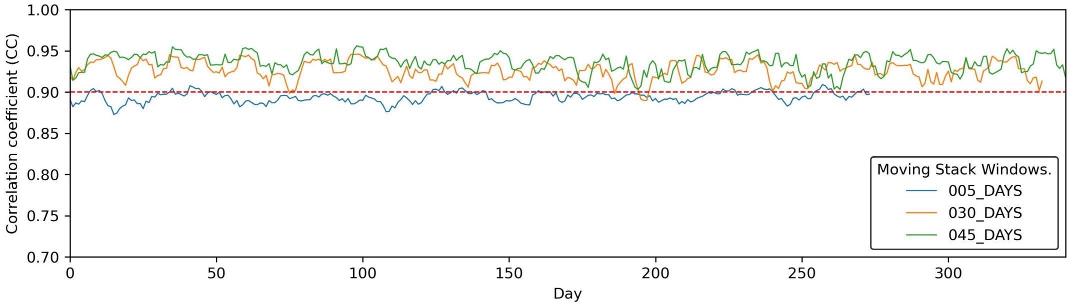

(a) A 0.05–0.4 Hz filter was used to generate this.

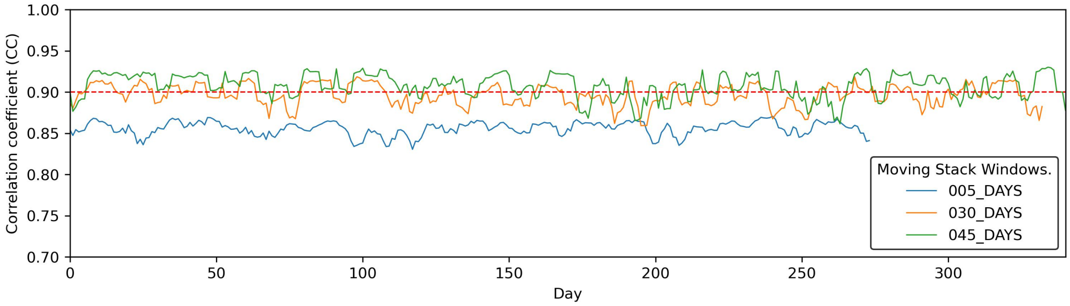

(b) A 0.1–0.9 Hz filter was used to generate this.

Figure 3.11: Average correlation coefficient (CC) for station-pair NZ.COVZ.10–NZ.FWVZ.10 data during a one-year period in 2022 for stack window sizes of 5, 30, and 45 days

- **LAG TIME**

It is important to choose the minimum lag time for the time shift calculations. Most studies conducted in volcanic events used the late arrivals of the CCF because scattered waves traveling along longer distances collect larger temporal delays [Lecocq et al., 2014]. To make sure we were measuring the velocity change from the coda of the cross-correlation functions, we had to specify a minimum time lag for the velocity computations. Both inter-station distance and anticipated wave velocities were considered to set this minimum lag time as a threshold parameter. A single minimum time lag is inappropriate for several station pairs with varying interstation distances because direct arrives later for longer paths. As a result, the inter-station distance and a minimum velocity parameter are used to dynamically define the minimum lag [see Appendix A.1]. We selected nearby stations in our Ruapehu study region [Figure 3.1], totaling 15 stations with varying distance separation [Figure 3.12]. The time delay for every station pair is shown in Figure 3.12, demonstrating the coherent nature of the signal. Based on Mestel's unpublished velocity model, a minimum velocity of 2 km/s was selected [Mestel, 2023, Schuler, 2023].

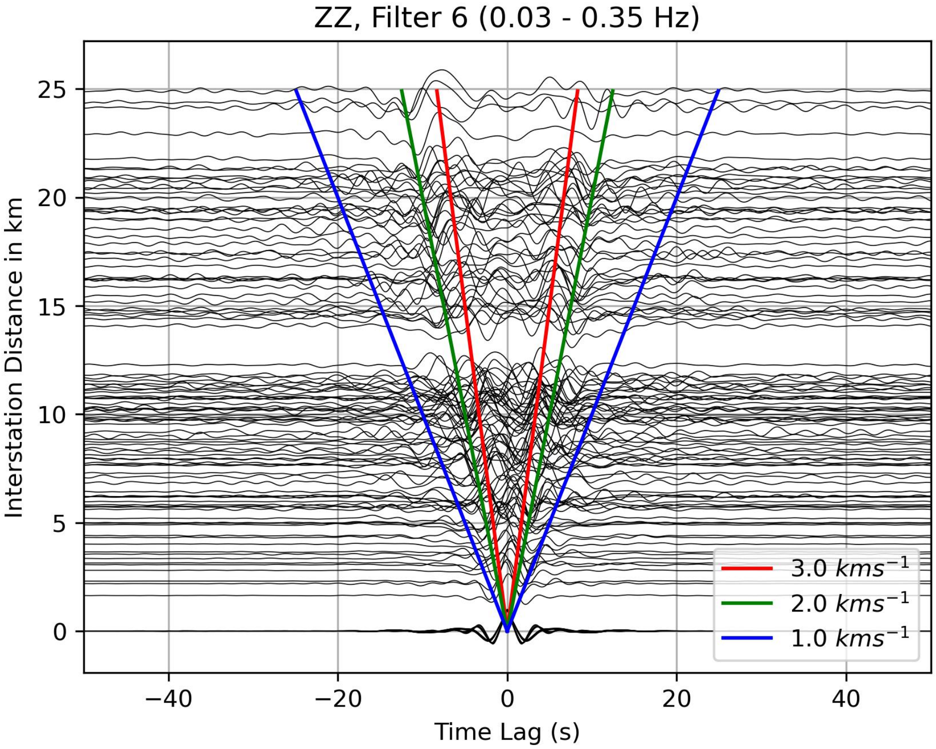

Figure 3.12: The distance against lag time, illustrating the various arrivals predicted at various velocities.

It was also necessary to choose the width of the time lag window, where the width is double the complete cycles of the lowest frequency. Given our lowest frequency of 0.04 Hz [see Table 3.1], the width of the time lag nearly equals 50 seconds. We are satisfied with 40 seconds lag time width as it captures the information from that frequency and within the maximum lag time range of 120 seconds for our cross-correlation function [see Appendix A.1]. Both the causal and acausal components are employed in $\delta t/t$ computations and maximum error and maximum δt were applied in MSNoise. The default value of 0.1 was maintained for the maximum error and the maximum dt is 0.5 s [see Appendix A.1]. Figure 3.13 shows the relationship between coherence and lag time, and lag time against the maximum and the minimum dt for the station pair NZ.NGV.10 and NZ.TRVZ.10 [Figure 3.1 for locations]. The CCFs coherency is excellent in all stations and extremely consistent. Offering an effective way to guarantee high-quality results, the coherence threshold was taken at 0.9 [see Appendix A.1].

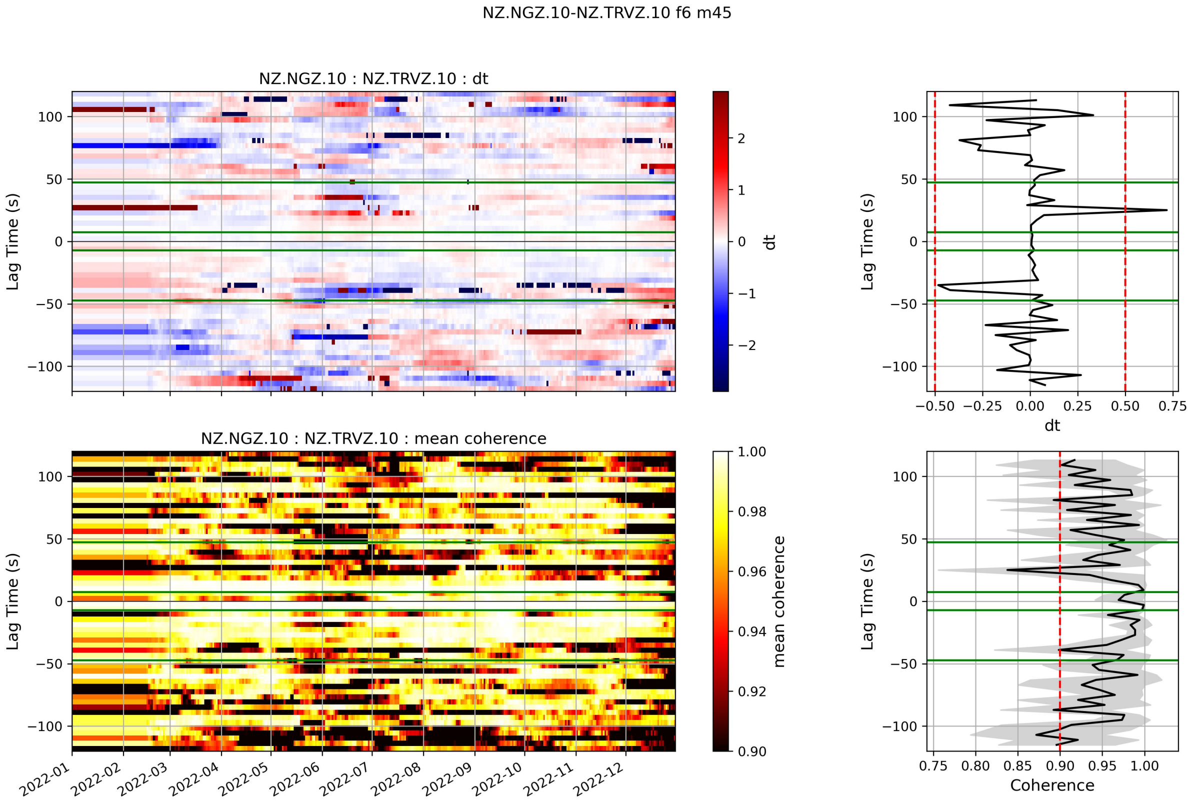

Figure 3.13: The plot shows coherence and dt against lag time

- **FILTER FREQUENCY TEST**

Filters require special attention since MSNoise has several parameters that impact each other nonlinearly. Pre-processing, whitening, and a MWCS filter are applied by MSNoise that can narrow down frequency bands gradually. As indicated in Table A.1, the pre-processing bandpass filter was determined to be 0.01 up to 12 Hz to prevent going over the Nyquist frequency and resulting in aliasing issues. The whiten and MWCS filters were then manually tested and adjusted based on which filter yielded the highest SNR value [see Table 3.1]. Each filter has a window length (Wlen) and step that affects the trade-off between frequency resolution and temporal resolution. The Window Length (Wlen) defines the size of the traces that are used in the MSWC. Better frequency resolution is achieved with a wider window length, but temporal resolution is poorer. The step also referred to as "overlap," controls how much the window moves forward in time between subsequent traces. Filters were obtained from a mix of Schuler [2023], Kortink [2020], and Yates [2018] to assess a varied range of filters that were effectively employed in similar investigations carried out in New Zealand. While several of the examined filters had poor SNR, many of them had acceptable SNR. The best-performing filters were those with narrower frequency widths, between 0.01 and 0.5 Hz, whereas the worst-performing filters had higher frequencies >1 Hz. Using the entire time (one year) in which the low frequency of less than 2 Hz predominates and the high frequency dominates the unrest period, the low-frequency filters yield a cross-correlation function (CCF) that is more consistent than the high-frequency filters. In this study, filter 6—which ranges from 0.04 to 0.34—was used. Several filters are contained under the MSNoise parameter in Table 3.1; the whitening low and high-frequency parameters are manually changed, and the MWCS window length (Wlen) and step are included.

Ref	**Low (Hz)**	**MWCS Low (Hz)**	**MWCS High (Hz)**	**High (Hz)**	**MWCS Wlen (s)**	**MWCS Step (s)**
1	0.1	0.1	1.0	1.0	20.0	4.0
2	0.1	0.15	0.85	0.9	10.0	2.0
3	0.1	0.15	0.4	0.65	12.0	3.0
4	0.1	0.1	0.9	1.1	10.0	2.0
5	0.1	0.15	1.15	1.2	10.0	4.0
6	**0.03**	**0.04**	**0.34**	**0.35**	**20.0**	**4.0**
7	0.12	0.14	0.96	0.98	10.0	2.0
8	0.05	0.06	0.4	0.4	4.0	2.0

Table 3.1: Station pair dataset test filters table

CHAPTER 4

RESULTS

Velocity change findings obtained after the ambient noise processing steps are shown in this chapter. Section 4.1 contains the details of the seismic stations. In Section 4.2, we go over the stations' signal quality and stability in more detail. Lastly, Section 4.3 displays the results of a year test of various moving windows.

4.1 SEISMIC STATION DETAILS

Eight broadband stations and seven short-period sensors spread around Ruapehu were used between January and December of 2022 to create the dataset used in this thesis. In this work, the vertical component was employed, and the lowest distance separation between stations is 2 km, while the maximum interstation distance is 26 km. For the vertical components, data has been acquired at a 100 Hz sample frequency. The WHVZ station had a 5-month data gap, while the WNVZ station did not have any data available during the study period. Therefore, these stations were excluded from this study.

Longitude	Latitude	Station code	Channel	Sensor Type
175.542	-39.200	COVZ	HHZ	Broadband seismometer
175.548	-39.299	TRVZ	HHZ	Broadband seismometer
175.654	-39.268	TUVZ	EHZ	Short period seismometer
175.601	-39.176	NGZ	EHZ	Short period seismometer
175.553	-39.255	FWVZ	HHZ	Broadband seismometer
175.562	-39.268	MAVZ	HHZ	Broadband seismometer
175.640	-39.186	SNVZ	EHZ	Short period seismometer
175.611	-39.126	NOVZ	EHZ	Short period seismometer
175.711	-39.136	ETVZ	HHZ	Broadband seismometer

Continued on the next page

Longitude	Latitude	Station code	Channel	Sensor Type
175.704	-39.116	TMVZ	HHZ	Broadband seismometer
175.676	-39.098	NTVZ	HHZ	Broadband seismometer
175.641	-39.094	KRVZ	EHZ	Short period seismometer
175.590	-39.115	WTVZ	EHZ	Short period seismometer
175.589	-39.282	WHVZ	HHZ	Broadband seismometer
175.665	-39.163	OTVZ	HHZ	Broadband seismometer

Table 4.1: Table of Stations Used

4.2 SIGNAL STABILITY AND QUALITY OF THE STATIONS

The data filtering process is one of the most important aspects of controlling the data signal. In order to compute the cross-correlation, the station recordings have been bandpassed between 0.01 and 12.0 Hz [see Table A.1 for all parameter details], and then decimated by a factor of 4. Following that, whitening was used to limit the frequency of the signal; the lower frequency should be > 0.01 and the high frequency < 12 HZ; the signals then need to be filtered once more using the MWCS filter [see Table 3.1]. Given the sampling rate of 25 Hz, a low-pass filter was set at 12 Hz to prevent exceeding the Nyquist frequency and avoid aliasing issues [see Appendix A.1].

Coherent energy is another important factor that was investigated to ensure the data has high quality. if our signal is coherent, it will be visible through the coherent energy recorded travelling across all pairs from different seismic stations. A very high degree of coherence and consistency of the phase relationship was demonstrated across all stacked cross-correlation functions from different seismic stations, which was more than 0.9 as shown in Figure 3.9. The minimum coherence on the delay time measurement was consequently set at 0.9 for high data quality [see Table A.1]; so, moving window cross-spectrum (MWCS) with coherence lower than that will not be included in the weighted linear regression (WLS) calculation. A correlation between the two signals is suggested by this high level of coherence.

Additionally, the SNR is important for determining the coherence threshold at which the coherence drops. Finding a suitable number of days for which the correlation coefficient reaches over 0.90 can be aided by cross-correlating an increasing stack of days with the reference stack. However, there is an immediate decrease in resolution and low capacity to identify velocity variations when using a moving window stack that is too large. Consequently, choosing a stack size that is both large enough to get precise velocity measurements and small enough to produce reliable temporal information that includes all available data is necessary. Many tests were carried out on a range of moving window stacks, ranging from 5 to 50, as indicated by the MSNoise configuration parameter [see Appendix A.1]. In contrast to the 5-day window stack, which showed a coherence of around 0.85, the 45-day window stack indicated a coherence of 0.95 [see Figure 3.11]. Consequently, the coherence increased with the number of stacks. Unless otherwise indicated, a 45-day moving window stack was the default window size used in this study.

4.3 GEONET STATION PAIR VELOCITY CHANGES

In this section, we present the seismic velocity observations for the unrest; in the next chapter, we discuss and interpret the results. Velocity variations and error in velocity changes for each station pair were calculated for the entire study period. The vertical component of station pairs near Ruapehu produced some of the most consistent and high coherence cross-correlation functions during the tremor. The mean velocity changes for all pair stations utilized are shown in Figure 4.1. Following the unrest, there was an estimated 0.1-0.2 % decrease in the relative mean velocity variation. The constant dv/v shown in the beginning in Figure 4.1 is due to the 45-day moving window lag, and because it has been smoothed over a longer moving window time, the result is much more obvious than with smaller moving windows would be.

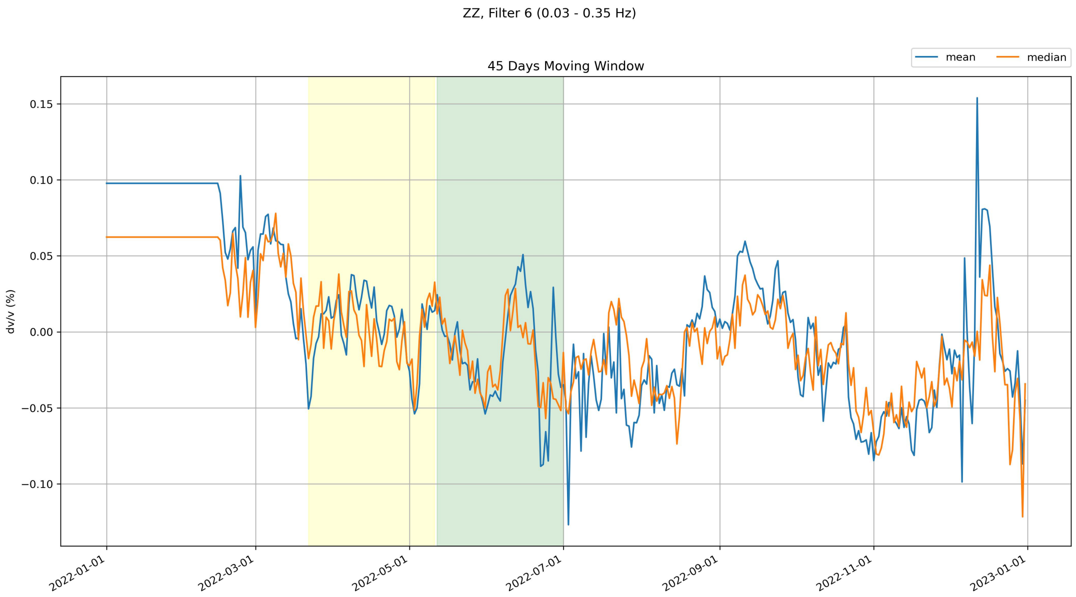

Figure 4.1: Relative Median velocity variations using one year's worth of data for the vertical-vertical component for a 45-day moving window with a one-year reference period. The combined colors indicate the duration of the unrest period which started in early March and lasted until the end of June. The yellow shade represents the period of velocity drop, while the light green shade signifies the subsequent recovery phase following the velocity decrease.

This overall velocity change was calculated for all station pairs in this study [see Figure 3.1]; however, many station paths do not cross Ruapehu edifice. Rather, in order to understand the change in velocity, certain pairings were selected to get more precise results, shown in Figure 4.3. Furthermore, paths along the West-North and East-North of Mount Ruapehu were examined to identify any seismic velocity changes. These pairs of short-period and broadband seismometers were NGZ-TUVZ, OTVZ-TUVZ, SNVZ-TRVZ, FWVZ-TRVZ, NOVZ-TRVZ, and COVZ-TRVZ. These station pairings were chosen to record any velocity variations because their courses crossed Ruapehu edifice.

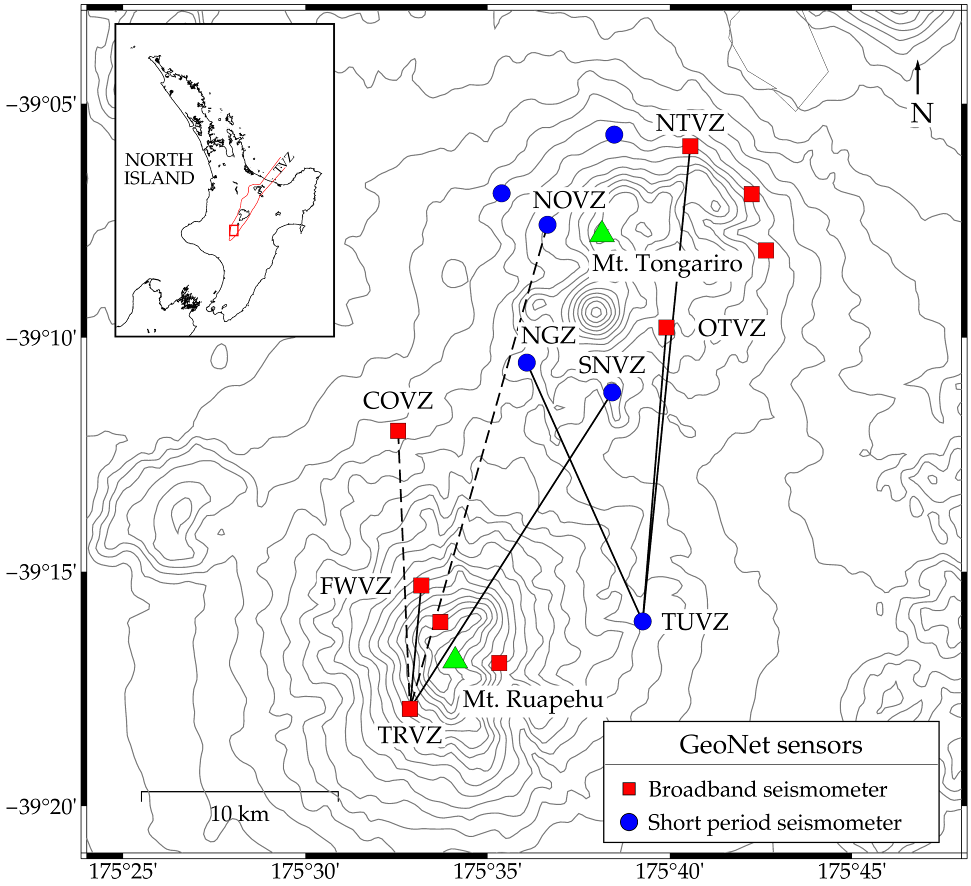

Figure 4.2: Spatial distribution of GeoNet seismic network around Mt. Ruapehu. An inset map shows the location of Mt. Ruapehu at the southern end of the Taupo Volcanic Zone on the North Island of New Zealand. Red squares show broadband seismic stations, whereas blue circles represent short-period seismic stations. The seismic station pairs cited in this study are highlighted. The solid and dashed lines show the WN and EN of Mount Ruapehu, respectively.

Figure 4.3 illustrates station pairs near Mount Ruapehu, including those to the east-north (EN), in a single figure. These station pairs exhibit a consistent reduction in velocity starting nearly four weeks before the onset of unrest. Specifically, a decrease in velocity of approximately 0.5 % is observed for station pairs until May 1, 2022, followed by a subsequent increase. The figure displays several notable features, including a decrease in velocity that occurred approximately two weeks prior to the heightened lake temperature and volcanic activity on March 13 according to GNS bulletin [see Section 5.3], the velocity then recovered to return to its mean after the unrest ended in late June, and a flat line at the beginning due to not having enough data to average the moving window yet. This velocity decrease took place four weeks (approximately on February 22) prior to the change in volcanic alert level (March 22, 2022) and is a feature shared between all station pairs that can be seen in Figure 4.3. Before the onset of unrest on March 22, 2022, the alert level was 1, which escalated to level 2 during the unrest period, and returned to level 1 shortly after the unrest ended in early July. The velocity started to decrease four weeks before the unrest and reached a maximum variation of $\sim 0.5\%$ following the event, peaking in early May. After that, the velocity slowly recovers to the long-term average velocity in the next weeks. These results demonstrate the mechanism responsible for these velocity variation observations is reversible. This mechanism is best displayed in Figure 4.4, showing 45-day moving window used to display the velocity variations for the NGZ-TUVZ station pair, which are situated on the east flank of Ruapehu.

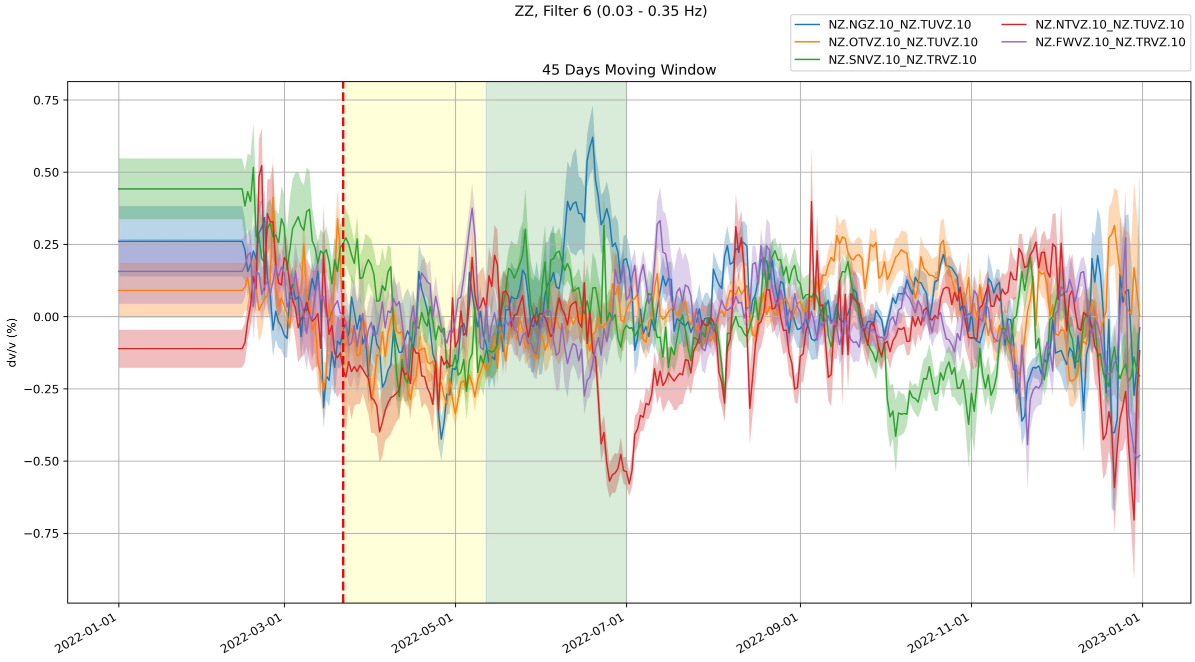

Figure 4.3: Velocity changes for all station pairs calculated for 45-day moving windows using one year of data for the vertical-vertical component. The combined colors indicate the duration of the unrest period which started in early March and lasted until the end of June. The yellow shade represents the period of velocity drop, while the light green shade signifies the subsequent recovery phase following the velocity decrease.

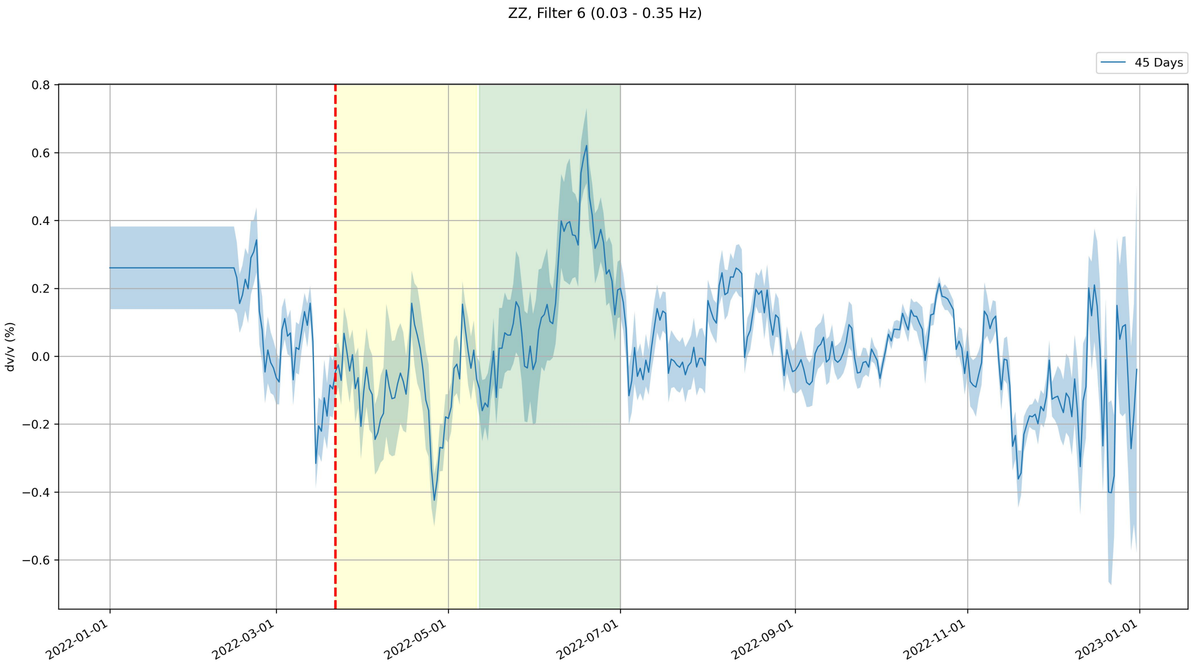

Figure 4.4: Velocity changes for NGZ-TUVZ station pair calculated for 45-day moving windows using one year of data for the vertical-vertical component. The combined colors indicate the duration of the unrest period which started in early March and lasted until the end of June. The yellow shade represents the period of velocity drop, while the light green shade signifies the subsequent recovery phase following the velocity decrease.

This decrease before the unrest is visible in the 35-day, 40-day, 45-day, and 50-day moving window velocity variation plots for the NGZ-TUVZ station pair, shown in Figure 4.5. The usage of various moving stack day windows results in a flat line in the relative velocity change for the beginning of the study period. For instance, there is a 35-day flat line at the start of the 35-day moving window, and a 40-day flat line at the start of the 40-day moving window, along with the same for the remainder. The N-moving window is the average velocity of the previous N days, including the current day. Figure 4.5, shows velocity began to decrease from approximately the same position in late February, and velocity variances were at their mean before the drop began. In this study, a 45-day moving window was used, which results in smoothing of the small daily variations and velocity reduction that occurs two weeks prior to the unrest and shows a gradual decline. A smaller stack size, like five hours, may indicate sub-daily variations and, as a result, the reduction in velocity before unrest would be more reliable, potentially showing a less gradual drop in velocity pre-unrest.

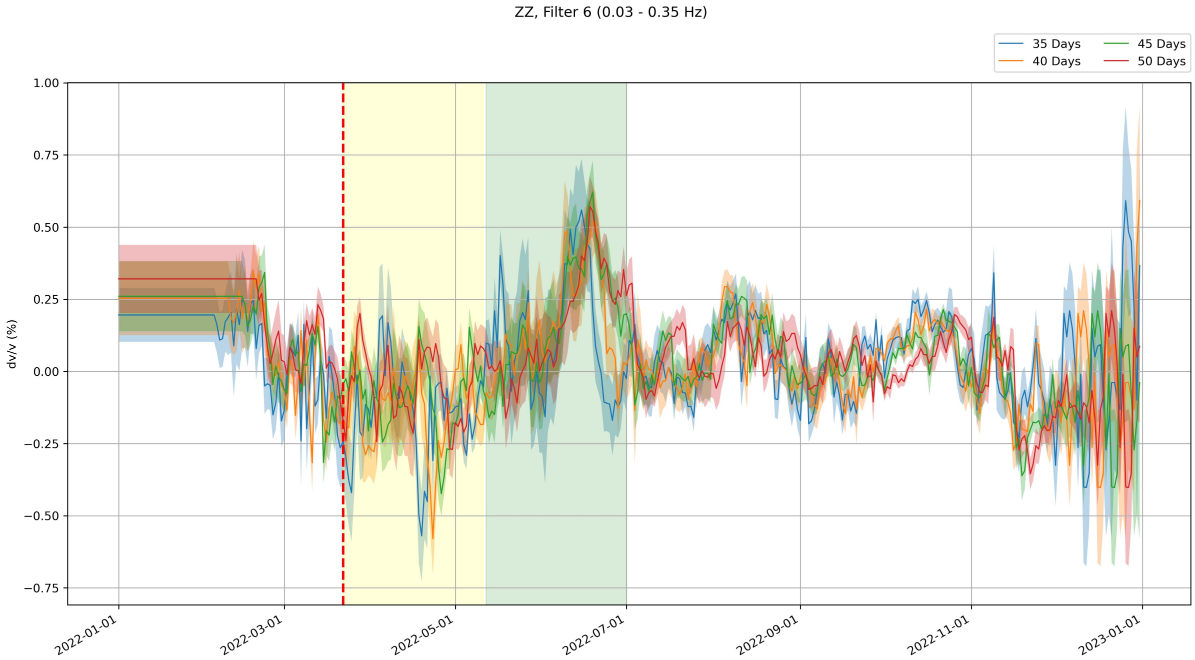

Figure 4.5: Velocity changes for NGZ-TUVZ station pair calculated for 35-day, 40-day, 45-day, and 50-day moving windows using one year of data for the vertical-vertical component. The combined colors indicate the duration of the unrest period which started in early March and lasted until the end of June. The yellow shade represents the period of velocity drop, while the light green shade signifies the subsequent recovery phase following the velocity decrease.

Velocity changes for two station pairs on the west flank of Mount Ruapehu are shown in Figure 4.6. The plotted data reveals that the mean velocity has not changed significantly on the subsurface of the west side. This stability may be explained by the lack of nearby faults the western side of Ruapehu, which are usually linked to notable ground movement. These observations are consistent with Mordret et al. [2010] that observed 0.8% reduction in the east flank of Ruapehu two days prior to the 2006 eruption, which corresponded to an opening crack in that region and caused a localized drop in velocity [Mordret et al., 2010], but little variation in the west flank velocity. The 2022 unrest was characterized by a similar decline in the velocity in the eastern part of Ruapehu, with no appreciable velocity change in the mean velocity in the western part. A detailed analysis of the geological background and past seismic activity would be beneficial for future interpretation in order to ensure complete comprehension of the absence of velocity variations on the west side of Ruapehu.

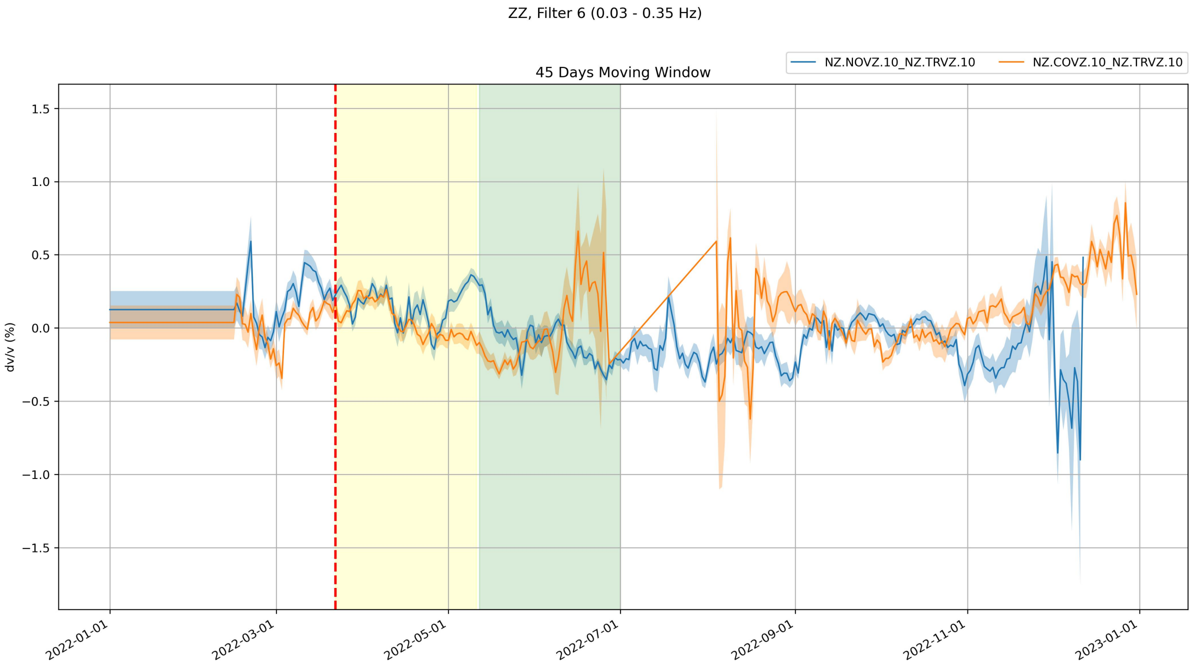

Figure 4.6: Velocity changes calculated for 45-day moving windows using one year of data for the vertical-vertical component of west flank stations. The combined colors indicate the duration of the unrest period which started in early March and lasted until the end of June.

CHAPTER 5

DISCUSSIONS

Recognizing the signs that volcanoes frequently exhibit before the start of eruptions is the first step toward intermediate- or short-term eruption forecasting. Seismicity, ground deformation, gas emissions, and thermal emissions are only a few of the signs of volcanic unrest that have been observed in active volcanoes over the past few decades and occasionally result in eruptions. As magma builds up at depth and subsequently rises towards the surface, these signs can be seen at various phases of pre-eruptive unrest.

In this discussion, we focus on interpreting the recent unrest that occurred in 2022 based on the seismic velocity results, recordings of volcanic tremor and crater lake temperature. First, information on the heating cycle and volcanic tremor that occurred during the unrest in 2022 are summarised in Sections 5.1 and 5.2. These observations are then analyzed in comparison to the seismic velocity results in Section 5.3.

5.1 HEATING OF THE CRATER LAKE AT MOUNT RUAPEHU

The temperature and lake level of Ruapehu Crater Lake during 2022 are displayed in Figure 5.1. This is an attempt to examine the temperature changes that occurred during the unrest episode and understand the relationship between temperature and the unrest event. On March 13, 2022, Te Wai A-moe Crater Lake in Mount Ruapehu began to warm. The temperature increased throughout the following two months, peaking on May 8 at 40.77 ^{o}C [see Figure 5.1]. The increase in temperature might be interpreted by magma intrusion into the hydrothermal system while magma attempts to ascend to the surface, however, there is no evidence to support this theory in the unrest of 2022. Nevertheless, from April 7 to the end of the month, the temperature remained constant at about $\sim$ 37 ^{o}C. This may be attributed to potential influences on the heat such as rainfall, external temperature changes, or hydrothermal systems, which kept the lake's temperature stable for a considerable amount of time.

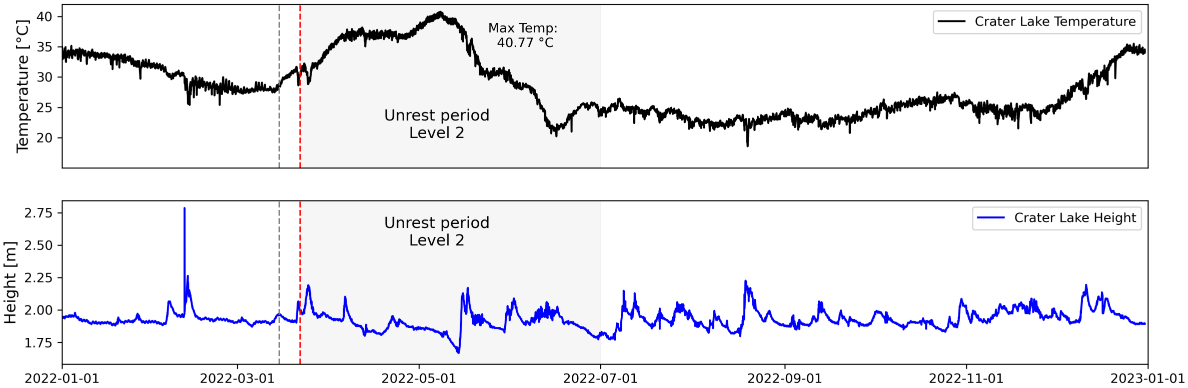

Figure 5.1: This figure presents the changes in Crater Lake's temperature and level during the year 2022. On May 8, 2022, the highest temperature recorded was 40.77 degrees. The gray-colored box indicates the duration of the unrest period, which started in early March and lasted until the end of June. The red and gray lines represent the start of the unrest (March 22, 2022) and the period of heightened lake temperature and increased tremors (March 15, 2022), respectively.

On the other hand, early May saw a sharp dip in temperature to 21 ^{o}C and nearly stable later on at 25 ^{o}C, although it did so at a different rate than it had been rising. This suggests that precipitation during May may have had a significant impact on the rapid drop in the lake's temperature. The volcanic alert level was changed to level one in July since the totality of the evidence pointed to a significantly lower level of volcanic activity and temperature drop to its normal.

It is noteworthy that there exists a correlation between temperature and other environmental parameters and how they affect variations in velocity and surface structure. Furthermore, the specifics of these correlations might differ greatly based on the characteristics, location, and scale of the system under study.

5.2 STRONG TREMOR

For the 2022 period, the mean daily ground velocity is shown in Figure 5.2. As can be seen, the tremors began on March 13, 2022, and became more intense on March 21, surpassing the threshold level, which led to the alert level being raised to level 2. This threshold, known as the Baseline Threshold Level (BTL), is represented by the dashed green line in Figure 5.2 and has a value of 330 RSAM for this seismograph. Early in May, the daily mean ground velocity increased over 2000 nm/s. The unrest period occurred between March and June [see Section 1.3.5], and corresponds to the seismic activity [Figure 5.2]. Furthermore, the lake's temperature exhibited a very similar pattern of behaviour during the unrest.

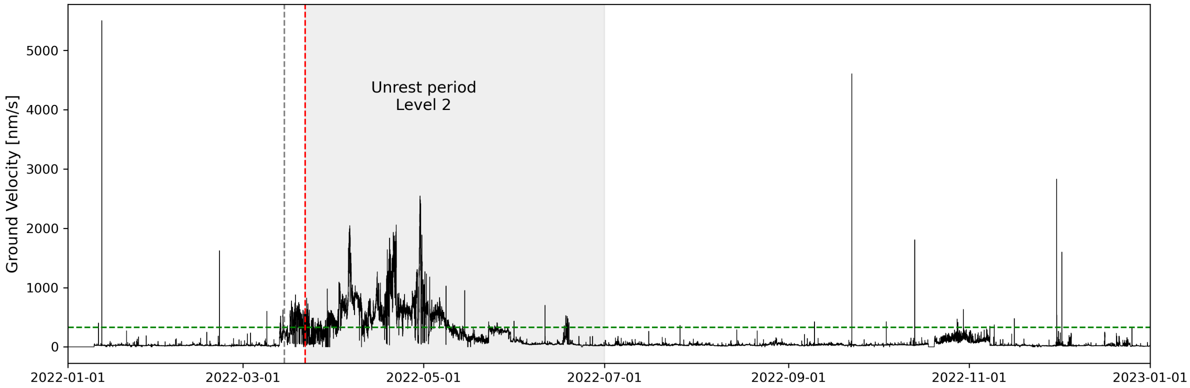

Figure 5.2: Real-time Seismic-Amplitude Measurement (RSAM) for the MAVZ station located on Ruapehu for 2022, averaged daily. The data was filtered between 1.0 - 4.0 Hz before calculating the RSAM. The dashed green line on the graph represents the Tremor Baseline Threshold Level (BTL). The red and gray lines represent the start of the unrest (March 22, 2022) and the period of heightened lake temperature and increased tremors (March 15, 2022), respectively. The RSAM value from this seismograph is 330.

5.3 SEISMIC VELOCITY VARIATIONS AS AN INDICATOR OF UNREST

The unrest period at Ruapehu, as indicated by elevated levels of volcanic tremor and crater lake temperature began on March 13, 2022. In contrast, the velocity variation results indicated a decrease in velocity in late February, 2 weeks before both the tremors and lake temperature increased. This is further evidence for seismic velocity variations as an indicator of unrest at Ruapehu. For example, in 2006, we witnessed an eruption with a 0.8 decrease in seismic velocity two days prior to the eruption [Mordret et al., 2010]. These results suggest seismic velocity variations may be a leading indicator of unrest and eruption at Ruapehu.

On March 13, 2022, Ruapehu's crater lake started to experience a heating cycle accompanied by increasing levels of volcanic tremor. The increase in lake temperature is not an instantaneous event but a process that needs time, days, weeks, or even a month, and it depends on the amount of gases entering the lake and the crater lake geothermal system. Crater Lake temperature is therefore likely to be a lagging indicator of unrest or subsurface changes at Ruapehu. The increased seismic activity noted [refer to Figure 5.3] likely indicates increased magma and/or fluid flow in the volcanic conduit system beneath the surface of Ruapehu and may be a contemporaneous indicator of volcanic unrest at Ruapehu.

The velocity drop was not observed or it is dubious for the station pairs WNVZ, and WHVZ due to their inadequate data set. The data for the station pairings MAVZ–WHVZ and TRVZ–TUVZ likewise indicate a large rise in velocity, which is quite ambiguous. This increase in seismic velocity might be interpreted as resulting from limitations or inconsistencies in data collection and processing and is not indicative of a volcanic process.

This leads us to the reason for the seismic velocity drop. A complete understanding of the seismic velocity changes is outside of the scope of this thesis, however, several possible sources may be identified. Seismic velocity changes may decrease as a result of magma intruding into the subsurface without reaching the surface and magma moving more slowly due to the resistance of the surrounding rocks [Ratdomopurbo and Poupinet, 2000, Sparks, 1997, Obermann et al., 2013b, Annen et al., 2005]. As a result, magma may have been trapped beneath the volcano, which could explain the formation of a low-velocity zone in the East-North of Ruapehu [see Figure 4.3]. Moreover, fluid fluxes like water, gas, or magma can alter the characteristics of the rocks they travel through or produce voids or gas bubbles inside the rocks, which will cause a decrease in velocity during volcanic unrest.

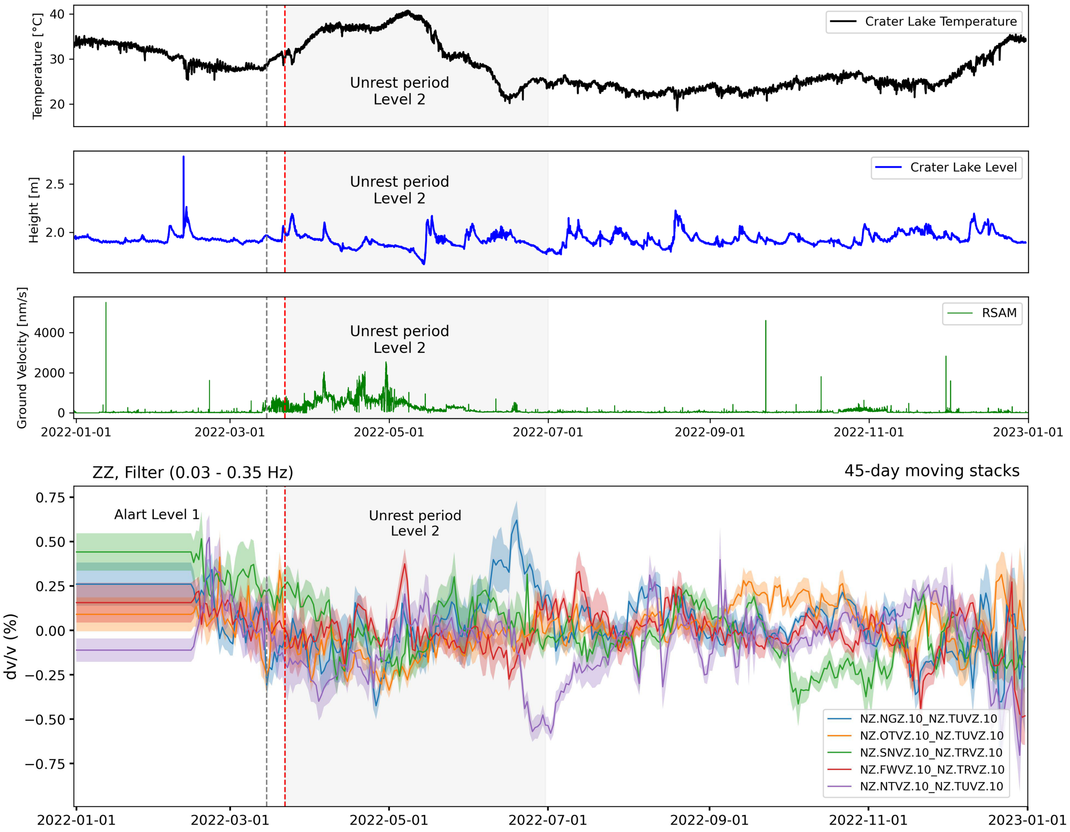

Figure 5.3: This figure displays changes in Crater Lake's temperature and level, RSAM, and relative seismic velocity during the year 2022. The gray-colored box indicates the duration of the unrest period, which started in early March and lasted until the end of June. The red and gray lines represent the start of the unrest (March 22, 2022) and the period of heightened lake temperature and increased tremors (March 15, 2022), respectively.

CHAPTER 6

CONCLUSIONS

In this thesis, seismic velocity variations from ambient noise interferometry for the year 2022, covering the recent unrest at Ruapehu volcano were obtained, utilizing a year's worth of data acquired by GeoNet. Chapter 1 stated four main goals, which were summarised as

- *Identify the seismic velocity and velocity variations at Ruapehu volcano during 2022.*
- *Investigate the correlation between the seismic velocity variations and the unrest.*
- *Identify changes in seismic velocity during the unrest in 2022.*
- *Consider the use of ambient noise for the detection and monitoring of volcanic unrest and activity.*

Analysis was conducted over a one-year period to determine changes that occurred prior to and during the unrest in 2022. The vertical-vertical component of the cross-components showed a drop in seismic velocity prior to the 2022 unrest and the decrease continued during the unrest between March and June. Furthermore, because our filter was used for the entire period (one year), the low frequency of less than 2 Hz predominates. For this reason, high-frequency filters would be more appropriate if the study was focused on the unrest period, which was dominated by the tremors. This chapter includes a summary of the thesis's results [Section 6.1] and suggestions for possible directions for further research [Section 6.2].

6.1 SUMMARY OF FINDINGS

The main conclusions of this thesis are developed in connection to the main objectives in Sections 6.1.1 and 6.1.2. The challenges and the future work research are presented in Section 6.1.3 and 6.2, respectively.

6.1.1 VELOCITY CHANGES AT RUAPEHU VOLCANO DURING 2022

During the 2022 unrest at Ruapehu volcano, between March and June, a variation in seismic velocity was noticed. The studied dataset shows a drop in seismic velocity started late in February 2022 [see Figure 4.3]. This decrease in seismic velocity persisted throughout the unrest and was accompanied by a rise in lake temperature and increased volcanic activity [see Figure 5.1 and 5.2]. Since this drop is a reversible process, the velocity recovery will occur after the decrease and before it returns to its mean velocity, this was observed between early May and June. All of the stations that were utilized had a mean velocity change of around 0.2% [see Figure 4.3]. These stations are dispersed across Tongariro National Park [see Figure 3.1]; however, Ruapehu volcano showed a $\sim 0.5\%$ reduction in seismic velocity across the East-North of Ruapehu [see Figures 4.3, 4.2]. This drop in velocity might be caused by a variety of events, such as fractures opening, fluid fluxes such as water, gas, or magma, magmatic anomalies, magma intruding into the subsurface without reaching the surface, or environmental factors (e.g. rainfall or atmospheric pressure changes). However, there is no conclusive indication of what factor caused this unrest. Given this, further research would help understand the mechanism that results in such a drop in seismic velocity.

An interesting observation was noted about the seismic velocity throughout Ruapehu's West-North, which has not changed [see Figure 4.6], in contrast to the drop across the East-North of Mount Ruapehu. Interestingly the decrease in seismic velocity occurred before the lake's elevated temperature and rise in seismic activity. Thus, seismic velocity variations may be a leading indicator of unrest.

6.1.2 IMPLICATIONS FOR AMBIENT NOISE MONITORING

It may be possible to monitor the unrest of volcanoes in real time using ambient noise. The dataset used in this thesis demonstrates how challenging it would be to understand changes in seismic velocity based on ambient noise prior to the unrest in 2022 if such approaches were not coupled with other methods. However, this method clearly shows the velocity reduction both before and during the unrest event. The findings of this thesis highlight how effective it may be to monitor Ruapehu utilizing ambient seismic noise. The ability to measure relative seismic velocity variations ($\delta v/v$) using ambient noise can support monitoring volcanic activity in real time or short time and work as a supplementary method to other techniques used to monitor the volcanic activity in the region, empowering authorities to promptly warn the public. Therefore, ambient noise may serve as a helpful tool for volcanoes that are close to populations' residence or activity when identifying whether a volcanic system has been disturbed by fluid intrusion or far-off tectonic earthquakes. Monitoring these changes before the unrest in real-time can also help in the early identification of any future intrusive events or changes in Ruapehu's volcanic activity.

6.1.3 CHALLENGES

Given the magnitude of the unrest accompanied by the increased lake temperature and seismic activity over the study period, it is very probable that clear indicators of a change were observed prior to this unrest. Yet, this method is unable to predict if an eruption will occur or if the drop is due to fluid interaction with a conduit or magma intruding into the subsurface. The complexity of the area is a major factor, as is our unawareness of the exact amount of velocity reductions required to induce an eruption, which makes it very difficult to determine whether will we have an eruption or a heightened phase of volcanic activity only.

One of the challenges was the lack of station density around Mt. Ruapehu therefore the GeoNet network has to be improved, and increasing the stations around the volcano in order for temporal seismic velocity changes to become a strong and trustworthy approach. Other methods, including single-station velocity changes [De Plaen et al., 2016], would also be beneficial to have as it functions well in areas with a few seismometers.

6.2 RECOMMENDATIONS FOR FURTHER WORK

The ambient noise made it possible to monitor seismic changes as it is very sensitive to small changes in the subsurface. Despite the restricted station duration operation and quality, the ability to measure these velocity changes was not affected. Here are some suggestions for further research. With these recommendations, we seek to shed light on how ambient noise may be utilized to learn more about Ruapehu region and how these findings might help us understand the bigger picture of the region.

- ***Seismic tomography and magnetic anomaly of the western flank of Mt. Ruapehu:*** The study's result was interesting since we noticed a decrease in seismic velocity in the eastern north region of Mt. Ruapehu but not in its western north region. This raises the question, "What is underneath the western part and the reason behind the velocity drop seen in the Mount Ruapehu EN edifice?". Further investigation looking for anomalies in the region can aid us in comprehending the subsurface beneath Mt Ruapehu. Thus, magmatic anomalies and tomography studies would provide a piece of convincing evidence and support for the findings that the seismic velocity decreases are more visible in the EN than in the WN.

- ***Extend the time frame for seismic data:*** A year's worth of data for 2022 was analyzed in this thesis to look for significant changes in seismic velocity both before and after the unrest event. The seismic velocity in this dataset decreased beginning in late February. Since the moving window size is 45 days in this study, extending the period would enable us to monitor prior to unrest and would provide a more comprehensive view of the velocity change values. For instance, we may begin in October 2021 rather than February 1st, 2022.

- ***Analysing Seasonal Variations:*** This thesis included information on the temperatures and level of Crater Lake in 2022. The rise in the lake's level may have been caused by rainfall or snowmelt. It would be interesting to investigate seasonal variations, such as relationships between rainfall and weather, to determine if they had a significant impact on velocity changes during the unrest in 2022.

REFERENCES

K. Aki. **Space and time spectra of stationary stochastic waves, with special reference to microtremors**. *Bulletin of the Earthquake Research Institute*, 35:415–456, 1957.

K. Aki and V. Ferrazzini. **Seismic monitoring and modeling of an active volcano for prediction**. *Journal of Geophysical Research: Solid Earth*, 105(B7):16617–16640, 2000. doi: 10.1029/2000JB900033.

K. Aki and R. Koyanagi. **Deep volcanic tremor and magma ascent mechanism under Kilauea, Hawaii**. *Journal of Geophysical Research: Solid Earth*, 86(B8): 7095–7109, 1981. doi: 10.1029/JB086iB08p07095.

K. Aki, M. Fehler, and S. Das. **Source mechanism of volcanic tremor: fluid-driven crack models and their application to the 1963 Kilauea eruption**. *Journal of Volcanology and Geothermal Research*, 2(3):259–287, 1977. ISSN 0377-0273. doi: 10.1016/0377-0273(77)90003-8.

B. V. Alloway, B. J. Pillans, L. Carter, T. R. Naish, and J. A. Westgate. **Onshore-offshore correlation of Pleistocene rhyolitic eruptions from New Zealand: implications for TVZ eruptive history and paleoenvironmental construction**. *Quaternary Science Reviews*, 24(14):1601–1622, 2005. doi: 10.1016/j.quascirev.2004.07.026.

H. Anderson and T. Webb. **New Zealand seismicity: Patterns revealed by the upgraded National Seismograph Network**. *New Zealand Journal of Geology and Geophysics*, 37(4):477–493, 1994. doi: 10.1080/00288306.1994.9514633.

H. Anderson, T. Webb, and J. Jackson. **Focal mechanisms of large earthquakes in the South Island of New Zealand: implications for the accommodation of Pacific-Australia plate motion**. *Geophysical Journal International*, 115(3):1032–1054, 12 1993. doi: 10.1111/j.1365-246X.1993.tb01508.x.

T. Anggono, T. Nishimura, H. Sato, H. Ueda, and M. Ukawa. **Spatio-temporal changes in seismic velocity associated with the 2000 activity of Miyakejima Volcano as inferred from cross-correlation analyses of ambient noise**. *Journal of Volcanology and Geothermal Research*, 247-248:93–107, 2012. ISSN 0377-0273. doi: 10.1016/j.jvolgeores.2012.08.001.

C. Annen, J. D. Blundy, and R. S. J. Sparks. **The genesis of intermediate and silicic magmas in deep crustal hot zones**. *Journal of Petrology*, 47(3):505–539, 12 2005. ISSN 0022-3530. doi: 10.1093/petrology/egi084.

H. J. A. Van Avendonk, W. S. Holbrook, D. Okaya, J. K. Austin, F. Davey, and T. Stern. **Continental crust under compression: A seismic refraction study of South Island Geophysical Transect I, South Island, New Zealand**. *Journal of Geophysical Research: Solid Earth*, 109(B6), 2004. doi: 10.1029/2003JB002790.

S. Bannister. **Seismic exploration in geothermal areas-effect of the surface layer**. *Proceedings of the 14th New Zealand geothermal workshop*, pages 231–235, 1992.

S. Bannister, C. J. Bryan, and H. M. Bibby. **Shear wave velocity variation across the Taupō Volcanic Zone, New Zealand, from receiver function inversion**. *Geophysical Journal International*, 159(1):291–310, 10 2004. doi: 10.1111/j.1365-246X.2004.02384.x.

N. L. Bennington, M. Haney, S. De Angelis, C. H. Thurber, and J. Freymueller. **Monitoring changes in seismic velocity related to an ongoing rapid inflation event at Okmok Volcano, Alaska**. *Journal of Geophysical Research: Solid Earth*, 120(8): 5664–5676, 2015. doi: 10.1002/2015JB011939.

G. D. Bensen, M. H. Ritzwoller, M. P. Barmin, A. L. Levshin, F. Lin, M. P. Moschetti, N. M. Shapiro, and Y. Yang. **Processing seismic ambient noise data to obtain reliable broad-band surface wave dispersion measurements**. *Geophysical Journal International*, 169(3):1239–1260, 06 2007. doi: 10.1111/j.1365-246X.2007.03374.x.

G. D. Bensen, M. H. Ritzwoller, and N. M. Shapiro. **Broadband ambient noise surface wave tomography across the United States**. *Journal of Geophysical Research: Solid Earth*, 113, 2008. doi: 10.1029/2007JB005248.

H. M. Bibby. **Crustal strain across the Marlborough faults, New Zealand**. *New Zealand Journal of Geology and Geophysics*, 19(4):407–425, 1976. doi: 10.1080/00288306.1976.10423537.

H. M. Bibby, T. G. Caldwell, F. J. Davey, and T. H. Webb. **Geophysical evidence on the structure of the Taupō Volcanic Zone and its hydrothermal circulation**. *Journal of Volcanology and Geothermal Research*, 68(1):29–58, 1995. doi: 10.1016/0377-0273(95)00007-H.

S. Bonnefoy-Claudet, F. Cotton, and PY. Bard. **The nature of noise wavefield and its applications for site effects studies: A literature review**. *Earth-Science Reviews*, 79(3):205–227, 2006. ISSN 0012-8252. doi: 10.1016/j.earscirev.2006.07.004.

F. Brenguier, M. Campillo, C. Hadziioannou, N. M. Shapiro, R. M. Nadeau, and E. Larose. **Postseismic relaxation along the San Andreas Fault at Parkfield from continuous seismological observations**. *Science*, 321(5895):1478–1481, 2008a. doi: 10.1126/science.1160943.

F. Brenguier, N. Shapiro, M. Campillo, V. Ferrazzini, Z. Duputel, O. Coutant, and A. Nercessian. **Towards forecasting volcanic eruptions using seismic noise**. *Nature Geoscience*, 1:126–130, 01 2008b. doi: 10.1038/ngeo104.

F. Brenguier, D. Rivet, A. Obermann, N. Nakata, P. Boué, T. Lecocq, M. Campillo, and N. Shapiro. **4-D noise-based seismology at volcanoes: Ongoing efforts and perspectives**. *Journal of Volcanology and Geothermal Research*, 321:182–195, 2016. ISSN 0377-0273. doi: 10.1016/j.jvolgeores.2016.04.036.

P. D. Bromirski and P. Gerstoft. **Dominant source regions of the Earth's "hum" are coastal**. *Geophysical Research Letters*, 36(13), 2009. doi: 10.1029/2009GL038903.

C. J. Bryan, S. Sherburn, H. M. Bibby, S. C. Bannister, and A. W. Hurst. **Shallow seismicity of the central Taupō Volcanic Zone, New Zealand: Its distribution and nature**. *New Zealand Journal of Geology and Geophysics*, 42(4):533–542, 1999. doi: 10.1080/00288306.1999.9514859.

H. Campbell, A. Malahoff, G. Browne, I. Graham, and R. Sutherland. **New Zealand geology**. *International Union of Geological Sciences*, 35:57–71, 2012. doi: 10.18814/epiiugs/2012/v35i1/006.

V. Cayol, J. H. Dieterich, A. T. Okamura, and A. Miklius. **High magma storage rates before the 1983 eruption of Kilauea, Hawaii**. *Science*, 288(5475):2343–2346, 2000. doi: 10.1126/science.288.5475.2343.

B. A. Chouet, R. A. Page, C. D. Stephens, J. C. Lahr, and J. A. Power. **Precursory swarms of long-period events at Redoubt Volcano (1989–1990), Alaska: Their origin and use as a forecasting tool**. *Journal of Volcanology and Geothermal Research*, 62(1):95–135, 1994. doi: 10.1016/0377-0273(94)90030-2.

J. F. Claerbout. **Synthesis of a layered medium from its acoustic transmission response**. *Geophysics*, 33(2):264–269, 1968. doi: 10.1190/1.1439927.

K. Clark, K. Berryman, N. Litchfield, U. Cochran, and T. Little. **Evaluating the coastal deformation mechanisms of the Raukumara Peninsula, northern Hikurangi subduction margin, New Zealand and insights into forearc uplift processes**. *New Zealand Journal of Geology and Geophysics*, 53(4):341–358, 2010. doi: 10.1080/00288306.2010.520324.

D. Clarke, L. Zaccarelli, N. M. Shapiro, and F. Brenguier. **Assessment of resolution and accuracy of the Moving Window Cross Spectral technique for monitoring crustal temporal variations using ambient seismic noise**. *Geophysical Journal International*, 186(2):867–882, 08 2011. doi: 10.1111/j.1365-246X.2011.05074.x.

D. Clarke, F. Brenguier, J.-L. Froger, N. M. Shapiro, A. Peltier, and T. Staudacher. **Timing of a large volcanic flank movement at Ppiton de la Fournaise Volcano using noise-based seismic monitoring and ground deformation measurements**. *Geophysical Journal International*, 195(2):1132–1140, 08 2013. ISSN 0956-540X. doi: 10.1093/gji/ggt276.

J. W. Cole. **Structure, petrology, and genesis of Cenozoic volcanism, Taupō Volcanic Zone, New Zealand-a review**. *New Zealand Journal of Geology and Geophysics*, 22(6):631–657, 1979. doi: 10.1080/00288306.1979.10424173.

A. Curtis, P. Gerstoft, H. Sato, R. Snieder, and K. Wapenaar. **Seismic interferometry-turning noise into signal**. *The Leading Edge*, 25(9):1082–1092, 2006. doi: 10.1190/1.2349814.

E. Daskalakis, C. P. Evangelidis, J. Garnier, N. S. Melis, G. Papanicolaou, and C. Tsogka. **Robust seismic velocity change estimation using ambient noise recordings**. *Geophysical Journal International*, 205(3):1926–1936, 04 2016. ISSN 0956-540X. doi: 10.1093/gji/ggw142.

R. S. M. De Plaen, T. Lecocq, C. Caudron, V. Ferrazzini, and O. Francis. **Single-station monitoring of volcanoes using seismic ambient noise**. *Geophysical Research Letters*, 43(16):8511–8518, 2016. doi: 10.1002/2016GL070078.

C. Donaldson, C. Caudron, R. G. Green, W. A. Thelen, and R. S. White. **Relative seismic velocity variations correlate with deformation at Kīlauea Volcano**. *Science Advances*, 3(6):e1700219, 2017. doi: 10.1126/sciadv.1700219.

G. A. Eiby. **Earthquake swarms and volcanism in New Zealand**. *Bulletin of volcanology*, 29:61–73, 1966.

G. A. Eiby. **A descriptive catalogue of New Zealand earthquakes**. *New Zealand Journal of Geology and Geophysics*, 16(4):857–907, 1973. doi: 10.1080/00288306.1973.10555229.

M. G. Ferrick, A. Qamar, and W. F. St. Lawrence. **Source mechanism of volcanic tremor**. *Journal of Geophysical Research: Solid Earth*, 87(B10):8675–8683, 1982. doi: 10.1029/JB087iB10p08675.

N. Fournier, C. A. Williams, L. Wallace, S. Sherburn, A. D. Jolly, L. Chardot, J. P. Ristau, S. Bourguignon, T. Hurst, B. J. Scott, M. Gibbs, K. Unglert, and R. J. Beavan. **From subduction processes to volcanic unrest: unraveling domino effects at Lake Taupō caldera, New Zealand**. *AGU Fall Meeting Abstracts*, 2013:V44C–01, 2013.

J. A. Gamble, C. P. Wood, R. C. Price, I. E. M. Smith, R B Stewart, and T. Waight. **A fifty year perspective of magmatic evolution on Ruapehu Volcano, New Zealand: verification of open system behaviour in an arc volcano**. *Earth and Planetary Science Letters*, 170(3):301–314, 1999. ISSN 0012-821X. doi: 10.1016/S0012-821X(99)00106-5.

A. Gerst and M. K. Savage. **Seismic anisotropy beneath Ruapehu Volcano: A possible eruption forecasting tool**. *Science*, 306(5701):1543–1547, 2004. doi: 10.1126/science.1103445.

W. F. Giggenbach and R. B. Glover. **The use of chemical indicators in the surveillance of volcanic activity affecting the Crater Lake on Mt. Ruapehu, New Zealand**. *Bulletin Volcanologique*, 39:70–81, 1975. doi: 10.1007/BF02596947.

A. Gorbatov, E. Saygin, and B. L. N. Kennett. **Crustal properties from seismic station autocorrelograms**. *Geophysical Journal International*, 192(2):861–870, 12 2012. doi: 10.1093/gji/ggs064.

P. Gouédard, L. Stehly, F. Brenguier, M. Campillo, Y. Colin de Verdière, E. Larose, L. Margerin, P. Roux, F. J. Sánchez-Sesma, N. M. Shapiro, and R. L. Weaver. **Cross-correlation of random fields: mathematical approach and applications**. *Geophysical Prospecting*, 56(3):375–393, 2008. ISSN 1365-2478. doi: 10.1111/j.1365-2478.2007.00684.x.

I. J. Graham and W. R. Hackett. **Petrology of Calc-alkaline lavas from Ruapehu Volcano and related vents, Taupō Volcanic Zone, New Zealand**. *Journal of Petrology*, 28(3):531–567, 06 1987. ISSN 0022-3530. doi: 10.1093/petrology/28.3.531.

R. H. Grapes and G. R. Holdgate. **Earthquake clustering and possible fault interactions across Cook Strait, New Zealand, during the 1848 and 1855 earthquakes**. *New Zealand Journal of Geology and Geophysics*, 57(3):312–330, 2014. doi: 10.1080/00288306.2014.907579.

G. W. Grindley. **Historical Taupō earthquakes and earth deformation**. *Roy. Soc. New Zealand Bull.*, 24:173–186, 1986.

B. Gutenberg. **Microseisms**. 5:53–92, 1958. ISSN 0065-2687. doi: 10.1016/S0065-2687(08)60075-8.

W. R. Hackett. **Geology and petrology of Ruapehu Volcano and related vents**. *Unpublished Ph.D. thesis, Open Access Te Herenga Waka-Victoria University of Wellington, New Zealand*, 1985. doi: 10.26686/wgtn.16949548.v1.

C. Hadziioannou, E. Larose, O. Coutant, P. Roux, and M. Campillo. **Stability of monitoring weak changes in multiply scattering media with ambient noise correlation: Laboratory experiments**. *The Journal of the Acoustical Society of America*, 125(6):3688–3695, 06 2009. ISSN 0001-4966. doi: 10.1121/1.3125345.

I. J. Hamling. **InSAR observations over the Taupō Volcanic Zone's cone volcanoes: insights and challenges from the New Zealand volcano supersite**. *New Zealand Journal of Geology and Geophysics*, 64(2-3):347–357, 2021. doi: 10.1080/00288306.2020.1721545.

I. J. Hamling, S. Hreinsdóttir, and N. Fournier. **The ups and downs of the TVZ: Geodetic observations of deformation around the Taupō Volcanic Zone, New Zealand**. *Journal of Geophysical Research: Solid Earth*, 120(6):4667–4679, 2015. doi: 10.1002/2015JB012125.

K. Hasselmann. **A statistical analysis of the generation of microseisms**. *Reviews of Geophysics*, 1(2):177–210, 1963. doi: 10.1029/RG001i002p00177.

R. Hechels. **Using ambient seismic noise to study temporal and spatial surface wave velocity structures and ambient noise field characteristics of central South Island, New Zealand**. *Unpublished Ph.D. thesis, Open Access Te Herenga Waka-Victoria University of Wellington*, 2017.

G. Hillers, Y. Ben-Zion, M. Campillo, and D. Zigone. **Seasonal variations of seismic velocities in the San Jacinto Fault area observed with ambient seismic noise**. *Geophysical Journal International*, 202(2):920–932, 06 2015. ISSN 0956-540X. doi: 10.1093/gji/ggv151.

T. Hirose, H. Nakahara, and T. Nishimura. **Combined use of repeated active shots and ambient noise to detect temporal changes in seismic velocity: application to Sakurajima Volcano, Japan**. *Earth, Planets and Space*, 69:42, 03 2017. doi: s40623-017-0613-7.

M. Hobiger, U. Wegler, K. Shiomi, and H. Nakahara. **Coseismic and post-seismic velocity changes detected by Passive Image Interferometry: comparison of one great and five strong earthquakes in Japan**. *Geophysical Journal International*, 205(2):1053–1073, 02 2016. ISSN 0956-540X. doi: 10.1093/gji/ggw066.

K. A. Hodgson, J. A. Lecointre, and V. E. Neall. **Onetapu Formation: The last 2000 yr of laharic activity at Ruapehu Volcano, New Zealand**. *New Zealand Journal of Geology and Geophysics*, 50(2):81–99, 2007. doi: 10.1080/00288300709509823.

A. J. Hotovec-Ellis, J. Gomberg, J. E. Vidale, and K. C. Creager. **A continuous record of intereruption velocity change at Mount St. Helens from coda wave interferometry**. *Journal of Geophysical Research: Solid Earth*, 119(3):2199–2214, 2014. doi: 10.1002/2013JB010742.

B. F. Houghton, J. H. Latter, and W. R. Hackett. **Volcanic hazard assessment for Ruapehu composite volcano, Taupō Volcanic Zone, New Zealand**. *Bulletin of Volcanology*, 49:737–751, 1987. doi: 10.1007/BF01079825.

A. W. Hurst. **Temperature observations of Crater Lake, Mt. Ruapehu, New Zealand, using Temperature Telemetry Bouys**. *Bulletin Volcanologique*, 43(3): 121–129, 1980. doi: 10.1007/BF02597616.

A. W. Hurst. **Stochastic simulation of volcanic tremor from Ruapehu**. *Journal of Volcanology and Geothermal Research*, 51(3):185–198, 1992. ISSN 0377-0273. doi: 10.1016/0377-0273(92)90122-T.

A. W. Hurst and P. J. McGinty. **Earthquake swarms to the west of Mt. Ruapehu preceding its 1995 eruption**. *Journal of Volcanology and Geothermal Research*, 90 (1):19–28, 1999. ISSN 0377-0273. doi: 10.1016/S0377-0273(99)00019-0.

A. W. Hurst and S. Sherburn. **Volcanic tremor at Ruapehu: Characteristics and implications for the resonant source**. *New Zealand Journal of Geology and Geophysics*, 36(4):475–485, 1993. doi: 10.1080/00288306.1993.9514593.

A. W. Hurst, H. M. Bibby, and R. R. Robinson. **Earthquake focal mechanisms in the central Taupō Volcanic Zone and their relation to faulting and deformation**. *New Zealand Journal of Geology and Geophysics*, 45(4):527–536, 2002. doi: 10.1080/00288306.2002.9514989.

T. Hurst, W. Heise, S. Hreinsdottir, and I. J. Hamling. **Geophysics of the Taupō Volcanic Zone: A review of recent developments**. *Geothermics*, 59:188–204, 2016. ISSN 0375-6505. doi: 10.1016/j.geothermics.2015.09.008.

T. Hurst, G. Kilgour, and I. J. Hamling. **Magmatic triggering of earthquakes on Distal Faults as a potential medium-term warning signal from Ruapehu Volcano**. *Geophysical Research Letters*, 45(23):12,776–12,783, 2018. doi: 10.1029/2018GL080677.

R. D. Hyndman, M. Yamano, and D. A. Oleskevich. **The seismogenic zone of subduction thrust faults**. *Island Arc*, 6(3):244–260, 1997. doi: 10.1111/j.1440-1738.1997.tb00175.x.

M. R. Ingham, H. M. Bibby, W. Heise, K. A. Jones, P. Cairns, S. Dravitzki, S. L. Bennie, T. G. Caldwell, and Y. Ogawa. **A magnetotelluric study of Mount Ruapehu Volcano, New Zealand**. *Geophysical Journal International*, 179(2):887–904, 11 2009. ISSN 0956-540X. doi: 10.1111/j.1365-246X.2009.04317.x.

D. M. Johnston, B. F. Houghton, V. E. Neall, K. R. Ronan, and D. Paton. **Impacts of the 1945 and 1995–1996 Ruapehu eruptions, New Zealand: An example of increasing societal vulnerability**. *GSA Bulletin*, 112(5):720–726, 05 2000. ISSN 0016-7606. doi: 10.1130/0016-7606(2000)112<720:IOTARE>2.0.CO;2.

G. Jolly, J. Beavan, B. Christenson, S. Ellis, A. Jolly, C. Miller, A. Peltier, B. Scott, S. Sherburn, L. Wallace, and R. McCaffrey. **What constitutes unrest at Taupō caldera, New Zealand?** *AGU Fall Meeting Abstracts*, 2008:V44A–07, 12 2008.

G. Kereszturi, L. Schaefer, S. Mead, C. Miller, J. Procter, and B. Kennedy. **Synthesis of hydrothermal alteration, rock mechanics and geophysical mapping to constrain failure and debris avalanche hazards at Mt. Ruapehu (New Zealand)**. *New Zealand Journal of Geology and Geophysics*, 64(2-3):421–442, 2021. doi: 10.1080/00288306.2021.1885048.

G. Kilgour, V. Manville, F. Della Pasqua, A. Graettinger, K.A. Hodgson, and G.E. Jolly. **The 25 September 2007 eruption of Mount Ruapehu, New Zealand: Directed ballistics, surtseyan jets, and ice-slurry lahars**. *Journal of Volcanology and Geothermal Research*, 191(1):1–14, 2010. ISSN 0377-0273. doi: 10.1016/j.jvolgeores.2009.10.015.

M. Kortink. **Effect of the Kaikōura earthquake on velocity changes in and around the ruptured region: A noise cross-correlation approach**. *Unpublished Ph.D. thesis, Open Access Te Herenga Waka-Victoria University of Wellington*, 2020. doi: 10.26686/wgtn.17145794.v1.

L. Krischer, T. Megies, R. Barsch, M. Beyreuther, T. Lecocq, C. Caudron, and J. Wassermann. **ObsPy: a bridge for seismology into the scientific Python ecosystem**. *Computational Science Discovery*, 8(1):014003, 05 2015. doi: 10.1088/1749-4699/8/1/014003.

E. Larose, P. Roux, and M. Campillo. **Reconstruction of Rayleigh–Lamb dispersion spectrum based on noise obtained from an air-jet forcing**. *The Journal of the Acoustical Society of America*, 122(6):3437–3444, 12 2007. doi: 10.1121/1.2799913.

T. Lecocq, C. Caudron, and F. Brenguier. **MSNoise, a Python package for monitoring seismic velocity changes using ambient seismic noise**. *Seismological Research Letters*, 85(3):715–726, 05 2014. doi: 10.1785/0220130073.

T. Lecocq, L. Longuevergne, H. A. Pedersen, F. Brenguier, and K. Stammler. **Monitoring ground water storage at mesoscale using seismic noise: 30 years of continuous observation and thermo-elastic and hydrological modeling**. *Scientific Reports*, 7:14241, 2017. doi: 10.1038/s41598-017-14468-9.

G. S. Leonard, D. M. Johnston, D. Paton, A. Christianson, J. Becker, and H. Keys. **Developing effective warning systems: Ongoing research at Ruapehu Volcano, New Zealand**. *Journal of Volcanology and Geothermal Research*, 172(3):199–215, 2008. ISSN 0377-0273. doi: 10.1016/j.jvolgeores.2007.12.008.

G. S. Leonard, R. P. Cole, B. W. Christenson, C. E. Conway, S. J. Cronin, J. A. Gamble, T. Hurst, B. M. Kennedy, C. A. Miller, J. N. Procter, L. R. Pure, D. B. Townsend, J. D. L. White, and C. J. N. Wilson. **Ruapehu and Tongariro stratovolcanoes: a review of current understanding**. *New Zealand Journal of Geology and Geophysics*, 64(3):389–420, 07 2021. doi: 10.1080/00288306.2021.1909080.

D. A. Lockner, J. B. Walsh, and J. D. Byerlee. **Changes in seismic velocity and attenuation during deformation of granite**. *Journal of Geophysical Research (1896-1977)*, 82(33):5374–5378, 1977. doi: 10.1029/JB082i033p05374.

Z. Lu, D. Mann, J. T. Freymueller, and D. J. Meyer. **Synthetic aperture radar interferometry of Okmok Volcano, Alaska: Radar observations**. *Journal of Geophysical Research: Solid Earth*, 105(B5):10791–10806, 2000. doi: 10.1029/2000JB900034.

M. Madley, A. Yates, M. Savage, W. Wang, T. Okada, S. Matsumoto, Y. Iio, and K. Jacobs. **Velocity changes around the Kaikōura earthquake ruptures from ambient noise cross-correlations**. *Geophysical Journal International*, 229(2):1357–1371, 12 2021. ISSN 0956-540X. doi: 10.1093/gji/ggab514.

K. Mannen, Y. Abe, Y. Daita, R. Doke, M. Harada, G. Kikugawa, N. Honma, Y. Miyashita, and Y. Yukutake. **Volcanic unrest at Hakone volcano after the 2015 phreatic eruption: reactivation of a ruptured hydrothermal system?** *Earth, Planets and Space*, page 80, 2021. ISSN 1880-5981. doi: 10.1186/s40623-021-01387-3.

V. Manville and S. J. Cronin. **Breakout Lahar from New Zealand's Crater Lake**. *Eos, Transactions American Geophysical Union*, 88(43):441–442, 2007. doi: 10.1029/2007EO430001.

U. Meier, N. M. Shapiro, and F. Brenguier. **Detecting seasonal variations in seismic velocities within Los Angeles basin from correlations of ambient seismic noise**. *Geophysical Journal International*, 181(2):985–996, 05 2010. ISSN 0956-540X. doi: 10.1111/j.1365-246X.2010.04550.x.

E. Mestel. **Seismicity, sub-surface structure and partnership with Tangata Whenua of Taupō Volcano**. *Open Access Te Herenga Waka-Victoria University of Wellington. Thesis*, 2023. doi: 10.26686/wgtn.24405691.

S. Minato, T. Tsuji, S. Ohmi, and T. Matsuoka. **Monitoring seismic velocity change caused by the 2011 Tohoku-oki earthquake using ambient noise records**. *Geophysical Research Letters*, 39(9), 2012. doi: 10.1029/2012GL051405.

A. Mordret, A.D. Jolly, Z. Duputel, and N. Fournier. **Monitoring of phreatic eruptions using Interferometry on Retrieved cross-correlation Function from Ambient Seismic Noise: Results from Mt. Ruapehu, New Zealand**. *Journal of Volcanology and Geothermal Research*, 191(1):46–59, 2010. ISSN 0377-0273. doi: 10.1016/j.jvolgeores.2010.01.010.

N. Mortimer. **New Zealand's geological foundations**. *Gondwana Research*, 7(1): 261–272, 2004. doi: 10.1016/S1342-937X(05)70324-5.

N. Mortimer, F. J. Davey, A. Melhuish, J. Yu, and N. J. Godfrey. **Geological interpretation of a deep seismic reflection profile across the Eastern Province and Median Batholith, New Zealand: Crustal architecture of an extended Phanerozoic convergent orogen**. *New Zealand Journal of Geology and Geophysics*, 45(3):349–363, 2002. doi: 10.1080/00288306.2002.9514978.

V. Mouslopoulou, A. Nicol, T. Little, and J. J. Walsh. **Terminations of large strike-slip faults: An alternative model from New Zealand**. *Geological Society, London, Special Publications*, 290, 01 2007. doi: 10.1144/SP290.15.

J. Nakajima, T. Matsuzawa, A. Hasegawa, and D. Zhao. **Three-dimensional structure of V_p, V_s, and V_p/V_s beneath northeastern Japan: Implications for arc magmatism and fluids**. *Journal of Geophysical Research: Solid Earth*, 106(B10): 21843–21857, 2001. doi: 10.1029/2000JB000008.

A. H. Nooghabi. **Green's function retrieval from noise correlation in multiple scattering media**. *Ph.D. thesis, Open Access Sorbonne Université,*, 2018.

R. J. Norris and A. F. Cooper. **Erosional control on the structural evolution of a transpressional thrust complex on the Alpine Fault, New Zealand**. *Journal of Structural Geology*, 19(10):1323–1342, 1997. doi: 10.1016/S0191-8141(97)00036-9.

R.J. Norris, P.O. Koons, and A.F. Cooper. **The obliquely-convergent plate boundary in the South Island of New Zealand: implications for ancient collision zones**. *Journal of Structural Geology*, 12(5):715–725, 1990. doi: 10.1016/0191-8141(90) 90084-C.

A. Nur. **Effects of stress on velocity anisotropy in rocks with cracks**. *Journal of Geophysical Research (1896-1977)*, 76(8):2022–2034, 1971. doi: 10.1029/JB076i008p02022.

A. Nur and G. Simmons. **Stress-induced velocity anisotropy in rock: An experimental study**. *Journal of Geophysical Research (1896-1977)*, 74(27):6667–6674, 1969. doi: 10.1029/JB074i027p06667.

A. Obermann, T. Planès, E. Larose, and M. Campillo. **Imaging preeruptive and coeruptive structural and mechanical changes of a volcano with ambient seismic noise**. *Journal of Geophysical Research: Solid Earth*, 118(12):6285–6294, 2013a. doi: 10.1002/2013JB010399.

A. Obermann, T. Planès, E. Larose, and M. Campillo. **Imaging preeruptive and coeruptive structural and mechanical changes of a volcano with ambient seismic noise**. *Journal of Geophysical Research: Solid Earth*, 118(12):6285–6294, 2013b. doi: 10.1002/2013JB010399.

L. Passarelli and E. E. Brodsky. **The correlation between run-up and repose times of volcanic eruptions**. *Geophysical Journal International*, 188(3):1025–1045, 03 2012. ISSN 0956-540X. doi: 10.1111/j.1365-246X.2011.05298.x.

H. Paulssen, J. Visser, and G. Nolet. **The crustal structure from teleseismic P-wave coda-I. Method**. *Geophysical Journal International*, 112(1):15–25, 01 1993. doi: 10.1111/j.1365-246X.1993.tb01433.x.

A. Peltier, T. Hurst, B. Scott, and V. Cayol. **Structures involved in the vertical deformation at Lake Taupō (New Zealand) between 1979 and 2007: New insights from numerical modelling**. *Journal of Volcanology and Geothermal Research*, 181(3):173–184, 2009. ISSN 0377-0273. doi: 10.1016/j.jvolgeores.2009.01.017.

T.-S. Pham and H. Tkalčić. **On the feasibility and use of teleseismic P wave coda autocorrelation for mapping shallow seismic discontinuities**. *Journal of Geophysical Research: Solid Earth*, 122(5):3776–3791, 2017. doi: 10.1002/2017JB013975.

S. H. Potter, G. E. Jolly, V. E. Neall, D. M. Johnston, and B. J. Scott. **Communicating the status of volcanic activity: revising New Zealand's volcanic alert level system**. *Journal of Applied Volcanology*, 3:13, 2014. doi: 10.1186/s13617-014-0013-7.

S. H. Potter, B. J. Scott, G. E. Jolly, D. M. Johnston, and V. E. Neall. **Introducing the Volcanic Unrest Index (VUI): a tool to quantify and communicate the intensity of volcanic unrest**. *Bulletin of Volcanology*, 77:77, 2015a. doi: 10.1007/s00445-015-0957-4.

S. H. Potter, B. J. Scott, G. E. Jolly, D. M. Johnston, and V. E. Neall. **A catalogue of caldera unrest at Taupō Volcanic Centre, New Zealand, using the Volcanic Unrest Index (VUI)**. *Bulletin of Volcanology*, 77:78, 2015b. doi: 10.1007/s00445-015-0956-5.

G. Poupinet, W. L. Ellsworth, and J. Frechet. **Monitoring velocity variations in the crust using earthquake doublets: An application to the Calaveras Fault, California**. *Journal of Geophysical Research: Solid Earth*, 89, 1984. doi: 10.1029/JB089iB07p05719.

A. C. Ramírez and A. B. Weglein. **Green's theorem as a comprehensive framework for data reconstruction, regularization, wavefield separation, seismic interferometry, and wavelet estimation: A tutorial**. *Geophysics*, 74(6):W35–W62, 2009. doi: 10.1190/1.3237118.

A. Ratdomopurbo and G. Poupinet. **Monitoring a temporal change of seismic velocity in a volcano: Application to the 1992 eruption of Mt. Merapi (Indonesia)**. *Geophysical Research Letters*, 22(7):775–778, 1995. doi: 10.1029/95GL00302.

A. Ratdomopurbo and G. Poupinet. **An overview of the seismicity of Merapi volcano (Java, Indonesia), 1983–1994**. *Journal of Volcanology and Geothermal Research*, 100(1):193–214, 2000. ISSN 0377-0273. doi: 10.1016/S0377-0273(00)00137-2.

M. Reyners. **Plate coupling and the hazard of large subduction thrust earthquakes at the Hikurangi subduction zone, New Zealand**. *New Zealand Journal of Geology and Geophysics*, 41(4):343–354, 1998. doi: 10.1080/00288306.1998.9514815.

M. Reyners, D. Eberhart-Phillips, G. Stuart, and Y. Nishimura. **Imaging subduction from the trench to 300 km depth beneath the central North Island, New Zealand, with V_p and V_p/V_s**. *Geophysical Journal International*, 165(2):565–583, 05 2006. ISSN 0956-540X. doi: 10.1111/j.1365-246X.2006.02897.x.

M. Reyners, D. Eberhart-Phillips, and G. Stuart. **The role of fluids in lower-crustal earthquakes near continental rifts**. *Nature*, 446:1075–1078, 2007. doi: 10.1038/nature05743.

D. Rivet, F. Brenguier, D. Clarke, N. M. Shapiro, and A. Peltier. **Long-term dynamics of Ppiton de la Fournaise Volcano from 13 years of seismic velocity change measurements and GPS observations**. *Journal of Geophysical Research: Solid Earth*, 119(10):7654–7666, 2014. doi: 10.1002/2014JB011307.

J. V. Rowland and R. H. Sibson. **Structural controls on hydrothermal flow in a segmented rift system, Taupō Volcanic Zone, New Zealand**. *Geofluids*, 4(4): 259–283, 2004. doi: 10.1111/j.1468-8123.2004.00091.x.

D. P. Rowlands, R. S. White, and A. J. Haines. **Seismic tomography of the Tongariro Volcanic Centre, Zealand**. *Geophysical Journal International*, 163(3):1180–1194, 12 2005. doi: 10.1111/j.1365-246X.2005.02716.x.

K. G. Sabra, P. Gerstoft, P. Roux, W. A. Kuperman, and M. C. Fehler. **Extracting time-domain Green's function estimates from ambient seismic noise**. *Geophysical Research Letters*, 32(3), 2005. doi: 10.1029/2004GL021862.

M. K. Savage, V. Ferrazzini, A. Peltier, E. Rivemale, J. Mayor, A. Schmid, F. Brenguier, F. Massin, J.-L. Got, J. Battaglia, A. DiMuro, T. Staudacher, D. Rivet, B. Taisne, and A. Shelley. **Seismic anisotropy and its precursory change before eruptions at Piton de la Fournaise Volcano, La Réunion**. *Journal of Geophysical Research: Solid Earth*, 120(5):3430–3458, 2015. doi: 10.1002/2014JB011665.

M. Schimmel and H. Paulssen. **Noise reduction and detection of weak, coherent signals through phase-weighted stacks**. *Geophysical Journal International*, 130 (2):497–505, 08 1997. doi: 10.1111/j.1365-246X.1997.tb05664.x.

J. Schuler. **Temporal velocity variations accompanying geodetically detected deformation at Taupō Supervolcano**. *Open Access Te Herenga Waka-Victoria University of Wellington. Thesis*, 2023. doi: 10.26686/wgtn.23606316.

C. Sens-Schönfelder and U. Wegler. **Passive image interferometry and seasonal variations of seismic velocities at Merapi Volcano, Indonesia**. *Geophysical Research Letters*, 33(21), 2006. doi: 10.1029/2006GL027797.

C. Sens-Schönfelder and U. Wegler. **Passive image interferometry for monitoring crustal changes with ambient seismic noise**. *Comptes Rendus Geoscience*, 343 (8):639–651, 2011. ISSN 1631-0713. doi: 10.1016/j.crte.2011.02.005.

N. M. Shapiro, M. Campillo, L. Stehly, and M. H. Ritzwoller. **High-Resolution Surface-Wave tomography from ambient seismic noise**. *Science*, 307(5715): 1615–1618, 2005. doi: 10.1126/science.1108339.

S. Sherburn, C. J. Bryan, A. W. Hurst, J. H. Latter, and B. J. Scott. **Seismicity of Ruapehu Volcano, New Zealand, 1971–1996: a review**. *Journal of Volcanology and Geothermal Research*, 88(4):255–278, 1999. ISSN 0377-0273. doi: 10.1016/S0377-0273(99)00014-1.

P. G. Silver, T. M. Daley, F. Niu, and E. L. Majer. **Active source monitoring of Cross-Well seismic travel time for Stress-Induced changes**. *Bulletin of the Seismological Society of America*, 97(1B):281–293, 02 2007. ISSN 0037-1106. doi: 10.1785/0120060120.

R. Snieder. **Extracting the Green's function from the correlation of coda waves: A derivation based on stationary phase**. *Physical Review E*, 69(8):046610, Apr 2004. doi: 10.1103/PhysRevE.69.046610.

R. Snieder, A. Grêt, H. Douma, and J. Scales. **Coda Wave Interferometry for estimating nonlinear behavior in seismic velocity**. *Science*, 295(5563):2253–2255, 2002. doi: 10.1126/science.1070015.

R. S. J. Sparks. **Forecasting volcanic eruptions**. *Earth and Planetary Science Letters*, 210(1):1–15, 2003. ISSN 0012-821X. doi: 10.1016/S0012-821X(03)00124-9.

R.S.J. Sparks. **Causes and consequences of pressurisation in lava dome eruptions**. *Earth and Planetary Science Letters*, 150(3):177–189, 1997. ISSN 0012-821X. doi: 10.1016/S0012-821X(97)00109-X.

G. S. Steinberg and A. S. Steinberg. **On possible causes of volcanic tremor**. *Journal of Geophysical Research (1896-1977)*, 80(11):1600–1604, 1975. doi: 10.1029/JB080i011p01600.

T. Stern, E. G. C. Smith, F. J. Davey, and K. J. Muirhead. **Crustal and upper mantle structure of the northwestern North Island, New Zealand, from seismic refraction data**. *Geophysical Journal International*, 91(3):913–936, 12 1987. doi: 10.1111/j.1365-246X.1987.tb01674.x.

T. Stern, W. Stratford, A. Seward, M. Henderson, M. Savage, E. Smith, A. Benson, S. Greve, and M. Salmon. **Crust-mantle structure of the central North Island, New Zealand, based on seismological observations**. *Journal of Volcanology and Geothermal Research*, 190(1):58–74, 2010. doi: 10.1016/j.jvolgeores.2009.11.017.

W. Sun and B. L. N. Kennett. **Receiver structure from teleseisms: Autocorrelation and cross correlation**. *Geophysical Research Letters*, 43(12):6234–6242, 2016. doi: 10.1002/2016GL069564.

T. Tanimoto, J. Um, K. Nishida, and N. Kobayashi. **Earth's continuous oscillations observed on seismically quiet days**. *Geophysical Research Letters*, 25(10):1553–1556, 1998. doi: 10.1029/98GL01223.

M. Nafi Toksöz and Richard T. Lacoss. **Microseisms: Mode structure and sources**. *Science*, 159(3817):872–873, 1968. doi: 10.1126/science.159.3817.872.

V. C. Tsai. **A model for seasonal changes in GPS positions and seismic wave speeds due to thermoelastic and hydrologic variations**. *Journal of Geophysical Research: Solid Earth*, 116(B4), 2011. doi: 10.1029/2010JB008156.

L. P. Vinnik. **Sources of microseismic P waves**. *pure and applied Geophysics*, 103: 282–289, 1973. doi: 10.1007/BF00876404.

R. I. Walcott. **Modes of oblique compression: Late Cenozoic tectonics of the South Island of New Zealand**. *Reviews of Geophysics*, 36(1):1–26, 1998. doi: 10.1029/97RG03084.

L. M. Wallace, J. Beavan, R. McCaffrey, K. Berryman, and P. Denys. **Balancing the plate motion budget in the South Island, New Zealand using GPS, geological and seismological data**. *Geophysical Journal International*, 168(1):332–352, 01 2007. doi: 10.1111/j.1365-246X.2006.03183.x.

L. M. Wallace, P. Barnes, J. Beavan, R. Van Dissen, N. Litchfield, J. Mountjoy, R. Langridge, G. Lamarche, and N. Pondard. **The kinematics of a transition from subduction to strike-slip: An example from the central New Zealand plate**

boundary. *Journal of Geophysical Research: Solid Earth*, 117(B2), 2012. doi: 10.1029/2011JB008640.

Q.-Y. Wang and H. Yao. **Monitoring of velocity changes based on seismic ambient noise: A brief review and perspective**. *Earth and Planetary Physics*, 4(5):532–542, 2020. doi: 10.26464/epp2020048.

Q.-Y. Wang, M. Campillo, F. Brenguier, A. Lecointre, T. Takeda, and A. Hashima. **Evidence of changes of seismic properties in the entire crust beneath Japan after the Mw 9.0, 2011 Tohoku-oki earthquake**. *Journal of Geophysical Research: Solid Earth*, 124(8):8924–8941, 2019. doi: 10.1029/2019JB017803.

K. Wapenaar, D. Draganov, R. Snieder, X. Campman, and A. Verdel. **Chapter 15 Seismic Interferometry: Tutorial on seismic interferometry: Part 1 - Basic principles and applications**. *Society of Exploration Geophysicists*, 01 2010. doi: 10.1190/1.9781560802273.ch15.

C. J. N. Wilson. **Volcanoes: Characteristics, tipping points, and those pesky unknown unknowns**. *Elements*, 13(1):41–46, 02 2017. ISSN 1811-5209. doi: 10.2113/gselements.13.1.41.

C. J. N. Wilson and J. V. Rowland. **The volcanic, magmatic and tectonic setting of the Taupō Volcanic Zone, New Zealand, reviewed from a geothermal perspective**. *Geothermics*, 59:168–187, 2016. doi: 10.1016/j.geothermics.2015.06.013.

C. J. N. Wilson, B. F. Houghton, M. O. McWilliams, M. A. Lanphere, S. D. Weaver, and R. M. Briggs. **Volcanic and structural evolution of Taupō Volcanic Zone, New Zealand: a review**. *Journal of Volcanology and Geothermal Research*, 68(1): 1–28, 1995. doi: 10.1016/0377-0273(95)00006-G.

J. Xie, Y. Yang, and S. Ni. **On the accuracy of long-period Rayleigh waves extracted from ambient noise**. *Geophysical Journal International*, 206(1):48–55, 04 2016. ISSN 0956-540X. doi: 10.1093/gji/ggw137.

Y. Yang and M. H. Ritzwoller. **Characteristics of ambient seismic noise as a source for surface wave tomography**. *Geochemistry, Geophysics, Geosystems*, 9(2), 2008. doi: 10.1029/2007GC001814.

Y. Yang, M. H. Ritzwoller, A. L. Levshin, and N. M. Shapiro. **Ambient noise Rayleigh wave tomography across Europe**. *Geophysical Journal International*, 168(1):259–274, 01 2007. ISSN 0956-540X. doi: 10.1111/j.1365-246X.2006.03203.x.

A. S. Yates. **Seismic velocity changes at White Island Volcano, New Zealand, using ten years of ambient noise interferometry**. *Master's thesis, Te Herenga Waka-Victoria University of Wellington.*, 2018.

A. S. Yates, M. K. Savage, A. D. Jolly, C. Caudron, and I. J. Hamling. Volcanic, coseismic, and seasonal changes detected at white island (whakaari) volcano, new zealand, using seismic ambient noise. *Geophysical Research Letters*, 46(1):99–108, 2019. doi: 10.1029/2018GL080580.

G. F. Zellmer, Y. Iizuka, C. Lormand, and A. Moebis. **Beyond crystal mushes: evidence for uptake of high-T pyroxene antecrysts from mid- to upper crustal andesites into tephras from the Central Plateau, New Zealand**. *New Zealand Journal of Geology and Geophysics*, 64(2-3):443–455, 2021. doi: 10.1080/00288306.2020.1848883.

APPENDIX A

VELOCITY VARIATIONS SUPPLEMENTARY MATERIAL

The appendices are split into two parts. This Appendix chapter contains the parameter choices that MSNoise uses to process data from raw ambient noise to velocity information [see AppendixA.1]. Appendix A.2 contains the station final filter used in this study.

A.1 FINAL MSNOISE PARAMETERS

This section includes the parameter choices that MSNoise uses to process data from raw ambient noise to velocity information.

Parameter	**Value**	**Definition**
startdate	2022-01-01	Start Date to process.
enddate	2022-12-31	End Date to process.
channels	EHZ, HHZ	Sensors' channels.
analysis_duration	86400	Duration of the Analysis in seconds.
cc_sampling_rate	25	Sampling Rate for the Cross-Correlation (in Hz).
cc_normalisation	ABSMAX	Normalisation method for individual CCFs, default is not normalized (NO), but can be normalized based on the power of the two traces (POW), or by the maximum (MAX) or absolute maximum (ABSMAX) of the CCF.

Continued on the next page

Parameter	Value	Definition
resampling_method	Lanczos	Resampling method [Lanczos]/Decimate.
preprocess_lowpass	12	Preprocessing Low-pass value (in Hz).
preprocess_highpass	0.01	Preprocessing High-pass value (in Hz).
preprocess_max_gap	10	Preprocessing maximum gap length that will be filled by interpolation (in seconds).
preprocess_taper_length	20	Duration of the taper applied at the beginning and end of trace during the preprocessing, to allow highpass filtering (in seconds).
remove_response	Y	Remove instrument response Y/[N].
response_prefilt	(0.005, 0.006, 30.0, 35.0)	Remove instrument correction pre-filter (in Hz).
maxlag	120	Maximum lag (in seconds).
corr_duration	1800	Data windows to correlate (in seconds).
overlap	0	Amount of overlap between data windows [0:1].

Continued on the next page

Parameter	**Value**	**Definition**
windsorizing	-1	The upper frequency bound of the whiten function Windsorizing at N time RMS, 0 disables windsorizing, -1 enables 1-bit normalization.
whitening	A	Whiten Traces before cross-correlation: [A]ll (except for autocorr), [N]one, or only if [C]omponents are different.
whitening_type	B	Type of spectral whitening function to use: [B]rutal (amplitude to 1.0), divide spectrum by its [PSD] or by bandpassing the white spectrum with a hanning-window.
clip_after_whiten	Y	Do the clipping (winsorizing) after whitening? Y/[N].
stack_method	linear	Stack Method: Linear Mean or Phase Weighted Stack [linear]/pws.
components_to_compute	ZZ	filter number applied in this study.
keep_days	Y	Keep all daily cross-corr [Y]/N.
ref_begin	2022-01-01	Beginning or REF stacks.
ref_end	2022-12-31	End or REF stacks.

Continued on the next page

Parameter	**Value**	**Definition**
mov_stack	45	Number of days to stack for the Moving-window stacks.
dtt_lag	dynamic	How is the lag window defined dynamic/[static].
dtt_v	2	If dtt_lag=dynamic: what velocity to use to avoid ballistic wave (in km/s).
dtt_width	40	Width of the time lag window (in seconds).
dtt_sides	both	Which sides to use [both]/left/right.
dtt_mincoh	0.9	Minimum coherence on dt measurement, MWCS points with values lower than that will not be used in the WLS, [0:1].
dtt_maxerr	0.1	Maximum error on dt measurement, MWCS points with values larger than that will not be used in the WLS [0:1].
dtt_maxdt	0.5	Maximum dt values, MWCS points with values larger than that will not be used in the WLS (in seconds).

Table A.1: Table of Parameters

A.2 STATION PAIR FINAL FILTER

Parameter	**Value**	**Definition**
Ref	6	Filter number applied in this study
Low	0.03	The lower frequency bound of the whiten function
High	0.35	The upper frequency bound of the whiten function
Mwcs Low	0.04	The lower frequency bound of the linear regression done in MWCS
Mwcs High	0.34	The upper frequency bound of the linear regression done in MWCS
Mwcs Wlen	20	Window length to perform MWCS
Mwcs Step	4	Step of the windowing procedure in MWCS

Table A.2: Station pair dataset final filter table